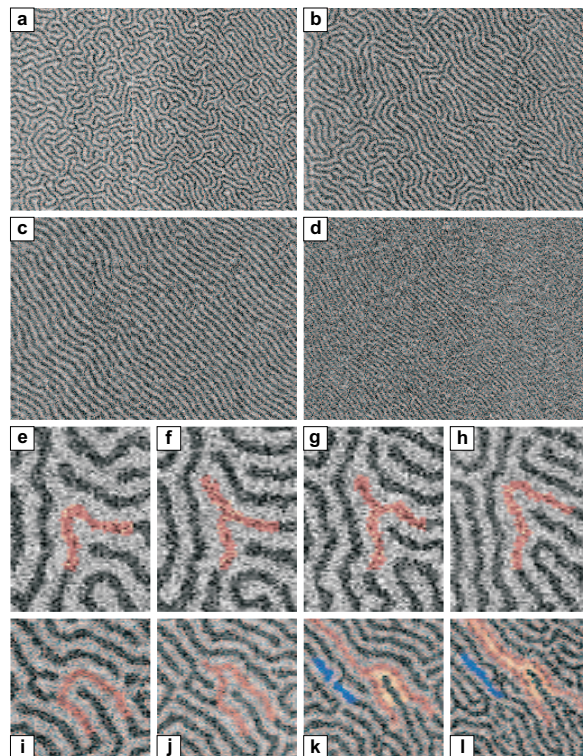


JAHRESBERICHT 2003



Laboratorium für Festkörperphysik
der
Eidgenössischen Technischen Hochschule
Zürich

Cover page:

An inverse transition of the magnetic domain pattern in ultrathin Fe films on Cu(001). Images A-D show the transformation of a labyrinthine pattern to a less symmetric array of stripes as the temperature is increased. The microscopic mechanisms mediating the transition – knee-bend and bridge instabilities – are highlighted in images E-H and I-L. (Nature 422, 701 (2003))

This annual report was edited by: C. Ellenberger.

PREFACE

This report highlights the scientific achievements of the solid state physics laboratory at ETH Zrich for the year 2003. It is with great pleasure that we are able to look back at another productive year of scientific collaboration and endeavor. The unflagging support of the technical staff of the individual research groups as well as the technical personnel of the physics department was absolutely instrumental in meeting our scientific objectives. The scientific staff of our institute was intimately involved on all levels of teaching, from undergraduate to graduate classes and including lab courses as well. We thank the board of ETH Zrich for their continual support in times of shrinking budgets. External support from the Schweizerischer Nationalfonds and other sources is gratefully acknowledged.

This is the second time, that our yearly report appears in its new face. We appreciate the help of Leo Degiorgi, Christoph Ellenberger and Hanni Hediger in the preparation of this document.

Zürich, March 2003

Der Vorsteher

A handwritten signature in black ink, reading "Klaus Ensslin". The signature is written in a cursive style with a large, prominent initial 'K'.

Prof. Dr. K. Ensslin

Contents

1	Physics of new materials	9
1.1	Organic molecular crystals	11
1.1.1	Electrical transport in Rubrene single crystals	11
1.1.2	Transport properties of organic single crystals measured by a field-effect technique	11
1.1.3	Bulk doping of pentacene single crystals	12
1.1.4	Temperature dependent structure parameters of pentacene single crystals	12
1.2	Organic thin film transistors	13
1.2.1	Threshold Voltage Shift by Surface Modification of the Gate Insulator in Pentacene TFTs	13
1.2.2	Modeling and parameter extraction on Pentacene Thin Film Transistors (Pc-TFTs)	14
1.3	Correlated electrons on a triangular lattice: Na_xCoO_2	14
1.3.1	Synthesis and structural investigations of Na_xCoO_2	14
1.3.2	Low-energy electronic states in triangular Na_xCoO_2	15
1.4	SiGe modulation doped heterostructures	15
1.5	Materials synthesis and high pressure crystal growth	16
1.5.1	Growth of MgB_2 single crystals	16
1.5.2	Substitution of carbon and aluminum in superconducting MgB_2	17
1.5.3	Copper-oxides	18
1.5.4	Growth of $\text{Al}_x\text{Ga}_{1-x}\text{N}$ single crystals	19
1.5.5	GaN films grown by MBE on GaN bulk single crystal substrates	20
1.5.6	Investigations performed in collaboration with other researchers	20
2	Physics of mesoscopic structures, semiconductor nanostructures	23
2.1	Electric field tuned singlet-triplet transition in quantum rings	25
2.2	Phase-coherent ring as a detector for single-electron effects	26
2.3	Multi-terminal transport through quantum dots	27
2.4	Electronic transport through a quantum dot network	28
2.5	Magnetic field dependent transmission phase of a double dot system in a quantum ring	29
2.6	Electronic properties of p-type GaAs heterostructures	29
2.7	Microwave spectroscopy of semiconductor nanostructures	30
2.8	Time resolved detection of electrons in a quantum dot	31

2.9	Local spectroscopy in the quantum Hall regime	31
2.10	Quantitative topographical analysis of Nuclear Pore Complex function using Scanning Force Microscopy	32
3	Condensed matter at low temperatures	35
3.1	Physical properties of hexaborides	37
3.1.1	Magnetotransport in $\text{Eu}_x\text{Ca}_{1-x}\text{B}_6$ ($0 < x < 1$)	37
3.1.2	Bulk and surface excitations in lanthanum hexaboride	37
3.1.3	Magneto-optical study of <i>Ca</i> -doped EuB_6	38
3.2	Superconductivity	40
3.2.1	Ambivalence of the anisotropy of the vortex lattice in an anisotropic type-II superconductor.	40
3.2.2	Unusual magnetic field-induced phase transition in superconducting NbSe_2	40
3.2.3	New interpretation of the equilibrium magnetization of a $\text{Tl}_2\text{Ba}_2\text{CaCu}_2\text{O}_{8+x}$ single crystal.	41
3.3	Structural and physical properties of quasicrystals	42
3.3.1	Structure analysis of decagonal Al-Co-Ni quasicrystals	42
3.3.2	Comparative NMR studies of decagonal and icosahedral $\text{Al}_{69.8}\text{Pd}_{12.1}\text{Mn}_{18.1}$	43
3.4	Physics of low-dimensional systems	43
3.4.1	Unconventional Charge Ordering in $\text{Na}_{0.70}\text{CoO}_2$ below 300 K	43
3.4.2	Low-temperature specific heat of $\text{Na}_2\text{V}_3\text{O}_7$	44
3.4.3	NMR and dc-susceptibility studies of NaVGe_2O_6	45
3.5	Instrumentation: NMR under pressure	45
3.6	Electron holography	46
3.6.1	Measurement of the mean inner potential of various metals by electron holography	46
3.7	Noble gases as model systems to study solidification behaviour of melts	46
3.8	Application oriented thin film research	47
3.8.1	Epitaxial IV-VI narrow gap semiconductor layers	47
3.8.2	Thin film solar cells based on $\text{Cu}(\text{In,Ga})\text{Se}_2$ and CdTe compound semiconductors	48
3.8.2.1	CIGS thin film solar cells	48
3.8.2.2	CdTe thin film solar cells	49
4	Magnetism, Electron Spectroscopy	51
4.1	Surface Physics	53
4.1.1	Self-assembled Al nanocrystals on the decagonal surface of the $\text{Al}_{70}\text{Co}_{15}\text{Ni}_{15}$	53
4.1.2	Structural compaction of the icosahedral quasicrystal $\text{Al}_{70}\text{Pd}_{20}\text{Mn}_{10}$	53
4.1.3	Atomic structure of the Al_2O_3 (10-0) surface	54
4.2	Magnetism	54
4.2.1	Labyrinthine to striped pattern inverse transition in perpendicularly magnetized ultrathin films	54
4.2.2	Pulsed precessional motion on the 'back of an envelope'	55

5 Publications	57
6 Talks	67

Chapter 1

Physics of new materials

(<http://www.solidphys.ethz.ch/pnm>)

Head

Prof. Dr. Bertram Batlogg

Academic Staff

Dr. Christoph Bergemann

Dr. David J. Gundlach

Benjamin Rössner

Markus Brühwiler

Simon Haas

Claudia Goldmann

Kurt Pernstich

Technical Staff

Kurt Mattenberger

Hans Peter Staub

Academic Guest

Dr. Jun-ichi Takeya, CRIEPI, Tokyo (Japan)

Administrative Staff

Gabriela Strahm

High pressure materials synthesis group

Head

Dr. Janusz Karpinski

Academic Staff

Peter Geiser

Dr. Sergei Kazakov

Jan Jun

Dr. Nikolai Zhigadlo

Academic Guests

Dr. Andrej Mironov, Moscow State University, Moscow (Russia)

Dr. Roman Puzniak, Polish Academy of Sciences, Warsaw (Poland)

Dr. Andrzej Wisniewski, Polish Academy of Sciences, Warsaw (Poland)

1.1 Organic molecular crystals

1.1.1 Electrical transport in Rubrene single crystals

C. Krellner, S. Haas, D. Gundlach, K. Mattenberger, H. P. Staub, B. Batlogg

Rubrene crystals are grown by vapor-phase transport. The purification of the starting material by means of multiple sublimations in vacuo plays an important role in producing high quality crystals, as does the use of Ar 6.0, ultra clean glassware, and the protection from UV light.

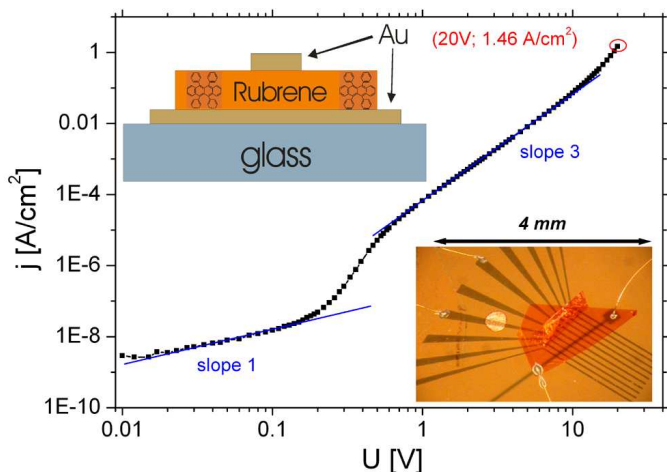


Figure 1.1: Space-charge-limited current-voltage characteristics of a rubrene single crystal (thickness $2 \mu\text{m}$.) The upper left inset shows a schematic cross-section of the sample and gold contacts. The lower right inset is a top view on a typical sample with ten contacts on the bottom and the top Au contact.

The crystals are electrically characterized either by FET measurements or space-charge limited current (SCLC) measurements. The latter technique gives a measure for the bulk mobility in c -direction, perpendicular to the flat surface of the sample. A thin crystal (typically a few microns thick) is put on top of a glass substrate with Au/Cr stripes as contacts. A gold top electrode is thermally evaporated directly on the crystal as the final step of sample preparation. Measurements are done in darkness and at 5×10^{-5} mbar. As the trap free limit could not be reached, lower limits for the bulk mobility up to $8 \times 10^{-2} \text{cm}^2/\text{Vs}$ and trap densities N_t in the order of 10^{14}cm^{-3} could be estimated. These values are comparable to that of pentacene and tetracene crystals grown by the same method.

The hole mobility measured in this experiment relates to transport perpendicular to the molecule layers, and is about 100 times smaller than measured parallel to the

layers in the single-crystal FET method (see 1.1.2), indicative of a large mobility anisotropy similar to the one observed in other layered organic molecular crystals.

1.1.2 Transport properties of organic single crystals measured by a field-effect technique

C. Goldmann, J. Takeya (CRIEPI, Tokyo, Japan), C. Krellner, S. Haas, K. P. Pernstich, D. J. Gundlach and

B. Batlogg, in collaboration with the group of Prof. Y. Iwasa, Sendai, Japan, the group of Prof. K. Ensslin, ETH Zurich, and the group of Dr. J. Gobrecht, PSI Villigen

We study the transport of field-induced charge in organic molecular crystals using a flip-crystal technique, in which the crystal is placed on a prefabricated substrate at the end of the device fabrication process. This method minimizes crystal handling and avoids direct processing of the crystal that may degrade the FET electrical characteristics. We have further improved the device quality: a modified substrate cleaning procedure and chemical substrate treatment has led to a reliable device fabrication process with a good reproducibility of the FET results. Moreover, the charge carrier mobilities have increased considerably even without major improvements in the crystal growth procedure. The highest room temperature hole mobilities measured so far are greater than $10 \text{cm}^2/\text{Vs}$ for rubrene and greater than $1 \text{cm}^2/\text{Vs}$ for tetracene and pentacene devices. Even

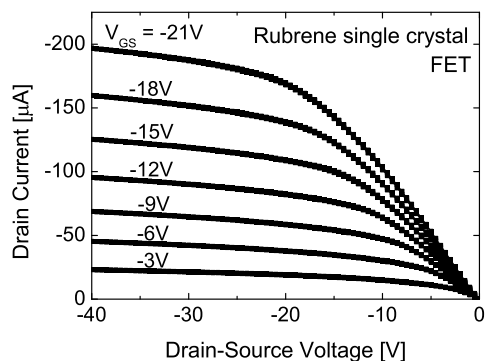


Figure 1.2: Output characteristics of a rubrene device.

in these high-mobility devices, trapping of charge carriers is still present at room temperature. A clear improvement in the transport properties can be expected from progress in the crystal growth technique, especially the chemical purity of the crystals. Work in this direction is currently in progress.

In a collaboration with the group of Prof. Y. Iwasa (Sendai, Japan) and Dr. J. Takeya (CRIEPI, Tokyo, Japan), self-assembled monolayers (SAMs) of various organic molecules have been deposited on the prefabricated substrates. The influence of these SAMs on the transport properties has been studied. A clear change in the switch on voltage has been found, resulting from the induction of additional holes inside the organic crystal by fluoro-terminated SAMs.

1.1.3 Bulk doping of pentacene single crystals

S. Haas, Ch. Bergemann¹, B. Batlogg

One approach to induce charge in organic molecular semiconductors is bulk chemical doping with intercalated charge donors.

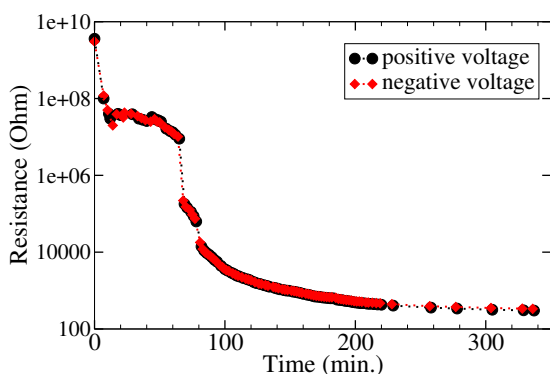


Figure 1.3: Resistance of a pentacene crystal as function of the doping level. Note: The intercalation of iodine was slowed down after 15 minutes and accelerated again after one hour by adjusting the partial pressure of I_2 .

The intercalation of iodine in pentacene (Pc) single crystals is measured in-situ and time resolved by the means of X-ray diffraction and simultaneous four- and two-terminal electrical resistivity measurements. The iodine vapor pressure was varied between 0.03 and 0.26 torr, while the samples were mostly held at room temperature. Intercalating iodine enhances the interlayer spacing (d_{001}) from 14.1 Å in pure pentacene to 19.2 Å. The resistivity is decreased by many orders of magnitude, from 10^8 – 10^9 Ω-cm in the pure pentacene crystal to about 1 Ω-cm for partially or completely intercalated samples. The iodine is de-intercalated by continuous pumping and sample heating.

1.1.4 Temperature dependent structure parameters of pentacene single crystals

S. Haas, T. Siegrist (Bell Labs, Murray Hill NJ), B. Batlogg

Temperature dependent structure parameters of pentacene single crystals were measured for temperatures between 25 and 150 °C. The crystal was held in a stream of preheated nitrogen gas. While the thermal expansion is most pronounced in b - and c -direction with thermal coefficients of $(139 \pm 2) \times 10^{-6} \text{K}^{-1}$ and $(108 \pm 2) \times 10^{-6} \text{K}^{-1}$, respectively, the a -axis contracts with increasing temperature, resulting in a negativ thermal coefficient of $-(19.9 \pm 0.7) \times 10^{-6} \text{K}^{-1}$. The bond lengths within the molecules remain constant. The overall expansion and the different behaviour of the a - and b -axis are mainly caused by a rotation of the molecule in $(\frac{1}{2} \frac{1}{2} 0)$.

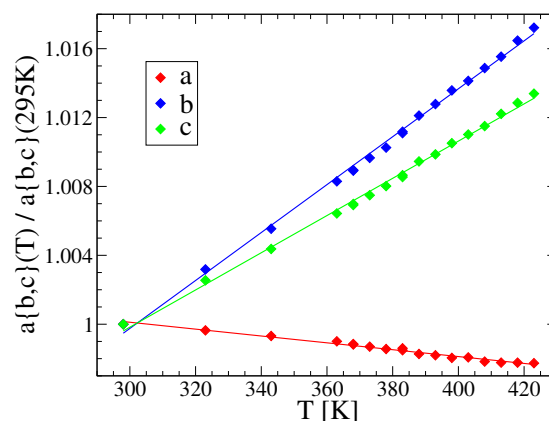


Figure 1.4: Relative change of the lattice constants in pentacene with temperature.

¹current address: Cavendish Lab., University of Cambridge, UK

1.2 Organic thin film transistors

1.2.1 Threshold Voltage Shift by Surface Modification of the Gate Insulator in Pentacene TFTs

K. P. Pernstich, S. Haas, D. J. Gundlach, B. Batlogg

A. N. Rashid - Nonlinear Optics Laboratory, ETH Zurich

G. Schitter - Nanotechnology Group, ETH Zurich

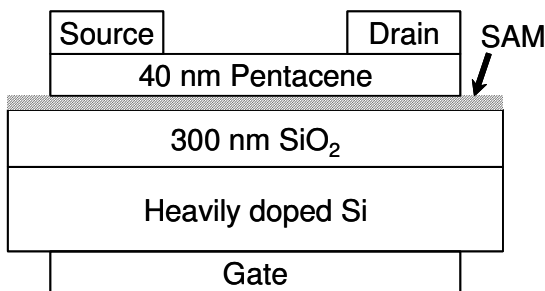


Figure 1.5: Schematic cross section of the pentacene TFTs.

The goal of this study is to investigate the influence of the gate insulator preparation on the electrical parameters of pentacene thin film transistors (TFTs). Therefore we fabricated pentacene TFTs on conducting silicon wafers with a silicon dioxide layer on top (cf. Fig. 1.7). In this configuration the wafer acts as the gate electrode and the SiO_2 as the gate insulator of the field effect transistor. Prior to the pentacene deposition we covered the SiO_2 with nine different self assembled monolayers (SAMs) formed by organosilanes. Those organosilane molecules have different functional groups and possess a permanent electric dipole field. This dipole field has the same effect than applying a gate bias, therefore mobile charge carriers are

present in the pentacene channel even at zero gate bias.

The presence of mobile charge carriers at zero gate bias can be observed in the transfer characteristic of TFTs with four different surface treatments shown in Fig. 1.6. At $V_g = 0$ V a substantial drain current I_0 is flowing for treatments (A), (C) and (F) while only the off-current flows for treatment (G). I_0 is marked in the figure for treatment (A). The SAM induced carrier density can be up to $4 \times 10^{12}/\text{cm}^2$ which is comparable to the carrier density of $6 \times 10^{12}/\text{cm}^2$ that can safely be induced by the gate bias without breakdown in the SiO_2 .

An important parameter for device operation, is the so called switch-on voltage. It is marked in Fig. 1.6 as V_{so} and indicates the gate voltage at which mobile majority carriers start to accumulate in the channel, raising the drain current above the off-current (flat band condition). In our experiments we could show that this switch-on voltage is determined by the surface potential of the gate insulator and can be modified by the incorporation of SAMs with various functional groups.

A second important parameter is the threshold voltage of the TFT (not shown). The measurements show a shift of the threshold voltage but at a different rate than the switch-on voltage. This is an indication for different trap concentrations in the band gap. Looking at the subthreshold behaviour (not shown) we could indeed identify those differences quantitatively.

All together we have presented a way to controllably shift the threshold voltage and the switch-on voltage in pentacene TFTs, which can be of importance for designing circuits.

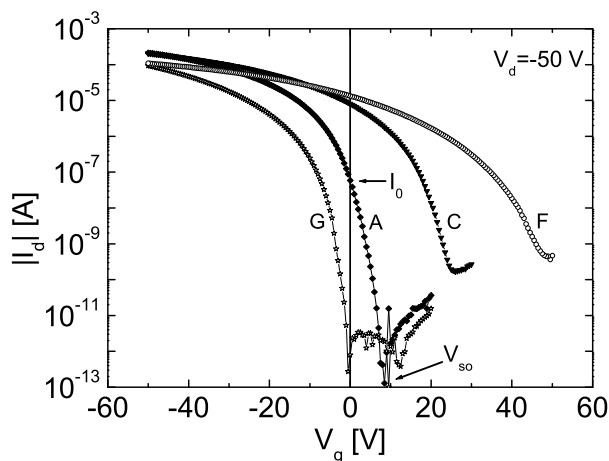


Figure 1.6: Transfer characteristic of TFTs with four different SAMs. The switch-on voltage shifts for the particular SAM and the increase in drain current at zero gate bias indicates the presence of mobile charges induced by the SAM.

1.2.2 Modeling and parameter extraction on Pentacene Thin Film Transistors (Pc-TFTs)

D. Oberhoff, K. P. Pernstich, D. J. Gundlach, B. Batlogg

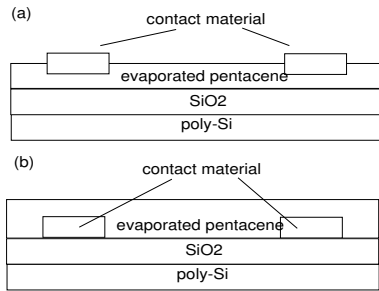


Figure 1.7: Schematic cross section of the pentacene TFTs in top (a) and bottom (b) contact configuration.

the TFT.

Organic thin film transistors behave in many regards similar to devices made of inorganic semiconductors such as silicon. In detail however they differ due to peculiarities of the electronic properties of organic thin films. In order to extract those properties we are fabricating devices in the configurations shown in figure 1.7 and developing a numerical simulation strategy to incorporate as much knowledge of the underlying physical system as possible.

A prototype implementation based on the steady state equivalent circuit shown in figure 1.8 allows for the definition of and includes an arbitrary density of states (DOS), grain boundary effects, and interface effects at the contacts and at the gate interface. It incorporates a numerical solution of the 1d-poisson-equation at the gate interface to determine the trapped and free charge density in the channel of

An array of measurement techniques and extraction methods have been investigated and/or developed allowing for the creation of a viable scenario and subsequently physically based exact modelling (90percent accuracy in output and transfer curves as well as C-V-curves in most cases). Further measurements, such as the temperature dependence of the electrical properties, will put additional constraints on the parameters used in the models.

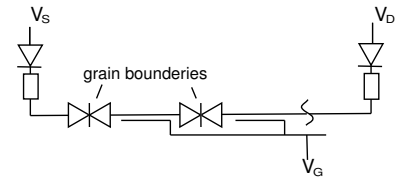


Figure 1.8: equivalent circuit of the 1d steady state model

1.3 Correlated electrons on a triangular lattice: Na_xCoO_2

1.3.1 Synthesis and structural investigations of Na_xCoO_2

S.Kazakov, J.Jun, J.Karpinski, B. Batlogg (in collaboration with D.Sheptyakov of PSI)

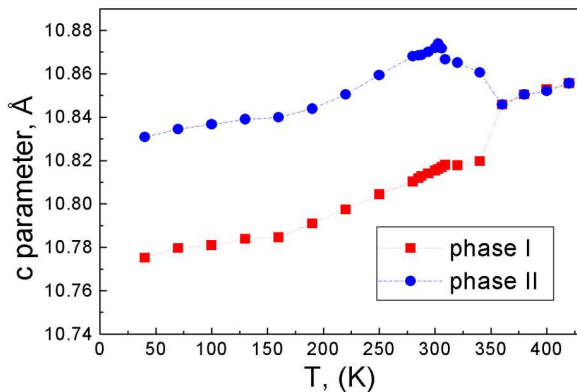


Figure 1.9: Temperature dependence of the c -parameter for a $\text{Na}_{0.79}\text{CoO}_2$ sample. Synchrotron powder diffraction study of $\text{Na}_{0.70}\text{CoO}_2$ showed the splitting of some reflections indicating the lowering of symmetry.

In contrast to the cuprates with corner-sharing CuO_2 square plaquettes, the CuO_2 layers are formed by edge-sharing octahedra, resulting in a triangular Cobalt arrangement. We have performed the synthesis and structural investigations of samples Na_xCoO_2 with different sodium content ($x = 0.5 - 0.9$). Temperature dependent neutron powder diffraction study of $\text{Na}_{0.79}\text{CoO}_2$ showed phase separation, i.e. the presence of two phases with the same structure but different lattice parameters and sodium content. This separation occurs at about 340 K (shown on Fig.1.9 where the temperature dependence of c -parameter of two phases is plotted). Single crystals of Na_xCoO_2 have been synthesized from the solution in NaCl. The crystals have size up to $5 \times 5 \text{ mm}^2$. The investigations of properties of the crystals are in progress.

1.3.2 Low-energy electronic states in triangular Na_xCoO_2

M. Brühwiler, B. Batlogg, S.M. Kazakov, J. Karpinski

The structure of Na_xCoO_2 is similar to the high-temperature superconducting cuprates. However, one main difference is the symmetry of the lattice formed by the metal ions: While the Co in Na_xCoO_2 form a triangular lattice, the Cu atoms in the cuprates make up a square array. This is a result of the CoO_6 octahedra being tilted and therefore the metal and oxygen layers are well separated in Na_xCoO_2 . The compound has low-temperature properties that suggest strong correlations between electrons, and superconducts below 5 K when intercalated with water. As a consequence, the compound is of great interest for both theorists and experimentalists alike. Furthermore, the material is a promising candidate for thermoelectric applications, due to its low electrical resistivity, low thermal conductivity and large thermopower.

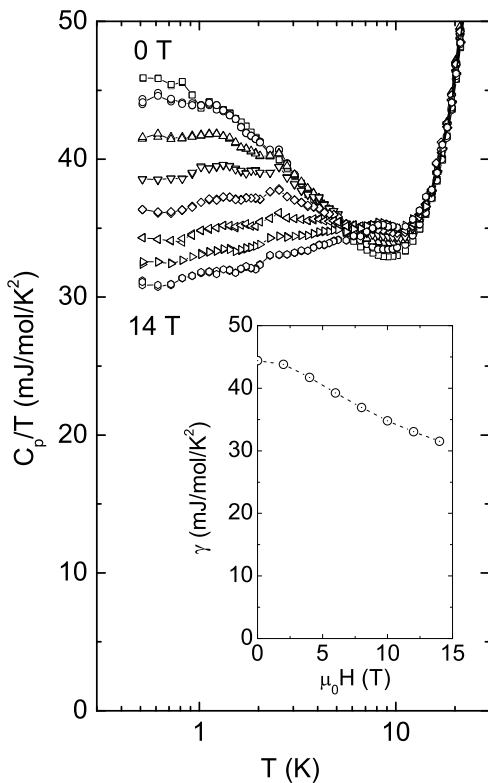


Figure 1.10: Heat Capacity $C_p(T)$ as a function of temperature for magnetic fields from 0 T to 14 T. The electronic specific heat coefficient $\gamma = \lim_{T \rightarrow 0} C/T$ as a function of magnetic field H is shown in the inset. γ is extracted from heat capacity data below 0.8 K. γ is suppressed by a magnetic field resulting in a reduction of the effective mass by 30 % in a 14 T field.

To elucidate the basic electronic properties of the triangular lattice, we have measured the electrical resistance $R(T)$ and specific heat $C_p(T, B)$ down to 0.5 K in magnetic fields up to 14 T. For $x = 0.7$, we find a highly unusual low-energy excitation spectrum. $R(T)$ increases sub-linearly with temperature in zero field and is enhanced significantly by a magnetic field. This is in sharp contrast to Landau Fermi-liquid behavior found in ordinary metals.

The coefficient of the electronic specific heat $\gamma = C_p/T$ increases at temperatures below about 10 K, giving a low-temperature value of $\gamma = 45 \text{ mJ/mol/K}^2$. This is roughly 10 times the γ of a typical transition-metal, but still 20 times smaller than heavy-Fermion materials. The low-temperature enhancement of γ is suppressed by a magnetic field resulting in a reduction of the effective mass by 30 % in a 14 T field. Comparison to magnetization measurements reveal that the field dependent effective mass might be due to magnetic fluctuations. This picture is supported by the proximity to a magnetic ground state as determined experimentally and predicted by calculations of the band structure.

It remains to be seen, if the peculiar properties of this material system are a direct result of the triangular structure. In any case, the characterization of this oxide promises to provide new insight into the physics of correlated electron systems.

1.4 SiGe modulation doped heterostructures

B. Rössner, H. von Känel

in collaboration with D. Christina, G. Isella (Polytecnico di Milano)

The growth of SiGe heterostructures with a pure Ge channel suffers from the need to combine high growth rate for buffer deposition and near monolayer precision for the electrically active structure. Usually a two-step technique is

needed. The LEPECVD process which is especially suitable for growth of graded buffers was adapted to accommodate the precision requirements. P-Modulation Doped (p-MOD) heterostructures were grown without growth interruption using the LEPECVD process.

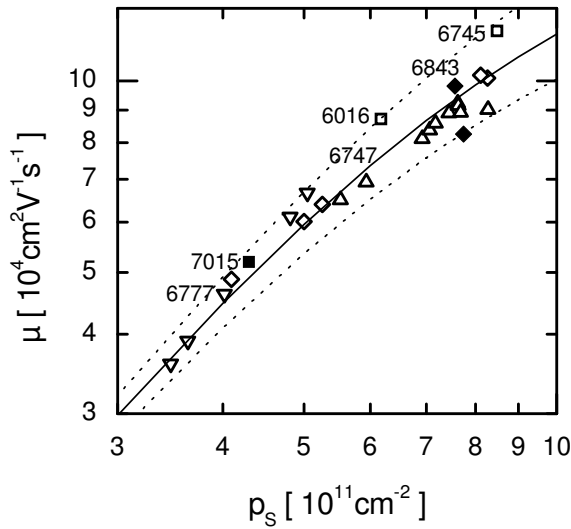


Figure 1.11: Carrier mobility of pure Ge channel p-MODs on a $\text{Si}_{0.3}\text{Ge}_{0.7}$ substrate at $T=2\text{K}$. It increases with carrier density, indicating predominance of impurity scattering. Open symbols: van der Pauw squares, closed symbols: Hall bars

$120.000 \text{ cm}^2/\text{Vs}$, the corresponding carrier density was $8.5 \times 10^{11} \text{ cm}^{-2}$. The sample set a new record for SiGe heterostructures.

The method allows a very low grading rate of the relaxed SiGe buffer (7% Ge per μm) and a thick ($2 \mu\text{m}$) constant composition layer underneath the electrically active layer stack. Thus it is possible to reduce both the dislocation density and the surface roughness of the buffer layers, rendering these sources of carrier scattering unimportant. Strained channel quality was improved by careful growth temperature selection and the use of H_2 as a surfactant, delaying the onset of 3-dimensional growth.

The relationship of carrier density to carrier mobility was investigated by growing a series of structurally identical samples. Only the amount of remote doping was changed from sample to sample. Although this method inevitably introduces slight variations in sample quality, it was chosen to circumvent the need for gated structures.

The results reveal the functional dependence of the carrier mobility on the carrier density. At low sheet densities, we find $\mu \propto p_s^{1.6}$ which is typical for remote impurity scattering. At higher carrier densities, impurity scattering lowers the achievable mobility. The highest hole mobility achieved at a temperature of 4.2 K was

1.5 Materials synthesis and high pressure crystal growth

The main activity has been related to investigations of pure and substituted MgB_2 and $\text{Al}_x\text{Ga}_{1-x}\text{N}$ single crystals. Other investigated materials are: Na_xCoO_2 , $\text{YBa}_2\text{Cu}_4\text{O}_8$, Hg-1201 and crystals of related compounds grown in our laboratory. Most investigations have been performed on single crystals due to the fact, that the investigated compounds are structurally highly anisotropic.

1.5.1 Growth of MgB_2 single crystals

S.Kazakov, J.Jun, N.Zhigadlo, J.Karpinski

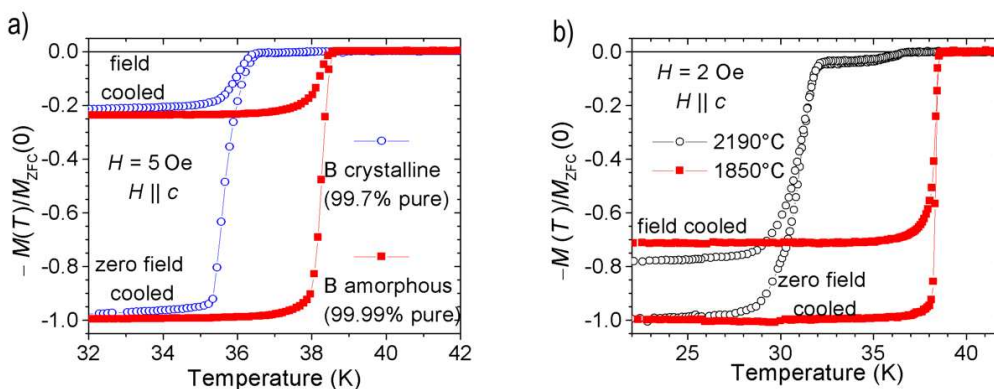


Figure 1.12: a) Magnetization curves of two MgB_2 crystals grown from boron of various purity using the same growth conditions b) Magnetization curves of two MgB_2 crystals obtained in a similar processes with various maximum temperatures.

Crystal growth process of MgB_2 takes place at high pressure of 30 kbar at temperatures of 1850–2000 °C. Molten Mg and its vapors are very reactive and we had to overcome the problems of impurities, doping and non-homogeneities created in crystals during the growth. Figure 1.12 a) shows the influence of the purity of precursors on the critical temperature. The magnetization curve of the crystal grown at 2190 °C shows a two-step transition with a lower onset T_c (Fig. 1.12b)) due to the formation of defects and lower Mg occupation of 90% in this crystal.

1.5.2 Substitution of carbon and aluminum in superconducting MgB_2

N.Zhigadlo, S.Kazakov, J.Jun, J.Karpinski, (in collaboration with R.Puzniak and A.Wisniewski of the Institute of Physics PAS in Warsaw, A.Mironov of the Moscow State University and G. Schuck of the Crystallography Department ETH)

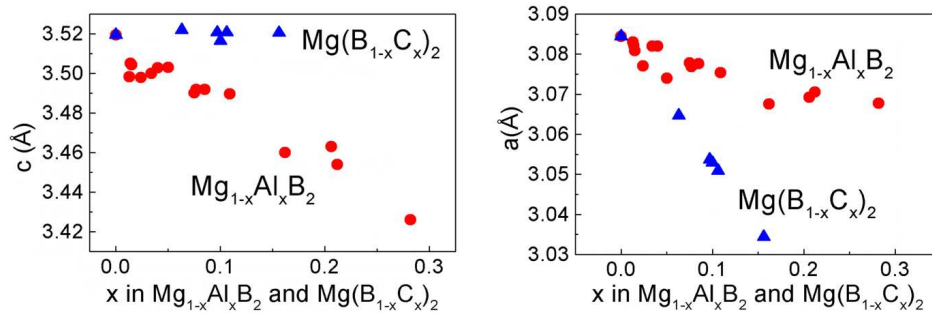


Figure 1.13: Structural parameters a and c of MgB_2 single crystals as a function of Al and C content.

Al and C substitution affect the MgB_2 structure differently. Figure 1.13 shows the lattice parameters as a function of Al and C content. Carbon substitution for boron decreases a lattice parameter, leaving c unaffected, aluminum substitution for magnesium leads to a decrease of the c lattice parameter and influences a only a little. This is related to the difference in bond strengths. The B-B bonds in the basal plane are much stronger than the Mg-B bonds. The critical temperature dependence on carbon content is shown in Fig. 1.14.

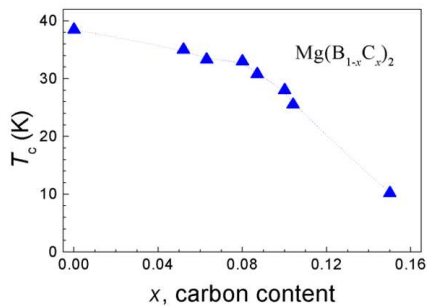


Figure 1.14: Variation of T_c as a function of carbon concentration.

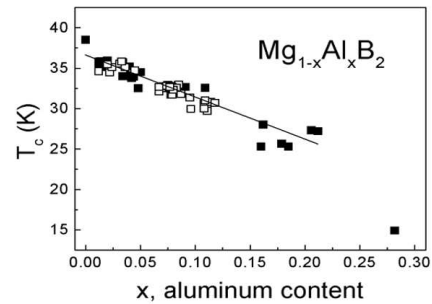


Figure 1.15: T_c dependence on Al content in $\text{Mg}_{1-x}\text{Al}_x\text{B}_2$ crystals grown at $T=1860^\circ\text{C}$: (■) and $T=1960^\circ\text{C}$: (□).

Structure investigations of MgB_2 crystals with carbon substitution for boron show elongations of the reflections in the c^* direction, which indicates inhomogeneities of carbon distribution. Torque investigations prove the existence of flux pinning in the field configuration close to the $H//c$ -axis effective up to 9 T. This leads to an enhancement of the critical current and cause the observed increase of the upper critical field in $\text{Mg}(\text{B}_{1-x}\text{C}_x)_2$ with a modest decrease of T_c . Samples of $\text{Mg}_{1-x}\text{Al}_x\text{B}_2$ show phase separation for $x>0.1$ This makes crystal growth of single phase $\text{Mg}_{1-x}\text{Al}_x\text{B}_2$ crystals very difficult. X-ray diffraction studies show that the second phase segregates as MgAlB_4 layers perpendicular to c -axis of the crystal. Careful modification of crystal growth procedure with slow cooling allowed us to grow crystals without precipitation up to $x \sim 0.11$. Figure 1.15 shows the T_c dependence on Al content measured by EDX. The experimental points form a band pointing towards $T_c = 36.5$ K and not $T_c = 38.5$ K as in pure MgB_2 crystals.

Therefore, even small, 1% Al concentration seems to introduce defects in the structure, which decreases T_c to 35 K.

The limiting factor for possible applications of MgB_2 is a low H_{c2} . Carbon substitution appears to improve the situation. Magnetic torque investigations of carbon substituted MgB_2 single crystals show a large increase of H_{c2} and a decrease of the anisotropy (Fig. 1.17). The increase of upper critical field in substituted compounds is accompanied with the significant development of a sharp peak in the irreversible torque at the fields / angles close to the upper critical field / angle. The peak develops with increasing magnetic field and decreasing temperature [see Fig. 1.16]. The peak amplitude expands in a magnetic field of 70 kOe to values of almost one order of magnitude higher than the value of reversible torque signal. The peak effect is due to a disorder-induced phase transition of vortex matter.

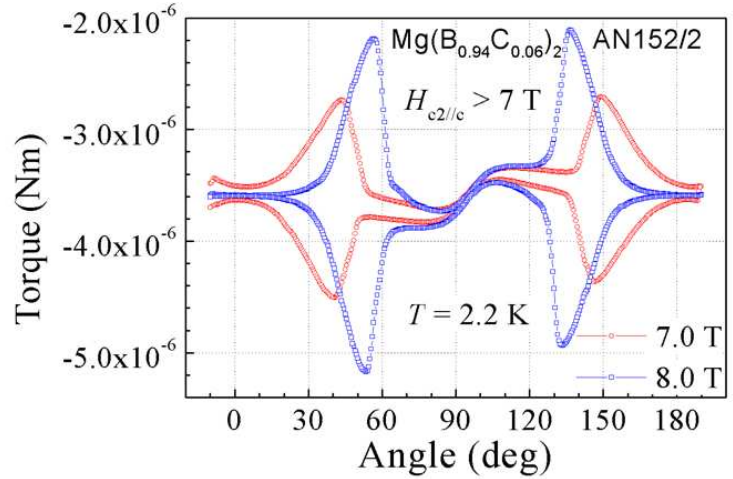


Figure 1.16: Torque τ versus angle θ between the applied field and the c-axis of a $\text{Mg}(\text{B}_{0.94}\text{C}_{0.06})_2$ single crystal. At 7 T the crystal is in superconducting state for all angles (torque signal is non-zero). At 8 T for 0° angle the crystal is in the normal state (torque signal is zero)

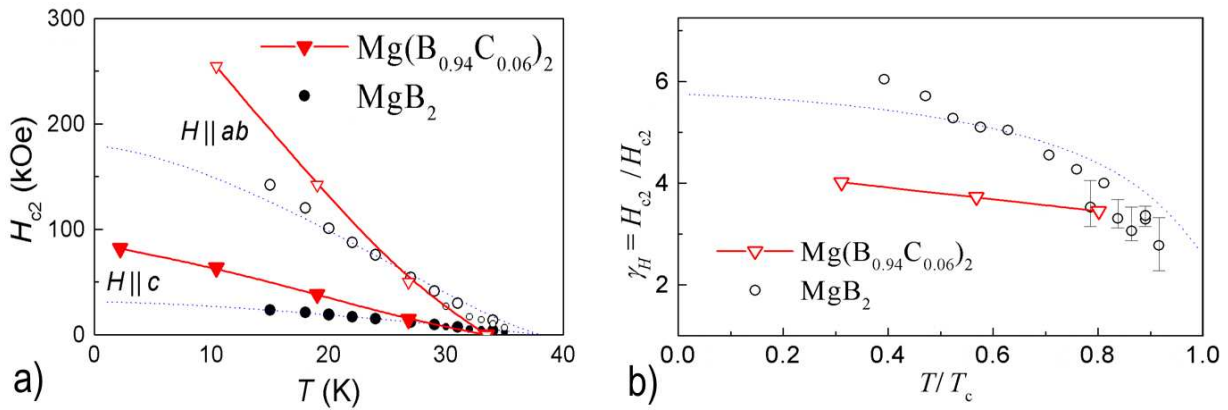


Figure 1.17: a) Upper critical field H_{c2} vs temperature T for $\text{Mg}(\text{B}_{0.94}\text{C}_{0.06})_2$ (full symbols) and for MgB_2 (open symbols). b) Reduced temperature T/T_c dependence of the upper critical field anisotropy $\gamma_H = H_{c2}^{\parallel ab} / H_{c2}^{\parallel c}$.

Substitution of Al and C in the structure of MgB_2 influences the electronic structure and the superconducting energy gaps. Point contact spectroscopy investigations have been performed in collaboration with R. Gonnelli of Politecnico Torino. The application of a magnetic field allowed for a separation of the contributions of the σ and π bands and the temperature dependence of each gap can be measured. The magnetic field dependency of the gaps has also been measured. The vanishing of the π -band contribution was observed at a field above 1 T. The investigation of Al and C substituted crystals led to unexpected result, that the merging of the gaps is absent.

1.5.3 Copper-oxides

$\text{HgBa}_2\text{CuO}_{4+\delta}$

Single crystals of this compound have been grown at a high pressure of 10 kbar at $T = 1000^\circ\text{C}$. In collaboration with Prof. H. Weber of Atom Institute in Vienna the investigations of superconducting parameters have been performed as a function of oxygen content. Irreversible properties have been investigated as a function of neutron irradiation. Large

enhancement of J_c and irreversible magnetic moment together with a decrease of anisotropy have been observed after neutron irradiation.

$\text{YBa}_2\text{Cu}_4\text{O}_8$

Single crystals have been grown at high oxygen pressure of 700 – 1000 bar at $T = 1100^\circ\text{C}$. $\text{YBa}_2\text{Cu}_4\text{O}_8$ is a stoichiometric superconductor with a reduced T_c (due to "underdoping"), what makes it exceptional among the superconducting cuprates. $\text{YBa}_2\text{Cu}_4\text{O}_8$ seems to be an ideal candidate for investigations if in underdoped superconductor holes can become concentrated at certain locations resulting in hole-rich superconducting domains. These investigations are running now in collaboration with various scientific groups.

1.5.4 Growth of $\text{Al}_x\text{Ga}_{1-x}\text{N}$ single crystals

P. Geiser, J. Jun, P. Wägli, S.M. Kazakov, L. Klemm (Institute for Isotope Geochemistry and Mineral Resources), J. Karpinski, B. Batlogg

We designed a new experimental setup for the growth of GaN and $\text{Al}_x\text{Ga}_{1-x}\text{N}$ bulk single crystals. A cubic anvil cell with solid pressure medium is used to reach temperatures as high as $T = 1850^\circ\text{C}$ and pressure up to 35 kbar. Gold capsules contain the precursors and GaN powder serves as nitrogen source. Growth takes place in a melt consisting of Al, Ga and Au. Fig. 1.18 shows a crystal grown in a 45 hrs process. X-ray diffraction confirms the $\text{Al}_x\text{Ga}_{1-x}\text{N}$ phase and indicates an Al content in $\text{Al}_x\text{Ga}_{1-x}\text{N}$ of $x_{XRD} = 0.24$, based on Vegard's law. This result is crosschecked by energy dispersive X-ray investigations (EDX). From lateral EDX scans we find that the Al content is high in the nucleation zone forming at the beginning of the process (zone A, fig. 1.18). The high Al content ($x_{EDX} = 0.3$) is confirmed for this area. Following a line from A to B in fig. 1.18 a continuous decrease of Al from $x = 0.3$ to $x = 0$ is found.

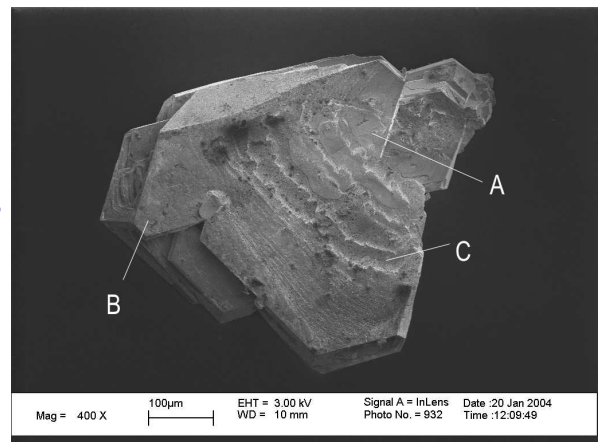


Figure 1.18: A) Nucleation zone B) GaN grown at the end of the experiment. C) Growth steps.

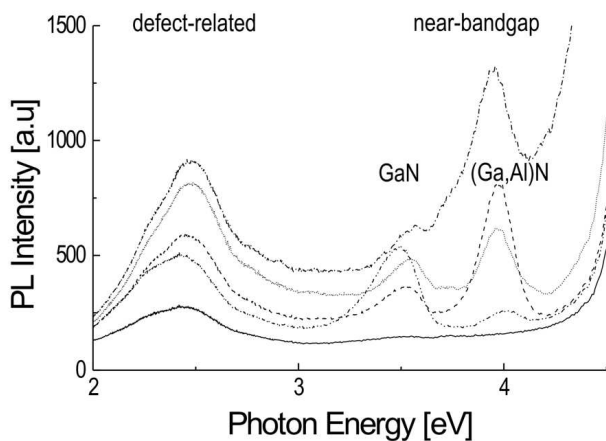


Figure 1.19: PL spectra of an $\text{Al}_x\text{Ga}_{1-x}\text{N}$ crystal measured at various spots between areas A and B (see fig. 1.18) The near bandgap transition shifts from $\sim 3.5\text{eV}$ in the Al free part of the crystal towards higher energy ($\sim 4\text{eV}$) in the Al rich part, quantitatively consistent with the increase of the bandgap upon Al substitution. The luminescence peaks near 2.5eV are associated with deep level defects.

Photoluminescence (PL) at room temperature is used to further study the Al concentration. Figure 1.19 shows several spectra when the focused laser (266 nm) is scanned along the A-B-line with a step width of $\sim 70\ \mu\text{m}$. The blueshift of the near bandgap transition is not continuous as it would be expected from the EDX data. Depth profiles measured with Laser Ablation Mass Spectroscopy have to be taken into account. All results indicate consistently, that the $\text{Al}_x\text{Ga}_{1-x}\text{N}$ bulk crystal is overgrown by a thin GaN capping layer. The thickness of this layer is increasing along $A \rightarrow B$. It remains to be clarified if the Al-free layer forms due to a lack of Al in the melt, or due to a drastically reduced solubility of Al at lower temperatures encountered during cool-down of the furnace.

1.5.5 GaN films grown by MBE on GaN bulk single crystal substrates

P. Geiser, D. Ebling (FIRST Lab. ETHZ), F. Pirovino (Institute for Geology ETHZ), J. Karpinski, B. Batlogg

Bulk single crystals of GaN (up to $5 \times 3 \times 0.5 \text{ mm}^3$) have been grown under high nitrogen pressure. The conditions reach up to $T = 1550^\circ\text{C}$ and $p = 13 \text{ kbar}$. The wurtzite GaN crystal (0001) and (000 $\bar{1}$) faces are of interest for homoepitaxial layer growth. As the crystal lattice is polar, the surface morphology is different for these two faces. The (0001) or Ga-face is known to be rough compared to the (000 $\bar{1}$) or N-face. We use this for an indirect determination of the crystal orientation by scanning the surface with an AFM. The oriented crystals are mechanically polished with a grain size down to $0.25 \mu\text{m}$. Polishing introduces a substantial amount of subsurface damage which we remove with a chemically assisted plasma etch using a $\text{Cl}_2/\text{CH}_4/\text{Ar}$ plasma. Crystals with both (0001) and (000 $\bar{1}$) orientation and different surface treatment (mechanically polished and/or plasma etched) were used as substrates for GaN MBE homoepitaxy. The crystals are mounted on a Al_2O_3 carrier, covered with 500 nm GaN as a protective layer. Then 500 nm of GaN are deposited on the GaN substrate crystals in a second step. Figure 1.20 shows the different layer morphologies. It is found, that for the Ga face (0001) the RMS roughness remains constant. For the N face (000 $\bar{1}$) the RMS roughness is increasing with every additional step of preparation.

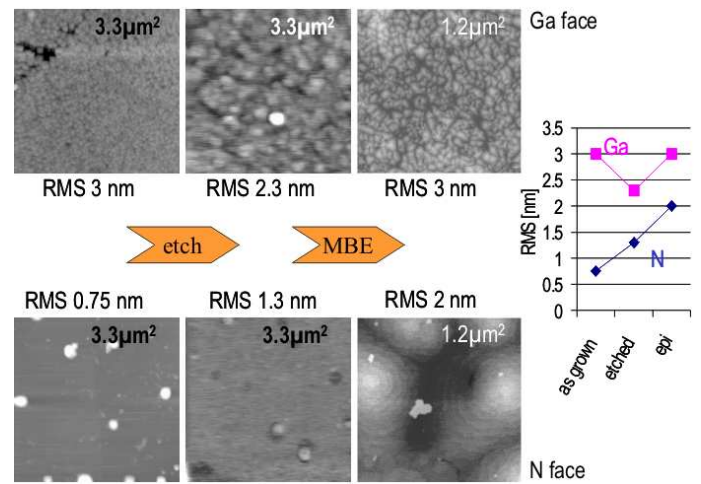


Figure 1.20: RMS roughness of GaN layers homoepitaxially grown by MBE. Dependence on crystal orientation and substrate preparation. The shown data are from samples not polished before the plasma etch.

1.5.6 Investigations performed in collaboration with other researchers

Detailed reports are found in the publications

- Magnetic torque investigations on MgB_2 in collaboration with Dr. R. Puzniak and Dr. A. Wisniewski (Institute of Physics PAS in Warsaw) and Prof. H. Keller (Physik Institut Uni Zürich).
- De Haas-van Alphen effect on MgB_2 (J.R. Cooper, University of Cambridge; A. Carrington, University of Bristol).
- Scanning tunneling spectroscopy (STS) investigations on MgB_2 (in collaboration with the group of Prof. Ø. Fischer of the University of Geneva).
- Point contact spectroscopy on MgB_2 pure and substituted with Al and C (in collaboration with Dr. R. Gonnelli, Politecnico di Torino)
- Irradiation defect effects of neutrons on MgB_2 (in collaboration with Prof. H. Weber Atom Institute in Vienna).
- Structural investigations on MgB_2 single crystals (in collaboration with Dr. A. Mironov, Moscow State University).
- Small Angle Neutron Scattering (SANS) studies (in collaboration with Dr. R. Cubitt of ILL in Grenoble and Dr. M. Eskildsen of University of Geneva).
- Phonon dispersion by inelastic X-Ray Scattering on MgB_2 (in collaboration with Dr. A. Shukla of Laboratoire de Minéralogie Cristallographie, Université Pierre et Marie Curie, Paris Cedex).

- Proton irradiation effects on MgB_2 (in collaboration with Prof. D. Caplin of Imperial College, London).
- Thermal conductivity of MgB_2 (Dr. A. Sologubenko/Prof. H.R. Ott, Laboratory for Solid State Physics, ETH Zürich)
- Picosecond spectroscopy on MgB_2 (Prof. R. Sobolewski, Dept. Electr. And Comp. Eng., Rochester Univ. USA).
- Magnetic decoration experiments on MgB_2 (Prof. L. Vinnikov, Chernogolovka).
- Isotope effects, muon spin resonance: on cuprates and MgB_2 Prof. H. Keller, Physik Institut, Uni Zürich.
- Nuclear Magnetic Resonance on Na_xCoO_2 : Dr. J. Gavilano/ Prof. H.R. Ott, Laboratory for Solid State Physics ETH.
- Magneto-thermopower measurements on MgB_2 , Dr. T. Plackowski/ Dr. C. Sulkowski, Institute of Low Temperature and Structure Research, Wroclaw, Poland.

Chapter 2

Physics of mesoscopic structures, semiconductor nanostructures

(<http://www.nanophys.ethz.ch>)

Head

Prof. Dr. K. Ensslin

Academic Staff

A. Baumgartner

A. Dorn

C. Ellenberger

Dr. A. Fuhrer

Dr. B. Simovic

D. Graf

B. Grbic

PD Dr. T. Ihn

Dr. S. Kicin

Dr. R. Leturcq

A. Pioda

Dr. R. Schleser

M. Sigrist

Technical Staff

C. Barengo

P. Studerus

Administrative Staff

B. Abt

2.1 Electric field tuned singlet-triplet transition in quantum rings

A. Fuhrer, T. Ihn, and K. Ensslin, in collaboration with W. Wegscheider (Uni. Regensburg), M. Bichler (Walter-Schottky Institute of the TU München)

The experimental spectrum of a Coulomb-blockaded many electron quantum ring shows many features of the theoretically expected single-particle level spectrum and individual states can be identified by their angular momentum quantum number. The peak positions are interpreted in a constant interaction picture and we find that a perturbation of the rotational symmetry leads to states with a more localized wavefunction. This is in contrast to the pure angular momentum states that extend around the ring and show a pronounced zig-zag behavior as a function of magnetic field. Here we report a new set of experiments where we investigate deviations from the constant interaction picture in detail. The fact that localized and extended states show clearly different dispersions as a function of asymmetrically applied gate voltages allows us to induce degeneracies between orbital levels where fluctuations in the Hartree interaction and exchange effects become important. Moreover, this allows to draw conclusions about the evolution of the ground state spin of this many-electron quantum ring.

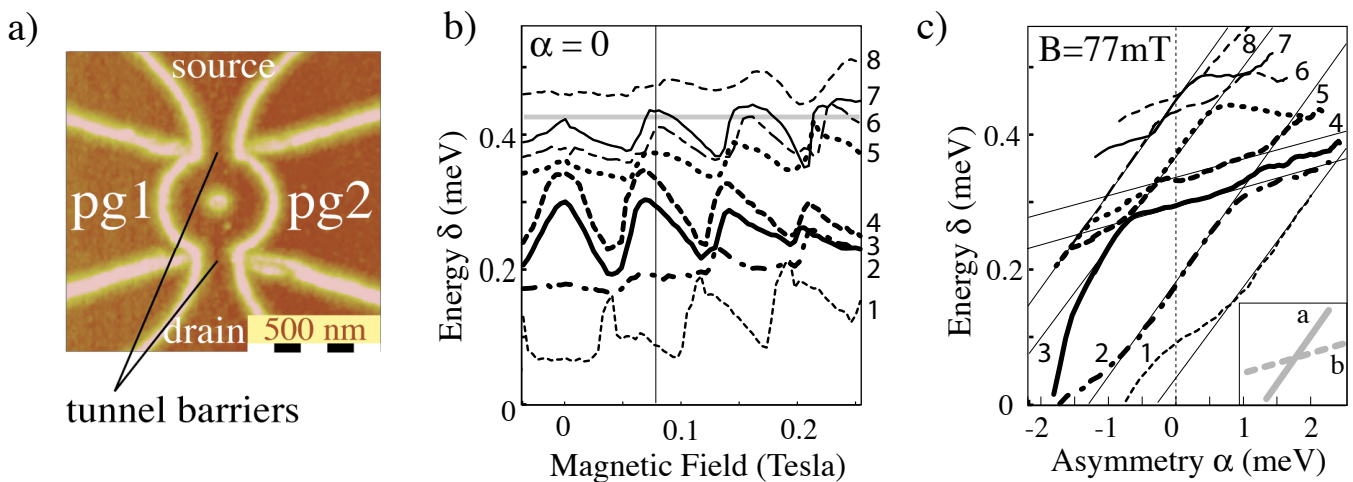


Figure 2.1: (a) AFM micrograph of the quantum ring sample. The tunnel barriers are tuned using a homogeneous metallic top gate in addition to the four in-plane gates flanking the plunger gates pg1 and pg2. The number of electrons and the symmetry between the arms is adjusted by applying appropriate voltages to the side gates pg1 and pg2. (b) and (c) Addition spectra after a constant energy was subtracted from the peak separation. The dashed of the lines identifies peak positions with the same number of electrons on the ring. Inset in (c) Schematic of the characteristic slopes of 'localized' **a** and 'extended' states **b**.

The two-terminal ring structure [see Fig. 2.1(a)] was fabricated on a high mobility shallow Ga[Al]As heterostructure by AFM-lithography. Two in-plane plunger gates (pg1 and pg2) allow to tune the number of electrons and the left/right symmetry of the ring. The ring has an average radius of $r_0 = 132$ nm and we estimate that it contains more than 60 and less than 200 electrons. Measurements were performed in a dilution refrigerator at a temperature of 100 mK.

We define an asymmetry parameter $\alpha(V_{pg1}, V_{pg2}) = \delta_{pg1}(V_{pg1}) - \delta_{pg2}(V_{pg2})$. Figure 2.1(b) and (c) show the resulting spectra as a function of perpendicular magnetic field and asymmetry. The peaks are numbered with increasing energy δ .

In Fig. 2.1(b) the positions of many conductance peaks oscillate as a function of magnetic field B applied normal to the plane of the electron gas, reflecting the magnetic field dispersions of states with well defined angular momenta. These states frequently occur as so-called spin-pairs, i.e. pairs of neighboring conductance peaks moving in parallel (see for example peaks 3 and 4). On two such conductance peaks the current is carried by the same orbital state and beyond the second peak the two topmost electrons have opposite spins like in a singlet state. The strongly oscillating magnetic field dispersion associated with a well-defined angular momentum for these states is characteristic for a wavefunction which is extended around the ring.

In contrast, we also find conductance peak positions with a flat magnetic field dispersion (see for example peak 2) that

have been previously identified as states that originate in the mixing of different angular momentum states at small energies of a higher radial subband when the rotational symmetry of the ring is broken. In a realistic ring structure the symmetry is always slightly perturbed, e.g., due to an inherent asymmetry between the two arms of the ring and we find that the wavefunctions of such mixed states no longer extend around the ring. Thus, we refer to such states as 'localized' states in the following, in contrast to the strongly oscillating 'extended' states .

The asymmetry allows us to induce crossings between extended and more localized states. This is due to the fact that a state which is more localized in one arm of the ring will depend more strongly on asymmetrically applied gate voltages, while a state extended around the ring will be only slightly shifted. Fig. 2.1(c) shows the measured spectrum as a function of asymmetry and the expected slopes of the two crossing orbitals are shown in the inset. At zero asymmetry ($\alpha = 0$) level **a** is filled with a first electron (peak 2) fills the lower of the two levels leading to a kink in the peak position at the crossing ($\alpha \approx 1$). Far away from the crossing ($\alpha \approx -1$) the second electron fills the same orbital level forming a singlet with the first electron. As the asymmetry is tuned we our findings indicate a transition from a singlet to a triplet back to a singlet state between peaks 3 and 4 in the asymmetry range where the single-particle spacing is smaller than the exchange interaction ($-0.8 \leq \alpha \leq 1.2$).

Our results show that the preparation of a specific spin state by appropriate gate voltages and at low enough temperatures in a many electron ring is possible. The special geometry with two independently adjustable gates for each arm of the ring allows to tune the symmetry and relate the behavior of orbital states to properties of the corresponding wavefunctions and their respective fluctuations in the interaction terms. To our knowledge, such a detailed microscopic understanding is unique for our ring, in contrast to other many electron systems.

2.2 Phase-coherent ring as a detector for single-electron effects

L. Meier, A. Fuhrer, T. Ihn, and K. Ensslin, in collaboration with W. Wegscheider (Uni. Regensburg), M. Bichler (Walter-Schottky Institute of the TU München)

Coupled mesoscopic systems are on top of the agenda for experimentalists trying to achieve charge read-out, controlled interference, and entanglement of electrons in magnetotransport experiments. We report an experiment in which two quantum structures, an AB ring and a Coulomb-blockaded quantum dot, interact electrostatically. The goal of the experiment is to detect the interaction between the two subsystems and to unravel its consequences. We show that single-electron charging in the quantum dot can be detected through a reduced AB oscillation amplitude in the transconductance of the ring. We find that our experimental observations are explained by a single-electron screening effect.

The coupled ring–dot structure was realized on a Ga[Al]As heterostructure with a high-quality two-dimensional electron gas (2DEG) 34 nm below the surface. Ring and dots shown in Fig. 2.2(a) were defined by AFM lithography. The two-dimensional electron gas is depleted below the oxide lines. Thereby the central AB ring with a diameter of $1 \mu\text{m}$ is defined, flanked by quantum dots on both sides. Only one dot is used for the experiments described here. The regions of 2DEG adjacent to the quantum dots are split by an additional oxide line leaving point-contact-like openings. Here, one of these regions is used as the 'plunger gate' indicated in the figure. The entire structure was covered by a top gate giving additional tunability. Experiments were carried out in a dilution refrigerator with a base temperature of 40 mK.

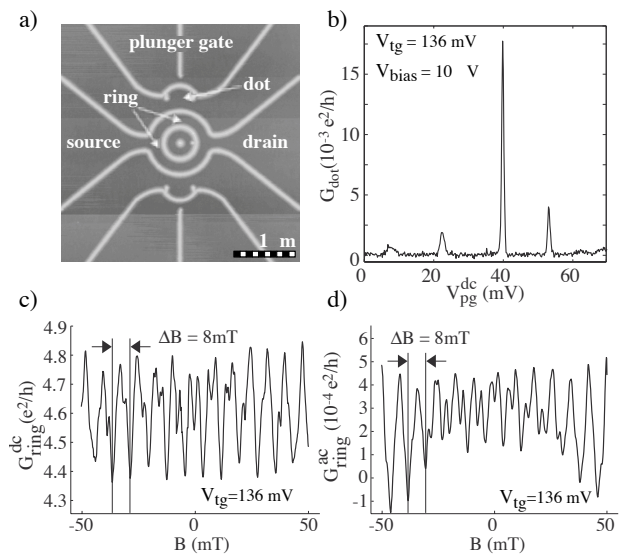


Figure 2.2: (a) Scanning force microscope image of the quantum ring coupled to a quantum dot. The structure was written by AFM lithography. (b) Coulomb-blockade oscillations in the conduction through the quantum dot as a function of the plunger-gate voltage. (c) Aharonov–Bohm oscillations in the dc conductance of the ring. The AB period as expected from the ring area is marked by the horizontal arrows. (d) Aharonov–Bohm oscillations in the transconductance of the ring.

The quantum dot can be tuned into the Coulomb-blockade regime. Pronounced Coulomb-blockade oscillations are observed in the dot conductance G_{dot} [Fig. 2.2(b)]. The quantum ring structure has a conductance $G_0^{\text{dc}} = 4.6e^2/h$ that is rather insensitive to small gate-voltage changes. The conductance exhibits pronounced AB oscillations as a function of magnetic field with a fundamental period $\Delta B_{\text{AB}} = 8 \text{ mT}$ [Fig. 2.2 (c)] which corresponds to one flux quantum penetrating the ring area. In order to increase the measurement sensitivity we measure the AB oscillations in the transconductance. This quantity is measured with lock-in techniques by applying a dc bias voltage between source and drain of the ring and modulating the plunger gate. The transconductance i.e. the modulation of $I_{\text{ring}}^{\text{dc}}$ through the ring is then detected at the same frequency. Figure 2.2(d) shows the resulting AB oscillations in the same magnetic field range as the dc-AB effect in Figure 2.2(c). The fundamental period h/e as well as higher harmonics are visible.

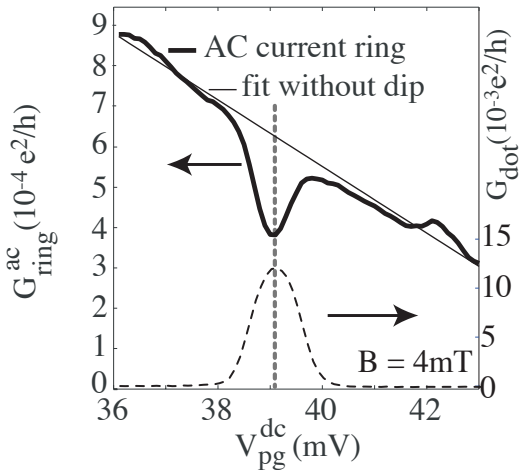


Figure 2.3: Dot conductance peak (dashed line) and ring transconductance (full line). The straight line represents the expected behavior if there was no conductance peak in the dot at this gate voltage.

In contrast to the dc-AB amplitude, the amplitude of the AB oscillations in the transconductance depends strongly on the dc dot conductance measured simultaneously. Figure 2.3 shows the transconductance measured at fixed magnetic field $B = 4 \text{ mT}$, where the effect of the dip is strongest. Our interpretation of the reduced AB amplitude is based on screening of the modulated plunger-gate voltage felt in the ring by single-electron charging in the dot on a conductance peak.

In our model the observed kinks in the dc conductance are similar in origin to the effects observed for the situation, where kinks are observed in the conductance of a quantum point contact neighboring a quantum dot. However our results are different in that we find this effect also in the phase-coherent part of the detector signal namely the AB amplitude. We have demonstrated that the phase-coherent AB oscillations in a quantum ring are sensitive to single-electron charging of an adjacent quantum dot. The ring can be used as a phase-coherent detector of the charge state of the dot.

2.3 Multi-terminal transport through quantum dots

R. Leturcq, D. Graf, T. Ihn, and K. Ensslin, in collaboration with D. D. Driscoll and A. C. Gossard (Materials Department, University of California, Santa Barbara, Ca 93106, USA)

Single mesoscopic systems such as quantum wires, dots and rings are well understood. However, spin-based quantum information processing requires the control of the coupling between components of more complex systems, such as coupled quantum dots. In a standard two-terminal experiment with a single quantum dot in the Coulomb blockade regime, the current in a conductance resonance is determined by the average coupling of the electron wave function in the dot with the corresponding wave functions in both leads. Such an experiment does not allow to determine the individual coupling of the wave function in the dot with each terminal. By connecting three or more terminals to the dot, it is possible to deduce the individual coupling strengths from the dot to the leads.

We have carried out tunneling transport through a three-terminal quantum dot (see Fig. 2.4(a)) in the Coulomb blockade regime. Figure 2.4(b) shows the measurement setup. A dc bias voltage is applied to one terminal of the dot (e.g. $V_{\text{bias}1}$), while the two other terminals are grounded (e.g. $V_{\text{bias}2} = V_{\text{bias}3} = 0$). Current-voltage converters are used to measure the

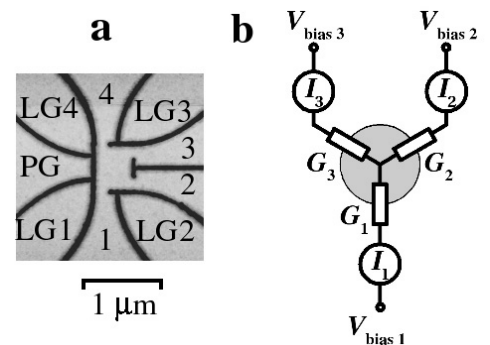


Figure 2.4: (a) Micrograph of the four-terminal quantum dot. The four leads (labelled 1 to 4) to the dot can be tuned through the four lateral gates LG1 to LG4. The plunger gate PG tunes the number of electrons in the dot. (b) Measurement setup using three of the four terminals. The dot (grey circle) is modelled by a classical resistor network.

currents through each terminal. For a bias voltage applied to one terminal, the currents through all three terminals are measured. Then, by applying the bias successively to each of the three terminals, this gives rise to nine different current measurements. In linear response theory, these nine currents can be converted to the nine elements of the conductance matrix of the three-terminal system. This enables us to calculate the tunneling rates from the dot to each lead individually. For weak coupling, the magnitude of the tunneling rates of a given terminal varies independently of the two other tunneling rates, when the number of electrons in the dot is changed. This result can be related to the chaotic shape of the wave function in the dot. The fluctuation of the shape of the wave function in the dot due to quantum interferences is also seen when applying a perpendicular magnetic field. At stronger coupling, it is possible to measure the opening of the contacts due to electrostatic effects. The set-up allows then to tune the tunneling rates from the dot onto the three terminals individually. In addition, the changing shape of the electronic wave function can be monitored on a qualitative level.

2.4 Electronic transport through a quantum dot network

A. Dorn, T. Ihn, and K. Ensslin, in collaboration with W. Wegscheider (Uni. Regensburg), M. Bichler (Walter-Schottky Institute of the TU München)

Electronic transport through granular or disordered materials is mediated by hopping or tunneling processes. Systems under study include arrays of metallic nano-crystals, layers of semiconductor quantum dots, porous silicon, and organic molecular crystals. Experiments are usually carried out on macroscopic samples, so that the microscopic processes are averaged out and can only be inferred by employing a specific model. Here we present measurements on a finite quantum dot network, where the coupling between the dots can be varied continuously. Starting with a high quality GaAs/AlGaAs heterostructure hosting a two-dimensional electron system (2DES) 34 nm below the surface, we used AFM-lithography to define the nano-structure under study. In this way a square lattice of 20×20 insulating islands with a lattice constant of $a=120$ nm was fabricated and enclosed by an insulating cavity with openings in the corners that serve as current and voltage leads (see inset of Fig. 2.5).

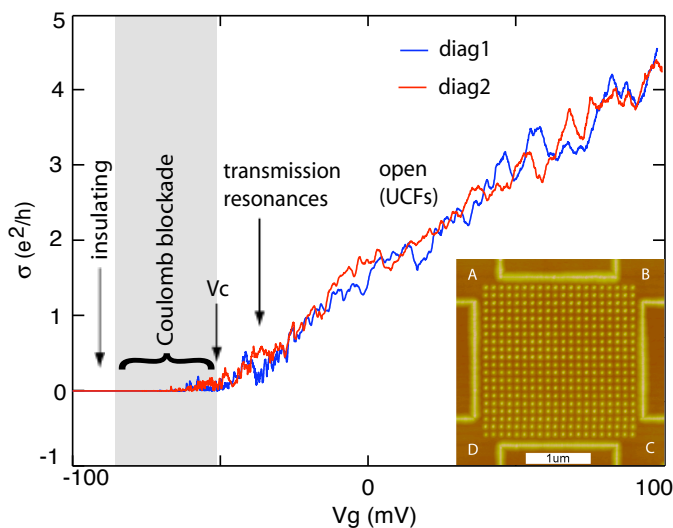


Figure 2.5: Conductance as a function of top gate voltage across diagonal 1 (A-C) and diagonal 2 (B-D). Inset: AFM-micrograph of the lattice and the enclosing cavity. White regions are oxidized and correspond to depletion in the underlying 2DES.

ing discs forming quantum point contacts. Due to small inhomogeneities inherent to the fabrication process and the presence of stray background charges, a percolation transition from the conducting to the insulating phase can be expected. For strong coupling the system behaves like a classical random resistor network with superimposed quantum fluctuations until charge quantization becomes important in the tunneling regime. For weaker coupling, Coulomb blockade dominates resulting in an insulating state for $T \rightarrow 0$ with current onset above a bias voltage threshold and hopping transport at elevated temperatures. Our quantum dot network is at a mesoscopic scale where collaboratively Coulomb blocked areas can be discriminated and related to macroscopic behavior.

Figure 2.5 shows the conductivity measured across diagonal 1 from corner A to C and across diagonal 2 from corner B to D as a function of top gate voltage at $T=90$ mK. As the voltage is lowered, the electron sheet density and the conductivity decrease until the Coulomb blockade regime is reached. This transition takes place at a top gate voltage of about -50.8 mV, marked by V_c in Fig. 1. Towards even lower voltages a series of on average decreasing Coulomb peaks is observed until conduction completely ceases below about -85 mV and the insulating regime is reached. It is worth pointing out that the conductivity across both diagonals is very similar over the entire range of top gate voltages studied aside from reproducible transmission resonances and mesoscopic conductance fluctuations arising from quantum mechanical interference and interaction. This indicates the high symmetry and homogeneity of our sample. We consider the conductance of the entire lattice to be dominated by the constrictions between neighboring insulating

2.5 Magnetic field dependent transmission phase of a double dot system in a quantum ring

M. Sigrist, A. Fuhrer, T. Ihn, and K. Ensslin, in collaboration with W. Wegscheider (Uni. Regensburg), M. Bichler (Walter-Schottky Institute of the TU München) The phase difference of interfering paths in coherent quantum rings can be detected in the conductance by measuring Aharonov-Bohm (AB) oscillations. Keeping the transmission phase of one of the interfering paths constant (reference path), the phase change of the other can be measured. This technique opens the attractive possibility to investigate the transmission phase which contains information about the system complementary to the transmission probability. Multiterminal devices are required for avoiding the restriction found in two-terminal devices, where the phase is locked to 0 or π . Here we investigate the phase evolution of a system of two quantum dots with negligible mutual electrostatic interaction embedded in two arms of a four-terminal AB ring.

The sample is a Ga[Al]As heterostructure containing a two-dimensional electron gas 37 nm below the surface. Oxide lines were written with AFM-lithography as shown in Figure 2.6(a). Lateral gate electrodes marked pg1–4 are used to tune the conductance in each of the four ring quadrants. All measurements were carried out at 100 mK.

A pronounced AB effect is observed in a setup in which the current and voltage contacts are the same two terminals of the ring. The AB signal is maximized with a non-local setup: a bias voltage V_{bias} was applied to terminal A [see Fig. 2.6(b)]. Contacts B and D were grounded via current-voltage converters. The voltage V_{nl} was measured at terminal C leading to a net current flow of zero in this terminal. Figure 2.6(c) shows the AB oscillations in V_{nl} . Their period $\Delta B = 4.8$ mT is consistent with the ring area $A = 0.85 \mu\text{m}^2$.

If any individual segment is tuned close to pinch off, a Coulomb blockaded quantum dot is induced. As an example, Fig. 2.6(d) shows the conductance of segment 1 [A to D in Fig. 2.6(b)] as a function of V_{pg1} with segment 3 completely pinched off and segments 2 and 4 open.

We have succeeded in measuring the AB phase in a four terminal quantum ring with two dots embedded in two different segments. For $50 \text{ mT} < B < 80 \text{ mT}$, the expected phase shifts across Coulomb resonances are typically observed. Phase lapses occur occasionally in finite magnetic field ranges at specific gate voltages. They are accompanied by a vanishing AB amplitude. Even outside the B -ranges where phase lapses occur, the phase evolution can be strongly modified by their presence. The appearance of phase lapses in finite B -intervals impedes the definition of a magnetic field independent transmission phase. A conceivable origin of the phase lapses is the finite width of the ring segments accommodating several modes. In the B -range investigated, the classical cyclotron radius is larger or comparable to the ring radius. A small influence of Lorentz force effects cannot be excluded at the highest fields.

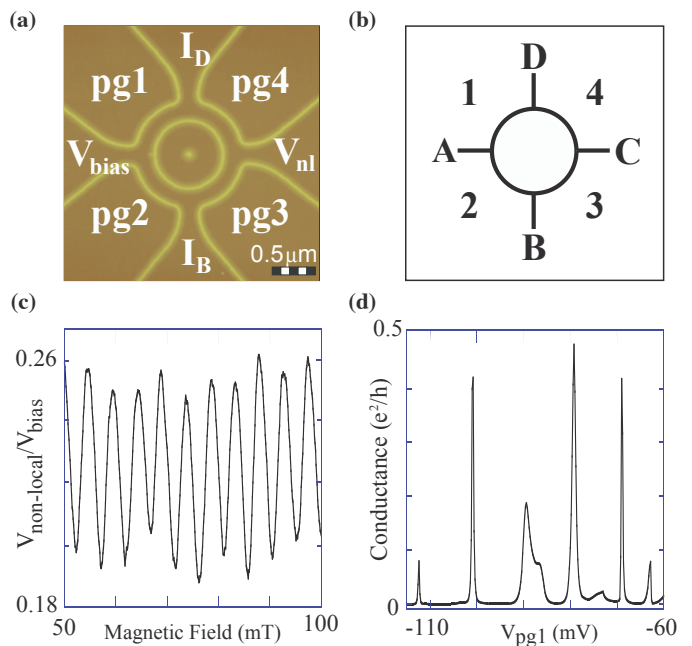


Figure 2.6: (a) AFM micrograph of the ring structure. Oxide lines (bright lines) fabricated by AFM lithography lead to insulating barriers in the two-dimensional electron gas. (b) Schematic arrangement of the ring with its four terminals (c) Nonlocal voltage as a function of B showing AB oscillations. (d) Conductance through a quantum dot induced in segment 1 as a function of plunger gate voltage.

2.6 Electronic properties of p-type GaAs heterostructures

B. Grbic, C. Ellenberger, T. Ihn, and K. Ensslin, in collaboration with D. Reuter and A. D. Wieck (Physics Department, Universität Bochum, D-44780 Bochum) The electronic properties of semiconductor quantum dots are well understood. The overwhelming majority of transport experiments has been done on lithographically patterned n-type quantum dots realized in the GaAs-AlGaAs

material system. Here we set out to explore nanostructures realized on p-type GaAs-AlGaAs heterostructures. Spin effects are generally more prominent in this material system. Most investigations of p-GaAs high-mobility two-dimensional hole gases undertaken so far have focused on structures grown on (311) substrates, where Si acts as an acceptor. In this project we focus on C-doped p-type heterostructures, which also exhibit rather high hole mobilities and are grown on (100) substrates, leading to a more isotropic bandstructure in the plane of the system.

At 100 mK hole temperature the samples have a mobility of $150000 \text{ cm}^2/\text{Vs}$, a carrier density of $3 \times 10^{11} \text{ cm}^{-2}$. The two-dimensional hole gas (2DHG) is located 100 nm below the surface.

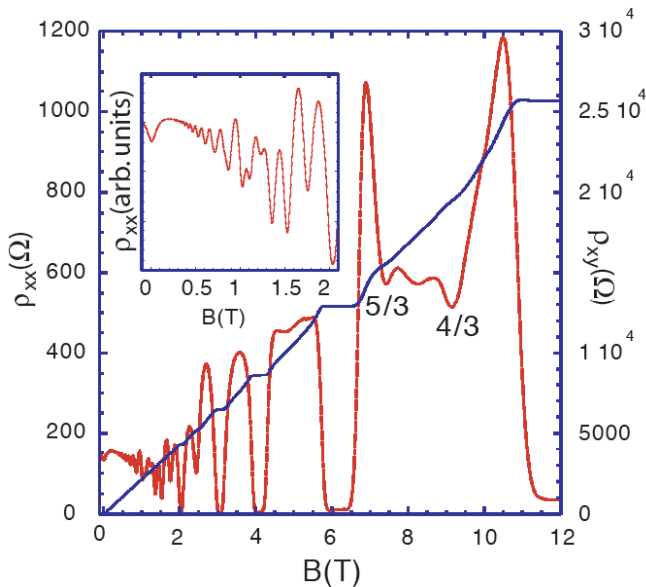


Figure 2.7: Magnetoresistance ρ_{xx} and Hall resistance ρ_{xy} of a C-doped AlGaAs-GaAs heterostructures. The inset shows the magnetoresistance expanded for low magnetic fields.

Figure 2.7 shows the magnetoresistance ρ_{xx} and the Hall resistance ρ_{xy} . Pronounced integer quantum Hall plateaus and minima in the magnetoresistance at fractions of $4/3$ and $5/3$ document the high quality of the sample. The inset shows the regime at low magnetic fields. Two different oscillation periods are clearly visible. The two periods are related to two spin subbands, as has been shown previously for Be-doped (100) structures and for Si-doped (311) samples. In our case the spin polarization at zero magnetic field is 33 %, i.e. there are two times more carriers in the lower spin subband than in the upper spin subband. A detailed analysis revealed the effective masses and mobilities of the two subbands. After deposition of a homogeneous top gate the electron density and mobility could be varied. The mobility keeps increasing even at temperatures below 1K because of reduced phonon scattering. It is apparent, that the mobility drops rather dramatically with decreasing carrier density and that pinch-off is determined by a mobility edge rather than by a vanishing carrier density.

2.7 Microwave spectroscopy of semiconductor nanostructures

B. Simovic, R. Leturcq, C. Ellenberger and K. Ensslin, in collaboration with J. Forrer and A. Schweiger (Institute of Physical Chemistry, ETH Zürich)

Spin resonance and the manipulation of spin states in quantum dots is important in view of spin-based quantum-information processing-schemes. Several groups worldwide are in the process of developing a microwave set-up, which allows to achieve large magnetic field components of the GHz signal at the location of the quantum dot in order to couple to the spins. A larger g-factor obviously helps in this respect, since already moderate magnetic fields will then lead to a Zeeman splitting larger than kT at milli-Kelvin temperatures.

The goal to detect single-spin resonance requires a large magnetic field component of the GHz signal at the location of the quantum dot. We have built a specially designed microwave cavity which contains the dot at the place of maximum field (see Fig. 2.8). This cavity will be connected via a waveguide to the microwave source outside of the cryostats. Spin-echo experiments have revealed a strong enough magnetic field component, that should facilitate the observation of spin resonance in quantum dots.

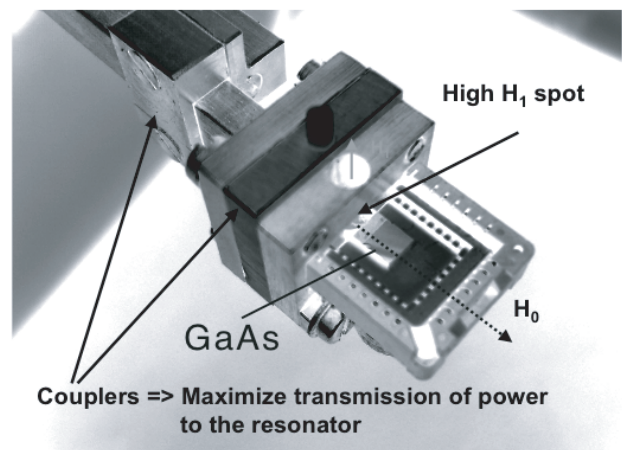


Figure 2.8: Microwave cavity designed for achieving large magnetic field components of the microwave field to excite electron spins in a semiconductor nanostructure.

2.8 Time resolved detection of electrons in a quantum dot

R. Schleser, E. Ruh, T. Ihn and K. Ensslin, in collaboration with D. D. Driscoll and A. C. Gossard (Materials Department, University of California, Santa Barbara, Ca 93106, USA)

The charge state of a quantum dot is usually monitored by conductance resonances. For top-gate defined quantum dots it has been shown that the conductance of a quantum point contact placed close to the quantum dot shows pronounced features which are related to the conductance resonances and can even be monitored when the dot current has become too small to be measured. The inset of Fig. 2.9 shows an AFM-defined quantum dot with a nearby quantum point contact detector.

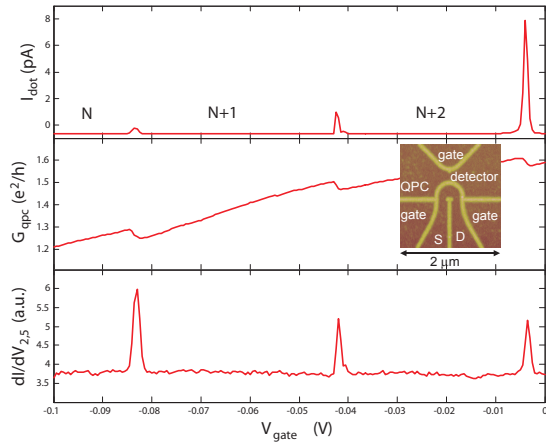


Figure 2.9: top: conductance through a quantum dot fabricated by AFM lithography. middle: signal of the point contact detector located next to the quantum point contact. bottom: derivative of the point contact signal, named transconductance. inset: image of the quantum dot and quantum point contact.

The top trace displays the conductance through the dot, the middle trace the detector signal, and the bottom trace the transconductance, i.e. the differential detector signal upon modulation of a lateral gate. When the coupling of the dot to source and drain is strongly reduced, such that no current flow through the dot can be detected experimentally any longer, the detector still gives reliable information of the charge state of the dot. For very weak coupling we can measure the charging of the dot by individual electrons on the time scale of seconds. This leads to a clearly discernible two-level detector signal which can be analyzed in terms of the average dot occupancy and the dot-lead coupling.

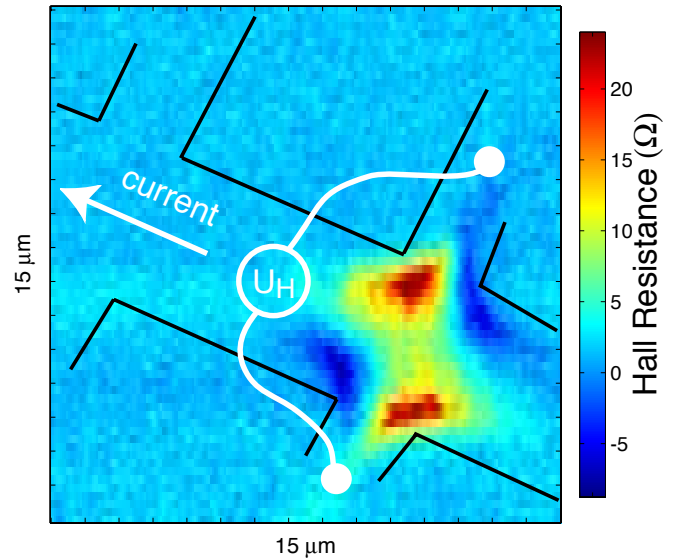
2.9 Local spectroscopy in the quantum Hall regime

A. Pioda, S. Kicin, A. Baumgartner, T. Ihn, and Klaus Ensslin, in collaboration with W. Wegscheider (Uni. Regensburg), M. Bichler (Walter-Schottky Institute of the TU München)

We have built a scanning force microscope which operates reliably down to temperatures of 300 mK and magnetic fields up to 10 T. A $10 \mu\text{m}$ wide Hall bar with a voltage probe separation of $10 \mu\text{m}$ is scanned at low temperatures. An effective potential between the conductive tip and the two-dimensional electron gas in the AlGaAs heterostructure is used to modulate the electron gas density locally. Using Kelvin probe spectroscopy we detect the depletion of the electron gas below the tip for negative tip biases. In a magnetic field the biased tip is used as a scanning gate in order to influence both, the magnetoresistance ρ_{xx} and the Hall resistance ρ_{xy} . The influence of the tip on the sample at a negative tip-sample voltages results in additional scattering of electrons leading to appreciable signals $\Delta\rho_{xx}$ and $\Delta\rho_{xy}$.

In the classical regime of the Hall effect, where Landau quantization is not yet relevant we find a pronounced influence of the Hall resistance on tip position because the tip breaks the symmetry of the Hall cross. Figure 2.10 shows, as an example, the Hall voltage as a function of tip position at zero magnetic field. Depending on the position of the tip, the Hall voltage can be positive or negative and as a result, a butterfly-shaped image emerges. The image can be explained considering the ballistic nature of the electron motion in the Hall cross in terms of transmission probabilities for electrons between pairs of leads forming the cross.

Figure 2.10: Spatial map of the Hall voltage measured on a Hall cross at zero magnetic field in the presence of the conducting tip of a scanning force microscope above the cross. For different tip positions the Hall voltage can be positive or negative leading to the observed butterfly pattern.



In the regime where quantum effects become important we find a $1/B$ periodicity in the scanning gate images which is correlated with the magnetic field positions of integer filling factors simultaneously measured by Shubnikov-de Haas oscillations and the quantum Hall effect. In this regime the tip creates, with local resolution, backscattering between so-called edge channels running at opposite edges of the sample in opposite directions. Such measurements extend previous selective backscattering experiments performed with fixed stripe gates towards a local understanding of the quantum Hall fluid.

2.10 Quantitative topographical analysis of Nuclear Pore Complex function using Scanning Force Microscopy

Rainer D. Jäggi, Alfredo Franco-Obregón, and Klaus Ensslin, in collaboration with U. Kutay (Institute of Biochemistry, ETH Zürich)

Transport receptors mediate the selective translocation of macromolecular cargo across the nuclear envelope which separates the nucleus of the cell from the other components inside the cell. To this end transport receptors must exhibit dual specificity. On the one hand, transport receptors interact with specific amino acid residues that line the transport pathway through the Nuclear Pore Complex (NPC). On the other hand, transport receptors are also responsible for cargo recognition via a peptide sequence that is intrinsic to the cargo molecule. Through these associations transport receptors are then able to chaperone macromolecular cargo through the NPC in a specific and effective manner. The importin β transport complex is the best-characterized nuclear transport pathway of eukaryotes.

We found that the extent of accumulation of bound mutant transport receptors over the luminal domain of the NPC as visualized using Scanning Force Microscopy (SFM) (see Fig. 2.11 A) agreed well with the relative binding affinity of the mutant constructs for the NPC as determined in biochemical measurements. The most dramatic case was that of the 45-462 importin β mutant, which due to the truncation of its amino terminal end is unable to interact with Ran proteins and hence binds irreversibly to the NPC. Furthermore, truncation of the carboxyl terminal of this mutant impedes its interaction with importin α and hence association with NLS-containing cargo.

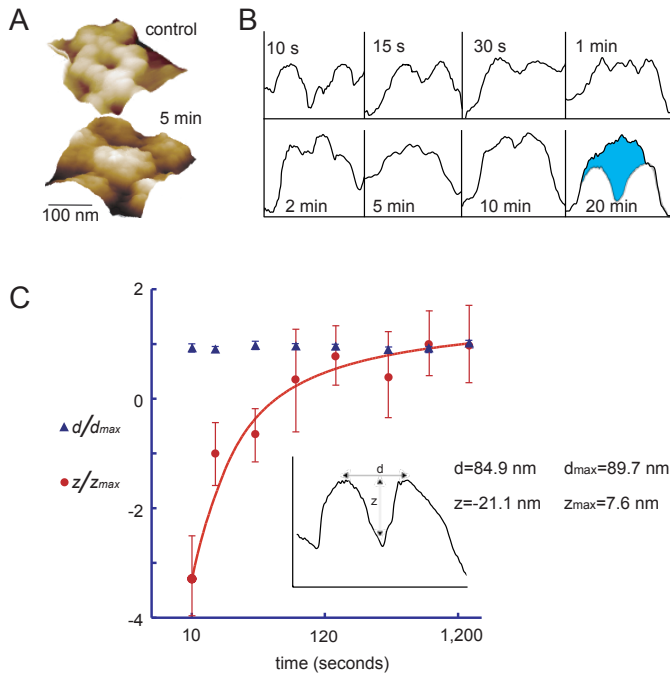


Figure 2.11: Time-dependent accumulation of 45-462 importin β over the surface of the nuclear pore complex (NPC). **A.** Scanning Force Microscopic images of a control NPC (top) and one treated with mutant transport receptor for five minutes (bottom). Scale bar applies to both images. **B.** Line profiles of representative NPCs incubated with mutant protein for the indicated times. For comparison the profile of a NPC after twenty minutes incubation with the 45-462 mutant receptor protein is shown superimposed on the profile of a NPC after twenty minutes incubation with the 45-462 mutant receptor protein. The difference between the two profiles is shown by the shaded area. **C.** Time response curves for normalized diameter (d/d_{max}) and vertical aspect (z/z_{max}) as a function of incubation time with 45-462 mutant protein. The inset depicts the manner in which the measurements of d and z were obtained.

Changes in NPC topology were investigated by taking cross-sectional profiles through single NPCs as previously described. The NPC topology was characterized by measurements of upper rim diameter (d) and central pore depth (z) as indicated in the inset of Fig. 2.11 C. The time dependence of 45-462 binding is shown in Fig. 2.11 B. Since the binding of the 45-462 mutant is an irreversible process the accumulation of bound protein over the central channel region indicates the saturation of available binding sites for importin β . In fact, very brief exposures to the 45-462 mutant protein were necessary in order to be able to clearly resolve the central channel depression of the NPC using SFM before its occupancy with bound protein. Thus, at very short exposure times to the 45-462 mutant protein the NPCs were virtually indistinguishable from those from control samples. After only ten seconds of exposure to 45-462 fragment the filling of the central channel region was apparent. Saturation of 45-462 binding was apparent shortly after only two minutes of incubation.

Chapter 3

Condensed matter at low temperatures

(<http://www.solid.phys.ethz.ch/ott>)

Head

Prof. Dr. H. R. Ott

Academic Staff

Dr. C. Beeli
Dr. M. Chiao
E. Felder
Dr. J.L. Gavilano
Dr. J. Hinderer

Dr. I. Landau
Prof. Dr. R. Monnier
Dr. B. Pedrini
D. Rau
S. Signoretti

Ch. Soltmann
Dr. A. Sologubenko
M. Weller
G. Wigger

Technical Staff

H.R. Aeschbach
P. Wägli

H. Thomas
R. Wessicken

S. Siegrist

Administrative Staff

I. Heer-Mettler

D. Amstad

Academic Guests

Dr. Veljko Zlatic, Zagreb, Croatia
Dr. Ko-Ichi Magishi, Japan

Melting and freezing

Head

Prof. Dr. J. Bilgram

Academic Staff

H. Singer
M. Fell

O. Wittwer

Technical Staff

H.R. Aeschbach

Solid state optics

Head

PD Dr. L. Degiorgi

Academic Staff

G. Caimi
A. Perucchi

Technical Staff

J. Müller

3.1 Physical properties of hexaborides

3.1.1 Magnetotransport in $\text{Eu}_x\text{Ca}_{1-x}\text{B}_6$ ($0 < x < 1$)

G.A. Wigger, R. Monnier, H. R. Ott

We have successfully modelled the magneto-resistance of EuB_6 for all temperatures between 20 and 300K by properly accounting for the scattering of the charge carriers by impurities, phonons and the (disordered) moments of the Eu-ions, as well as for the change in carrier density with temperature and magnetic field. Our attempt to apply our formalism to the evaluation of the anomalous Hall resistivity in this compound led to values several orders of magnitude too low. The same discrepancy has earlier been observed by other authors in Gd and Gd compounds, in which the rare-earth ion's 4f shell is also half-filled, and the reason for it is still unknown. At temperatures below 10K, both the magneto- and the Hall resistance are well reproduced by a two band model, the parameters of which are consistent with the data at high temperatures. Our model also reproduces the relation between the plasma frequency and the magnetization observed in optical reflectivity experiments.

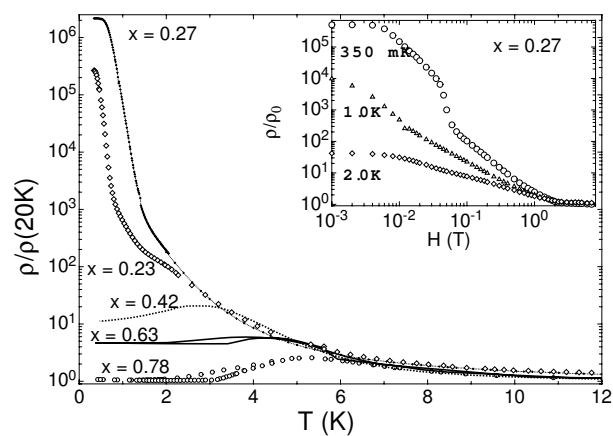


Figure 3.1: $\rho/\rho(20K)$ for $\text{Eu}_x\text{Ca}_{1-x}\text{B}_6$. The inset shows the colossal changes in ρ for $x = 0.27$.

Doping EuB_6 with Ca lowers the temperature of the ferromagnetic phase transition, until it vanishes at a critical concentration $x_p \sim 0.3$. The description of the electrical transport and magnetism may be regarded as site-percolation problems with simple cubic symmetry. Transmission Electron Microscopy reveals a phase separation between Eu- and Ca-rich domains. Near x_p , features of the electrical resistivity can be described as a percolation phenomenon using a random-resistor network, which can also account for the colossal magnetoresistive effects close to $x = x_p$ shown in the inset of the Figure.

3.1.2 Bulk and surface excitations in lanthanum hexaboride

R. Monnier, in collaboration with B. Delley (PSI)

Lanthanum hexaboride is a high yield, low workfunction cathode material used in electron guns and microscopes, and a large body of experimental work has been devoted to the investigation of its bulk and surface properties. Neutron scattering studies have evidenced a rapid flattening of the dispersion curve to an almost constant value of ≈ 3 THz over most of the Brillouin zone (BZ) for both the longitudinal and transverse acoustic modes. We have computed the phonon spectrum of LaB_6 from first principles and reproduce the observed feature. We find that the lowest TA mode in the [110] direction near Γ behaves singularly, due to large and opposite band velocities on the two sheets of the Fermi surface connected by the corresponding wave vector. We also find good agreement between our calculated frequencies for the optical modes of even symmetry with those observed by Raman scattering. Using a supercell geometry consisting of La-terminated, periodically repeated [100] slabs, we have computed the energy of the surface phonons at the Γ point of the surface BZ, with the ions in their fully relaxed positions. We can assign all our values to the peaks observed by high resolution electron energy loss spectroscopy. The electronic structure also very nicely displays the surface band at ≈ 2 eV below the Fermi energy, mapped out many years ago by ultraviolet photoelectron spectroscopy.

3.1.3 Magneto-optical study of Ca -doped EuB_6

A. Perucchi, G. Caimi, L. Degiorgi, and H.R. Ott

Remarkable variations of electronic transport properties, distinctly depending on the bulk magnetization, have been observed for materials, such as rare-earth hexaborides and manganites. Recently, dc magneto-transport and magnetization experiments on a series of $Eu_{1-x}Ca_xB_6$ compounds provided results that again reflect the intimate relation between the electronic conductivity and the magnetization. In particular, for the material with $x=0.4$, an exponential decrease of the resistivity ρ_{dc} as a function of magnetization at constant temperature close to and below the Curie temperature $T_C = 4.5 K$ was reported. These observations are unusual for a bulk magnetic material. Based on these results it was suggested that some kind of magnetization-dependent barriers or intrinsic spin-filter effects dominate the electronic transport in the magnetically ordered phase of this material.

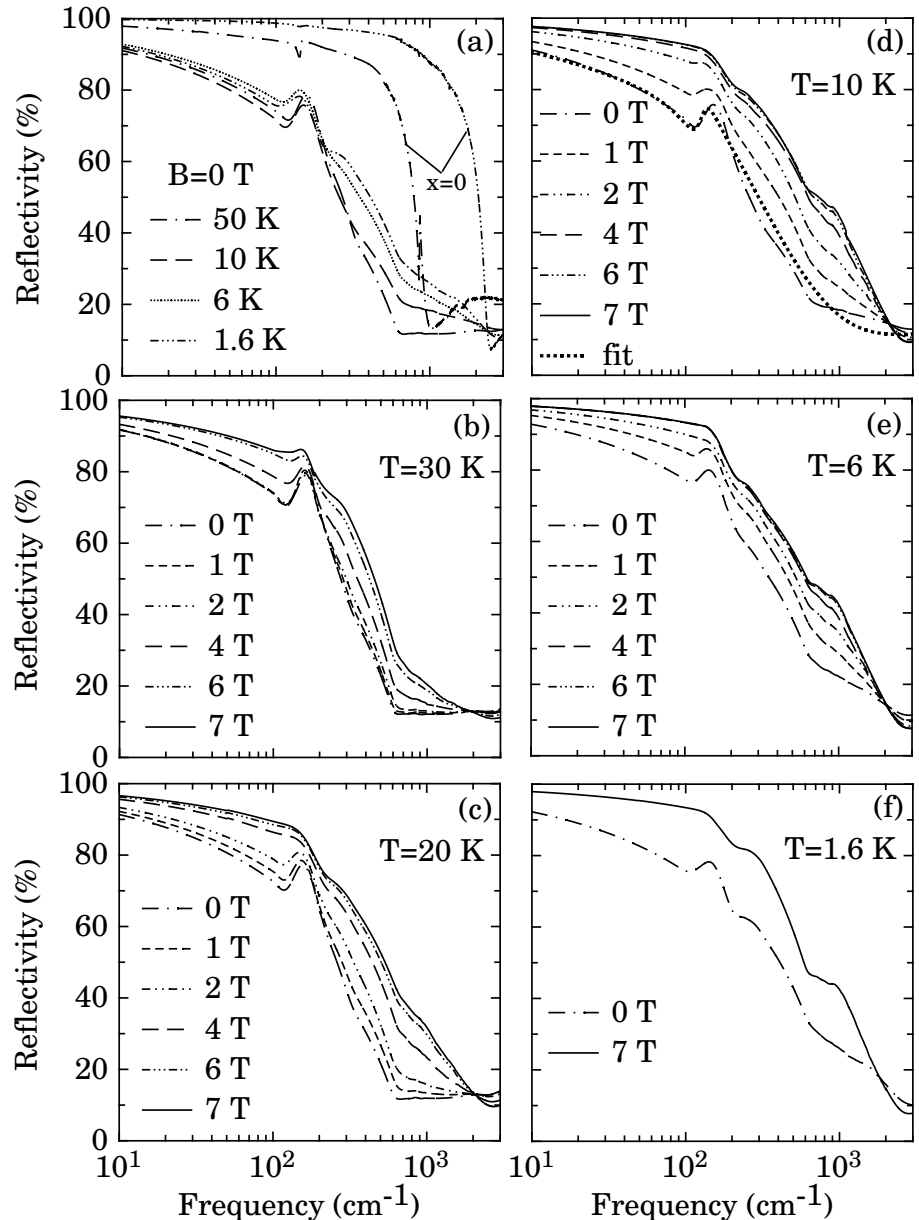


Figure 3.2: (a) Optical reflectivity $R(\omega)$ of $Eu_{0.6}Ca_{0.4}B_6$ in zero field at temperatures between 50 and 1.6 K. Panel (a) also shows $R(\omega)$ for EuB_6 in zero field for $x=0$ at 50 and 1.6 K (the same notation as for $x=0.4$ applies), revealing the much sharper $R(\omega)$ plasma edge. (b)-(f) Magnetic field dependence of $R(\omega)$ at selected temperatures. In panel (d) the Lorentz-Drude phenomenological fit at 10 K and 0 T is also reproduced in order to demonstrate the fit quality.

It was therefore of interest to further characterize its charge transport by investigating the electrodynamic response. Since $\rho_{dc} \sim \Gamma/\omega_p^2$, where Γ and ω_p are the scattering rate and the plasma frequency of the itinerant charge carriers, respectively, it is instructive to single out the relevance of those quantities in relation with the dc properties. We have

measured the optical reflectivity $R(\omega)$ of $\text{Eu}_{0.6}\text{Ca}_{0.4}\text{B}_6$ as a function of temperature between 1.5 and 300 K and in external magnetic fields up to 7 T (Fig. 3.2). $R(\omega)$ increases with decreasing temperature and increasing field but the plasma edge feature does not exhibit the same remarkably sharp onset and steep slope that is observed in the binary compound EuB_6 . The analysis of the magnetic field dependence of the low-temperature optical conductivity spectrum confirms the previously observed exponential decrease of the electrical resistivity upon increasing, field-induced bulk magnetization at constant temperature (Fig. 3.3c). In addition, however, our optical results allow for an analysis of the individual magnetization dependences of the two quantities that determine the dc transport, i.e., the plasma frequency (Fig. 3.3a) and the scattering rate (Fig. 3.3b). The exponential variations that link the magnetization to the Drude spectral weight, which is proportional to the ratio n/m of the charge carrier concentration (n) and the effective mass (m), and to the scattering rate, are rather intriguing. It remains to be seen, how these observations can be explained on a microscopic level.

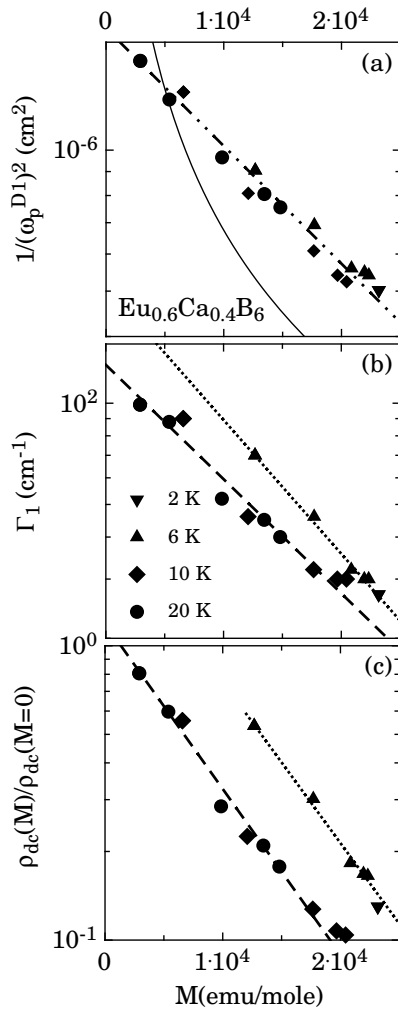


Figure 3.3: (a) Inverse squared plasma frequency $1/(\omega_p^{D1})^2$ of the Drude term as a function of the magnetization M . The dash-dot-dot line represents $(\omega_p^{D1}(M))^{-2} = (\omega_{p0})^{-2}e^{-\beta_\omega M}$ with the parameters $\omega_{p0}=742 \text{ cm}^{-1}$ and $\beta_\omega=5.79 \times 10^{-5} (\text{emu/mole})^{-1}$. Note that a fit with $(\omega_p^{D1}(M))^2 \sim M$ (as for EuB_6), represented by the thin solid line, is obviously inadequate. (b) Scattering rate Γ_1 of the Drude term as a function of M . The dotted and the dashed lines represent $\Gamma_1(M) = \Gamma_0 e^{-\beta_\Gamma M}$ with the parameters $\Gamma_0 = 224 \text{ cm}^{-1}$ and $\beta_\Gamma=9.16 \times 10^{-5} (\text{emu/mole})^{-1}$ for 2 and 6 K , and $\Gamma_0=130 \text{ cm}^{-1}$ and $\beta_\Gamma=7.82 \times 10^{-5} (\text{emu/mole})^{-1}$ for 10 and 20 K , respectively. (c) $\rho_{dc}(M)/\rho_{dc}(M=0)$ versus M , calculated from the Lorentz-Drude fit parameters. The dashed and the dotted lines are calculations based on $\rho_{dc}(M) = \rho_{dc}(M=0)e^{-\beta M}$ with parameters $\rho_{dc}(M=0) = 10 \text{ m}\Omega\text{cm}$ and $\beta=1.30 \times 10^{-4} (\text{emu/mole})^{-1}$ for 10 and 20 K , and $\rho_{dc}(M=0) = 14 \text{ m}\Omega\text{cm}$ and $\beta=1.26 \times 10^{-4} (\text{emu/mole})^{-1}$ for 2 and 6 K , respectively.

3.2 Superconductivity

3.2.1 Ambivalence of the anisotropy of the vortex lattice in an anisotropic type-II superconductor.

I. L. Landau, A. V. Sologubenko and H. R. Ott

In anisotropic type-II superconductors the upper critical field H_{c2} , the magnetic-field penetration depth λ , and the coherence length ξ depend on the direction relative to the crystallographic axes of the material and these dependencies may schematically be represented by ellipsoids. In magnetic fields well below H_{c2} , it is the magnetic interaction between the vortices that provides the main contribution to the free energy of the mixed state. This means that the distances between one chosen vortex line and its six nearest neighbors should all be equal in units of λ , i.e., the nearest neighbors are situated along ellipses that reflect the anisotropy of λ . This circumstance allows a rather direct evaluation of the anisotropy γ using neutron scattering, STM microscopy or Bitter decoration. The actual situation is not, however, that simple and, as we show below, there is some ambiguity in the evaluation of γ from the observed vortex patterns.

Two possible vortex configurations corresponding to the same value of γ are shown in Fig. 3.4(a). The vortex lattices that follow from these two configurations are displayed in Fig. 3.4(b) and (c). While the vortex lattice 1 is indeed strongly anisotropic and its geometrical appearance is as it might be expected intuitively, lattice 2, appears as much less anisotropic. In real space the nearest neighbors of the vortex line a are the vortices b and c . These vortices form a pattern with a close to triangular symmetry, which is emphasized by the dashed-line ellipse in the bottom panel of Fig. 3.4. Thus, although both vortex lattices shown in Fig. 3.4 correspond to the same anisotropy of λ , the anisotropies of the corresponding vortex lattices in real space are quite different.

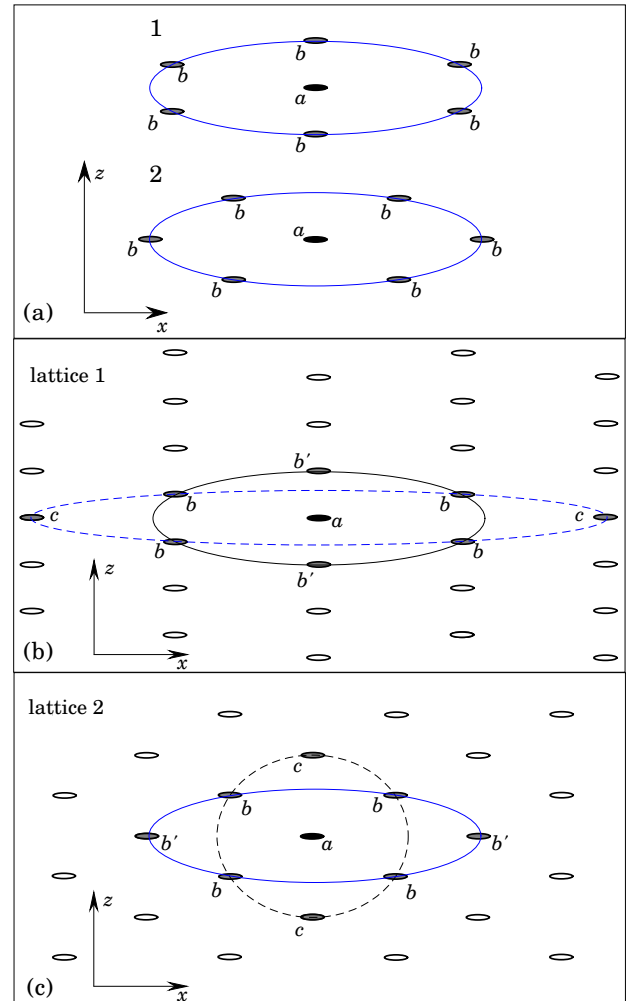


Figure 3.4: (a) Two possible configurations of vortices for $\gamma = 3.5$. The small ellipses represent single vortices, their shape indicates the anisotropy of ξ . (b-c) Two possible vortex lattices. Although both these lattices are drawn for an anisotropy $\gamma = 3.5$ (solid-line ellipses), they are equally consistent with anisotropies that differ from γ by a factor of 3, as is emphasized by the dashed-line ellipses.

3.2.2 Unusual magnetic field-induced phase transition in superconducting NbSe₂

A.V. Sologubenko, I. L. Landau, H.R. Ott

The layered hexagonal compound NbSe₂ is considered to be a conventional superconductor with a relatively low critical temperature $T_c = 7.2$ K. The material has been of recent interest as a possible multigap superconductor, and in view of the competition between the charge-density-wave formation at 34 K and superconductivity.

The basal plane thermal conductivity κ of single-crystalline NbSe₂ has been measured as a function of magnetic field H oriented both along and perpendicular to the c -axis and at several temperatures below T_c . Representative $\kappa(H)$

curves, measured at a $T = 0.85$ K are shown in In Fig. 3.5. Similar results were obtained at other temperatures between 0.38 K and T_c .

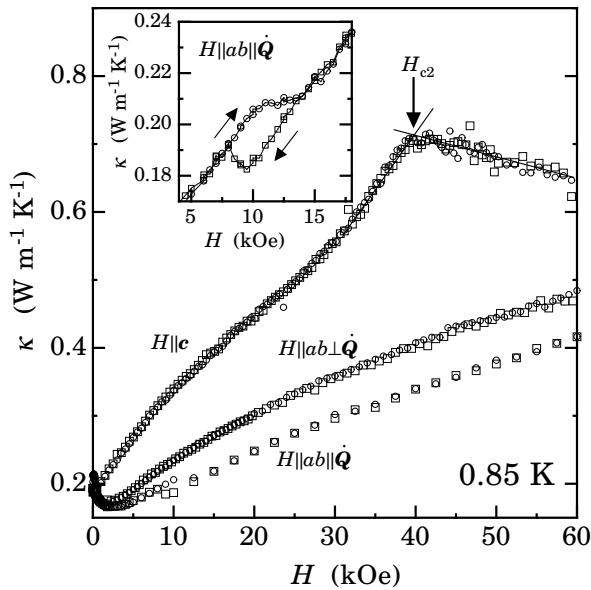


Figure 3.5: The thermal conductivity of single crystalline NbSe₂ in the basal plane, as a function of differently oriented magnetic fields at $T = 0.85$ K. The open circles and squares correspond to increasing and decreasing fields, respectively. The inset emphasizes the discovered hysteretic feature of the thermal conductivity.

The measured $\kappa(H)$ curves are typical for type-II superconductors and can be explained in terms of the model where the quasiparticles associated with the vortices induced in a superconductor by a magnetic field, enhance the phonon scattering, thus reducing the phonon thermal conductivity κ_{ph} but at the same time, enhance the quasiparticle thermal conductivity κ_e . On top of this conventional behaviour, when applying the magnetic field in the basal plane parallel to the heat flux, we observed an unexpected hysteresis of $\kappa(H)$ (see the inset of Fig. 3.5). Although such a behaviour is usually associated with a first order phase transition, several anomalous features make it very difficult to attribute this transition to any vortex-matter transformations that are known for type-II superconductors. First, the transition is absent in $\kappa(H)$ curves when H is oriented perpendicular to the heat flux direction. Second, the critical fields of this transition demonstrate a counterintuitive increase with increasing temperature. Third, the difference between the values of the thermal conductivity in the high-field region and the low-field region is too large to be associated with a difference in the magnetic induction. Fourth, the ratio of the contributions of the high-field and the low-field phases demonstrate a remarkable stability in the hysteresis region.

3.2.3 New interpretation of the equilibrium magnetization of a $\text{Tl}_2\text{Ba}_2\text{CaCu}_2\text{O}_{8+x}$ single crystal.

I. L. Landau and H. R. Ott

The magnetization of a type-II superconductor in the mixed state provides important information about different physical properties of the sample under investigation. The irreversible magnetization is a measure of the pinning strength, while by analyses of the reversible magnetization, different equilibrium parameters of the superconducting material, such as critical magnetic fields and characteristic lengths may be evaluated. This is why magnetization measurements are one of the most widely used tools for studying conventional and unconventional superconductors. In order to obtain the relevant information from raw magnetization data, different models of the mixed state are used. Recently we have developed a simple scaling approach for the analysis of the magnetization data. The main advantage of our scaling procedure is that it is based on very few rather general assumptions, which makes it applicable for a wide range of experimental situations.

Fig. 3.6 shows the results of our analysis for a $\text{Tl}_2\text{Ba}_2\text{CaCu}_2\text{O}_{8+x}$ single crystal investigated in Ref. 1. The comparison between the result of our analysis with that of a previous interpretation using another widely used model, demonstrates that the unphysical result in the inset of Fig. 3.6 may be avoided with our procedure.

[1] H.-J. Kim, P. Chowdhury, I.-S. Jo, and S.-I. Lee, Phys. Rev. B **66**, 134508 (2002).

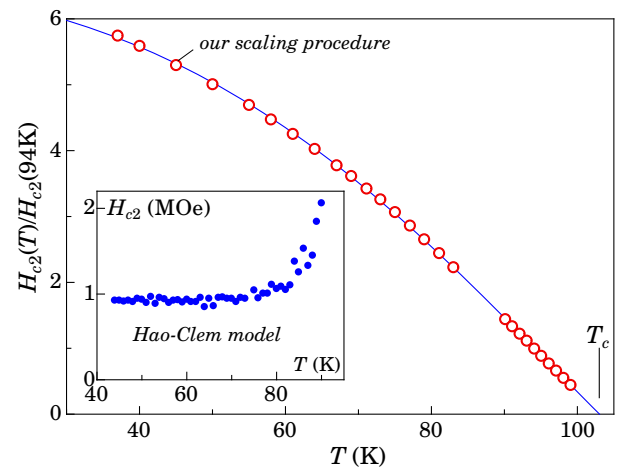


Figure 3.6: The normalized temperature dependence of H_{c2} . The inset shows the $H_{c2}(T)$ curve as it is given in Ref. 1.

3.3 Structural and physical properties of quasicrystals

3.3.1 Structure analysis of decagonal Al-Co-Ni quasicrystals

C. Soltmann, C. Beeli in collaboration with R. Lück, Max-Planck-Institut für Metallforschung, Stuttgart, Germany

The aim of the present in-situ high-temperature powder diffraction investigation was to monitor the two high-temperature phase transitions in Ni-rich Al-Co-Ni quasicrystals in order to better characterise the structural processes at higher temperatures and across the two phase transitions present at high temperatures. We showed that the transition temperatures of the phase transitions of the type I superstructure to the S1 superstructure and of the S1 superstructure to the basic decagonal phase can be determined very reliably by the applied high-temperature in-situ X-ray powder diffraction setup, despite the fact that the relative changes in the determined and inferred quantities are very small.

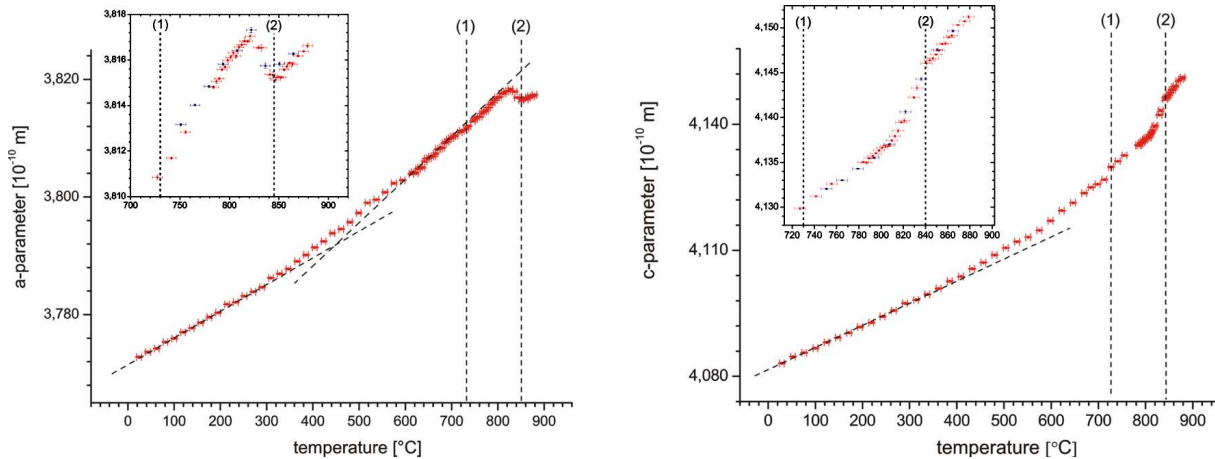


Figure 3.7: Temperature dependence of the cell parameters of $\text{Al}_{71}\text{Co}_{11.5}\text{Ni}_{17.5}$ at intermediate temperatures and across the phase transitions of type I to S1 (1) and the S1 to basic decagonal (2) quasicrystal phases. The insets show the thermal evolution of the cell parameters across the phase transitions of the S1 to the basic decagonal phase at increasing (red data points) and at decreasing temperatures (blue data points).

The analysis of the experimental data was based on the cell parameters of the respective quasicrystals and on the inferred quantity c/a . The results obtained for four different chemical compositions provided meaningful information on the thermal expansion behaviour in general and on the high-temperature phase transitions in particular.

The thermal expansion behaviour at temperatures below the phase transition temperature of the type I superstructure to the S1 superstructure proved to be clearly more complicated than expected (Fig. 3.7). The numerical values for the onset temperatures of structural changes in connection with both high-temperature phase transitions and for the corresponding transition temperatures, as obtained in this study, are a very good match for the corresponding values obtained by dilatometric measurements. The results inferred from the high-temperature data showed that the principal evolution of the cell parameters as well as of the c/a ratio is similar across the two high-temperature phase transitions, namely the opposite thermal expansion behaviour of the cell parameters across the phase transitions and the corresponding step increase in the c/a ratio. The measurements confirmed that the phase transition of type I to the S1 superstructure is a second-order transition. No indication of coexisting decagonal phases at high temperatures were found. Across this phase transition, the cell parameters change contrarily whereas the cell volume remains almost unaffected. The structural processes across the phase transition can be related to a deformation of three-dimensionally linked coordination polyhedra.

Both high-temperature phase transitions were found to be reversible. However, relaxation processes were observed which affect mainly the course of the a-parameter (quasilattice parameter) across the phase transition from the S1 superstructure to the type I superstructure. These observations indicate that the quasiperiodic layers are significantly more influenced by a delayed relaxation owing to finite cooling rates. Delayed relaxation within quasiperiodic layers can be associated with order/disorder processes across the phase transition. These processes are related to a change in the type of tiling, i.e., to phason flips.

3.3.2 Comparative NMR studies of decagonal and icosahedral $\text{Al}_{69.8}\text{Pd}_{12.1}\text{Mn}_{18.1}$

D. Rau, J.L. Gavilano, J. Hinderer, C. Beeli, M. Weller and H. R. Ott

We have extended our previous NMR studies [1] of decagonal $\text{Al}_{69.8}\text{Pd}_{12.1}\text{Mn}_{18.1}$ to explore the very-low temperature region and we have performed a comparative study of the NMR response of icosahedral (i-AIPdMn) and decagonal (d-AIPdMn) phases of the same material. Our experimental data reveal spin-glass type freezing transitions at $T_f = 19$ and 12 K for i-AIPdMn and d-AIPdMn, respectively.

Above 120 K, in the paramagnetic state of our material, we find that all the Mn ions in the icosahedral phase carry a magnetic moment, while in the decagonal phase this number is of the order of 50%. These concentrations n_{mag} of magnetic Mn ions, are surprisingly large for quasicrystals. Below 110K the concentration n_{mag} decreases by more than 20% for d-AIPdMn [2], but no reduction is observed for i-AIPdMn.

The low-temperature phases of both materials are very unusual. For example, at temperatures below the spin glass transition T_f the NMR line-widths of icosahedral and decagonal $\text{Al}_{69.8}\text{Pd}_{12.1}\text{Mn}_{18.1}$ decrease with decreasing temperature. In addition, both the NMR spectra and the spin-lattice relaxation rate T_1^{-1} , which for these compounds are very different above T_f , are almost identical at very low temperatures, $T/T_f \leq 0.1$.

Our data suggest that at temperatures below T_f , the spin-glass phases of d-AIPdMn and i-AIPdMn gradually disappear. In both cases this unusual process is completed at $T \approx 2$ K and leaves a paramagnetic phase, with a very small amount of isolated Mn magnetic moments. Our $T_1^{-1}(T)$ data reveal important changes in the dynamics of these moments below 1 K.

[1] J. L. Gavilano, D. Rau, Sh. Mushkolaj, H. R. Ott, J. Dolinšek, and K. Urban, Phys. Rev. B, **65**, 214202 (2002).

[2] D. Rau, J.L. Gavilano, Sh. Mushkolaj, C. Beeli, M. A. Chernikov, H. R. Ott, Phys. Rev. B, **68**, 13204 (2003).

3.4 Physics of low-dimensional systems

3.4.1 Unconventional Charge Ordering in $\text{Na}_{0.70}\text{CoO}_2$ below 300 K

J. L. Gavilano, D. Rau, B. Pedrini, J. Hinderer, H. R. Ott, C. Beeli M. Wörle, S. M. Kazakov and J. Karpinski

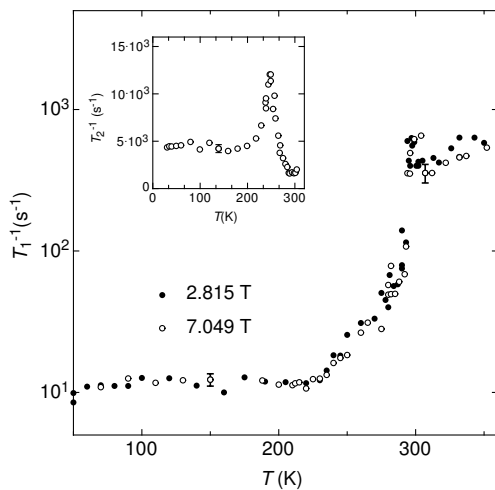


Figure 3.8: Main frame: Spin-lattice relaxation rate as a function of T measured at two different external magnetic fields. Inset: Spin-spin relaxation rate as a function of T , measured in an external magnetic field of 2.815 T.

The unexpected recent discovery [1] of superconductivity in $\text{Na}_{0.3}\text{CoO}_2 \cdot 1.3\text{H}_2\text{O}$ below a critical temperature $T_c \approx 5$ K, has triggered an enhanced interest in layered alkali-metal cobalt oxides. Of special interest is the parent compound, $\text{Na}_{0.70}\text{CoO}_2$, whose physical properties are quite puzzling.

We have performed measurements of the magnetic susceptibility and ^{23}Na -NMR on polycrystalline samples of Na_xCoO_2 . The high quality of our sample has been verified by X -ray diffraction and electron microscopy.

The $\chi(T)$ data suggest that for $T > 75$ K, the Co ions adopt an effective configuration of $\text{Co}^{3.4+}$. The temperature evolution of the ^{23}Na -NMR linewidth of the Na central transition reveals a pronounced peak near 250 and a change of slope at 295 K, but no evidence for magnetic phase transitions is found in $\chi(T)$.

Below 230 K, the spin-lattice relaxation rate T_1^{-1} is approximately T -independent. With increasing temperature we observe, near 230 K, the onset of an increase of the relaxation rate T_1^{-1} . This onset is accompanied by a significant anomaly in of the spin-spin relaxation rate $T_2^{-1}(T)$.

Together, these two relaxation-rate features provide evidence for a crossover phenomenon or a phase transition. With increasing T , dT_1^{-1}/dT increases and an almost discontinuous enhancement of T_1^{-1} , by a factor of 20, occurs at 295 K. Our data suggest a dramatic change in the Co 3d-electron spin dynamics at 295 K. Upon decreasing temperature, this process is completed at 230 K.

From our results [2] we infer that below 295 K the Co 3d-electron system is affected by at least one phase transition. Two scenarios seem possible: (a) a partial charge ordering phenomenon involving Co^{3+} and Co^{4+} upon decreasing temperature, completed only near 230 K; and (b) an unconventional charge density wave within the Co subsystem develops. The system remains metallic at all temperatures.

[1] K. Takada H. Sakurai, E. Takayama-Muromachi, F. Izumi R. A. Dilanian, T. Sasaki, Nature **422**, 53 (2003).

[2] J. L. Gavilano, D. Rau, B. Pedrini, J. Hinderer, H. R. Ott, S. M. Kazakov and J. Karpinski, cond-mat/0308383 (2003).

3.4.2 Low-temperature specific heat of $\text{Na}_2\text{V}_3\text{O}_7$

J. L. Gavilano, E. Felder, D. Rau, H. R. Ott

In collaboration with P. Millet (CEMES, Toulouse), and F. Mila (University of Lausanne)

$\text{Na}_2\text{V}_3\text{O}_7$ is an insulator with very peculiar structural features [1] and unusual low temperature properties [2]. In particular the V ions form an unusual arrangement of spins with $S = 1/2$. From our previous investigation of $\text{Na}_2\text{V}_3\text{O}_7$ using NMR techniques we concluded that $\text{Na}_2\text{V}_3\text{O}_7$ is very close to or at a quantum critical point at $H = 0$ T.

We made measurements of the specific heat $C_p(T)$ of $\text{Na}_2\text{V}_3\text{O}_7$ in various external magnetic fields of 0, 1.5, 3 and 5 T and at temperatures between 0.3 and 40 K. We found that $C_p(T)$ of this material exhibits several unusual features. Between 8 and 20 K, $C_p(T)$ is well represented by $C_p(T) = \gamma T + \beta \cdot T^3$, with $\gamma = 55$ mJ/(mol K²) and $\beta = 0.9$ mJ/(mol K⁴). We associate the cubic term $\beta \cdot T^3$ with the lattice contribution to the specific heat. The linear term γT turns out to be rather large. Interpreting this contribution to be due to $S = 1/2$ spinon excitations in the low-temperature limit, leads to expectations for the magnetic susceptibility which do not agree with the experimental observation and, therefore, does not make sense.

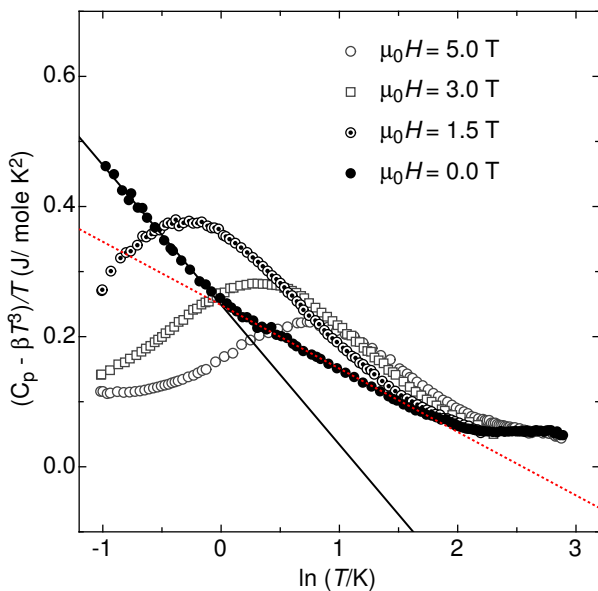


Figure 3.9: $(C_p - \beta \cdot T^3)/T$ as a function of $\ln(T)$ for $\text{Na}_2\text{V}_3\text{O}_7$. The solid and broken lines each represent the sum of a linear- and a logarithmic-in- T contribution to $C_p(T)$.

[1] P. Millet, J.Y. Henry, F. Mila, J. Galy, J. Solid State Chem. **147**, 676 (1999).

[2] J.L. Gavilano, D. Rau, Sh. Mushkolaj, H.R. Ott, P. Millet, F. Mila, Phys. Rev. Lett., **90**, 167202 (2003).

The total excess entropy, per mol of V^{4+} ($S = 1/2$) ions, released up to 20 K, is about one order of magnitude smaller than $R \cdot \ln(2)$, indicating that only a small fraction of the V ions are magnetically active at low temperatures. This result adds support to our previous conjecture [2] that there is a gradual quenching of the V magnetic moments in $\text{Na}_2\text{V}_3\text{O}_7$ at temperatures between 100 and 20 K.

At lower temperatures $C_p(T)$ exhibits broad maxima at $T_0(H)$ which shift to higher temperatures upon increasing applied external field H . The data indicate that for $H = 0$ T, $T_0 = 0$ K. In zero magnetic field $C_p(T)/T$ diverges logarithmically towards $T = 0$ K. These results support the conjecture that $\text{Na}_2\text{V}_3\text{O}_7$ is close to or at a quantum critical point at $T = 0$ K and $H = 0$ T. Although the experimental results for the $C_p(T)$ and NMR are consistent with each other, a realistic theoretical description of the low-temperature physical properties of $\text{Na}_2\text{V}_3\text{O}_7$ is presently not available. This is mainly due to the topology of the arrangement of the V moments and the resulting complexity of the $V - V$ interactions.

3.4.3 NMR and dc-susceptibility studies of NaVGe₂O₆

B. Pedrini, J. L. Gavilano, D. Rau and H. R. Ott

In collaboration with S. M. Kazakov and J. Karpinski

We measured the dc-susceptibility and ²³Na-NMR response of NaVGe₂O₆, a recently synthesized material consisting of isolated chains of, slightly distorted, VO₆ octahedra. Taking into account the structural features of this material and the most likely oxidation states of O²⁻, Na¹⁺ and Ge⁴⁺, NaVGe₂O₆ may be expected to represent a good physical realization of a one-dimensional antiferromagnetic S = 1 spin system, for which a nonmagnetic ground state (the Haldane phase) is expected to develop at low temperatures.

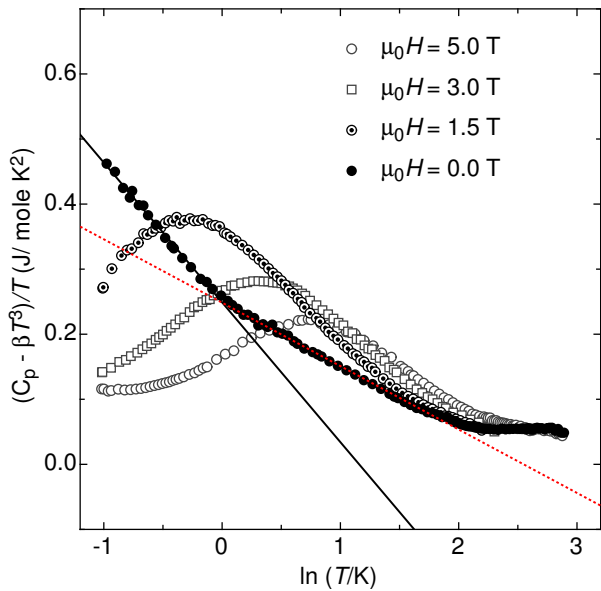


Figure 3.10: ²³Na spin-lattice relaxation rate T_1^{-1} as a function of T^{-1} . The solid line represents $T_1^{-1} = C \exp(-\Delta/k_B T)$. Inset ²³Na-NMR spectra of NaVGe₂O₆, measured at 7.049 T

Above 100 K, the magnetic susceptibility $\chi(T)$ of NaVGe₂O₆ follows a Curie Weiss type of behavior with an effective moment of $2.7 \mu_B$, indicating a trivalent oxidation state (S=1) for the V ions. Detailed comparisons of $\chi(T)$ with the results of computer simulations, however, reveal the presence of non-negligible interchain coupling. In fact a kink in $\chi(T)$ at 18 K indicates a magnetic phase transition.

At temperatures above 18 K, the temperature dependence of the ²³Na-NMR response of NaVGe₂O₆ follows $\chi(T)$. The observed hyperfine coupling between the V moments and the Na nuclei contains, in addition to the usual direct dipolar coupling, an isotropic term, whose origin is presently not understood. The phase transition at $T_N = 18$ K is reflected by a drastic change of the lineshape of ²³Na NMR spectra and an anomaly in the temperature evolution of the spin-lattice relaxation rate $T_1^{-1}(T)$. At very low temperatures $T \ll T_N$, $T_1^{-1}(T)$ decreases rapidly with decreasing temperature, indicating the formation of a gap $\Delta/k_B = 12.5$ K in the magnon excitation spectrum.

We conclude that in NaVGe₂O₆, the expected Haldane phase does not develop because the system orders antiferromagnetically below 18 K. The ratio between the intrachain and interchain coupling, estimated from the $\chi(T)$ data by a mean-field analysis, is large enough to explain this observation [1].

[1] A.Koga and N. Kawakami, Phys. Rev. B **61**, 6133 (2000).

3.5 Instrumentation: NMR under pressure

J. Hinderer, M. Weller, J. L. Gavilano, D. Rau, M. Chiao, H. R. Ott.

In collaboration with I. Sheikin, GHMFL, Grenoble, France

We are building an NMR station combined with a magnet and a cryostat, which can accommodate a pressure cell. The aim is to do measurements in a 5mm inner bore at hydrostatic pressures of up to 20 kbar in magnetic fields of up to 8 Tesla at temperatures down to 500 mK.

We have designed and assembled a continuous flow ³He cryostat with an experimental space of 48mm diameter that can accommodate pressure cells as heavy as 1kg or more. It provides two coaxial signal lines as well as two rotatable axes in order to tune the NMR tank circuits at low temperature close to the sample (high signal to noise ratio). The modest minimum temperature is a tradeoff to the high cooling power which is necessary for NMR experiments (RF pulses). The cryostat is placed inside an 8 Tesla superconducting magnet. A BeCu piston cylinder pressure cell has been built and will be autofrettaged in order to go to pressures up to 20 kbar.

We have assembled and tested a new NMR station that can be operated from 2 up to 400 MHz. It is based on a home made spectrometer. The pulse control and the signal recovery is done by PC based hardware.

3.6 Electron holography

3.6.1 Measurement of the mean inner potential of various metals by electron holography

S. Signoretti, C. Beeli; in collaboration with B. Doudin, Department of Physics and Astronomy, University of Nebraska Lincoln, USA

In various microscopy techniques it is of great importance to know the volume average of the electrostatic potential of a solid, generally known as the mean inner potential. This potential V_0 is negative and lies typically between 5 and 30 V, depending on the composition and the structure of the solid. The knowledge of the mean inner potential is important in practice in low energy electron diffraction (LEED), reflected high-energy low energy electron diffraction (RHEED), Fresnel imaging of interfaces (i.e. defocused electron micrographs) and in electron holography.

We have measured the mean inner potential of single-component nanowires of cylindrical shape (with circular cross section), made of Ag, Co, Cu and Ni. Our measurements resulted in the following values: $V_{Ag}=26.9$ V, $V_{Co}=25.8$ V, $V_{Cu}=20.1$ V and $V_{Ni}=21.4$ V, respectively. The typical measurement error amounted to 1.0 to 1.5 V. The comparison with calculated values of the mean inner potential revealed generally a good agreement, with the exception of Ni. In the case of Nickel the calculated values lie around 25 V. This discrepancy may be explained by a low density of the Ni nanowires as a consequence of the nanocrystallinity, as well as by an oblate shape of the nanowires, resulting in systematically wrong estimates of the sample thickness. The investigation thus showed that the calculated mean inner potentials can be employed with reasonable confidence.

3.7 Noble gases as model systems to study solidification behaviour of melts

H.M. Singer, O. Wittwer, and J. Bilgram

Complex structures developed during a solidification process can influence properties of the solidified material. Predictive models for heat and fluid flow are successfully being used in the design of components and casting processes, but the ability of those models to quantitatively predict casting defects such as porosity and hot tearing is limited. The present lack of knowledge of the morphological development during solidification is prohibitive for the development

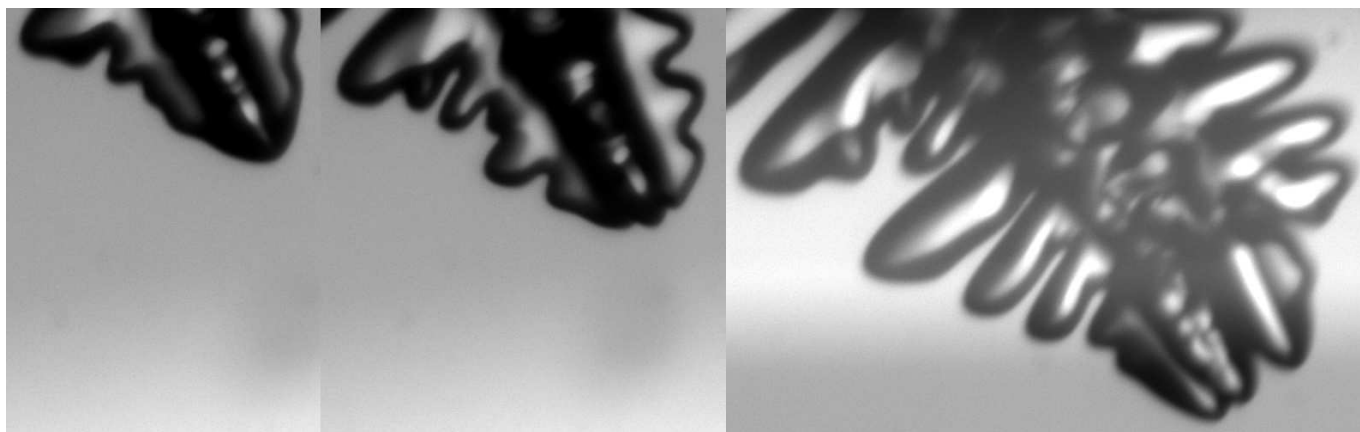


Figure 3.11: Morphological transition of a xenon crystal from a dendrite to a triplon

of the sophisticated casting models that are needed e.g. in the aluminium foundry industry. In recent years the complex patterns produced by growing dendrites have been a source of immense theoretical interest. For an application of theoretical results typical length scales and rate constants have to be implemented. These data have to be measured in experiments. Theoretical and experimental studies have shown that besides dendrites other morphologies are formed during solidification. Transitions between such morphologies are supposed to have a strong influence on the microstructures in the final product and thus on its mechanical and corrosion properties. Morphology changes seem to lead to an explanation of grain refinement in metals, a feature that remained unexplained since long time.

We have developed experimental techniques to produce complex shapes in 3D solidification experiments. We use xenon as a transparent model substance for metals and have shown for the first time, that various morphologies can be produced (Fig.1). We study the conditions for the initiation of various morphologies and have developed a morphology diagram of 3D structures. Some of the 3D morphologies have counterparts in 2D.

In all cases the topology of a 3D structure is different from the one of a 2D structure. It is important to determine the shape parameters of 3D objects, therefore we developed a technique to reconstruct a 3D shape of an experimentally grown transparent crystals. For the first time it is possible to reconstruct the shape of transparent objects where no close up inspection is possible. Now we compare quantitatively objects deduced from theoretical studies and our phase field simulations with the ones grown in experiments. Thus it is possible to verify assumptions used in theoretical studies and to test scaling laws. Up to now no 3D data from experiments were available. We study multi-morphologies like doublons and triplons to find out the stabilization process of these structures, which is of great theoretical interest.



Figure 3.12: Original image of a xenon dendrite and its 3D reconstruction

Two new features have been introduced into the study of the solidification process by model experiments: 1.) the study of various morphologies and morphological transitions, and 2.) the reconstruction of transparent 3D objects. We have the unique possibility to combine theoretical studies with experiments.

3.8 Application oriented thin film research

3.8.1 Epitaxial IV-VI narrow gap semiconductor layers

K. Alchalabi, K. Kellermann, D. Zimin, M. Arnold, A.N. Tiwari and H. Zogg; www.tfp.ethz.ch

Narrow gap lead chalcogenide (IV-VI) layers like PbX , $\text{Pb}_{1-x}\text{Sn}_x\text{X}$ and $\text{Pb}_{1-x}\text{Eu}_x\text{X}$ ($\text{X} = \text{Te}, \text{Se}$) are investigated for applications and basic research. The layers are grown by solid source molecular beam epitaxy (MBE) onto Si-substrates, employing a CaF_2 buffer layer. The density of threading dislocations in these lattice- and thermal expansion mismatched layers ranges from 10^6 cm^{-2} to 10^8 cm^{-2} . Despite of these rather high densities, devices with reasonable quality are fabricated in the layers:

- Heteroepitaxial monolithic two-dimensional Infrared Focal Plane Arrays (2d IR-FPA) have been realized on active Si-substrates; the Si-substrate chip already contains the read-out and addressing electronics. Array size is 96×128 pixels on a $75 \mu\text{m}$ pitch. The IR-detectors sensitive in the $3\text{-}5 \mu\text{m}$ wavelength range are fabricated in the epitaxially overgrown PbTe layer. Schottky-barrier as well as p-n junction sensor arrays have been fabricated. The junction noise currents are determined by the dislocation densities ($\sim 10^7 \text{ cm}^{-2}$) in the non-lattice matched layers [for a review, see IEEE Trans. ED50, 209(2003)].

- Optically pumped mid-IR lasers on Si-substrates have been realized. They consist of PbSe QW (quantum wells) embedded in $\text{Pb}_{1-x}\text{Eu}_x\text{Se}$ barrier layers. The EuSe top cladding layer is transparent to the incoming pump beam. The mirror facets are either cleaved (for (100) oriented IV-VI layers, (100) is their natural cleavage plane) or etched (for (111) orientation), fig. 3.13, left. As pump source, low cost high power GaAs based laser diodes emitting at 900 nm are employed. The IV-VI devices emit in the 4-6 μm range, the exact wavelength depends on the width of the QW and temperature. At the maximum peak power of the pump beam, the peak output power is as high as 240 mW per facet and the quantum efficiency up to 20 % (one facet). The highest operation temperature reached so far is 250 K. The threshold is limited by Shockley-Read (sr) recombination (fig. 3.13, right), leading to carrier lifetimes as short as 0.1 ns. This is due to the high dislocation density of $>10^8 \text{ cm}^{-2}$. A reduction to 10^7 cm^{-2} is feasible, which then would lead to a factor 10 improvement of the sr lifetimes and correspondingly higher operation temperature [J. Appl. Phys. 94, 7053(2003)].

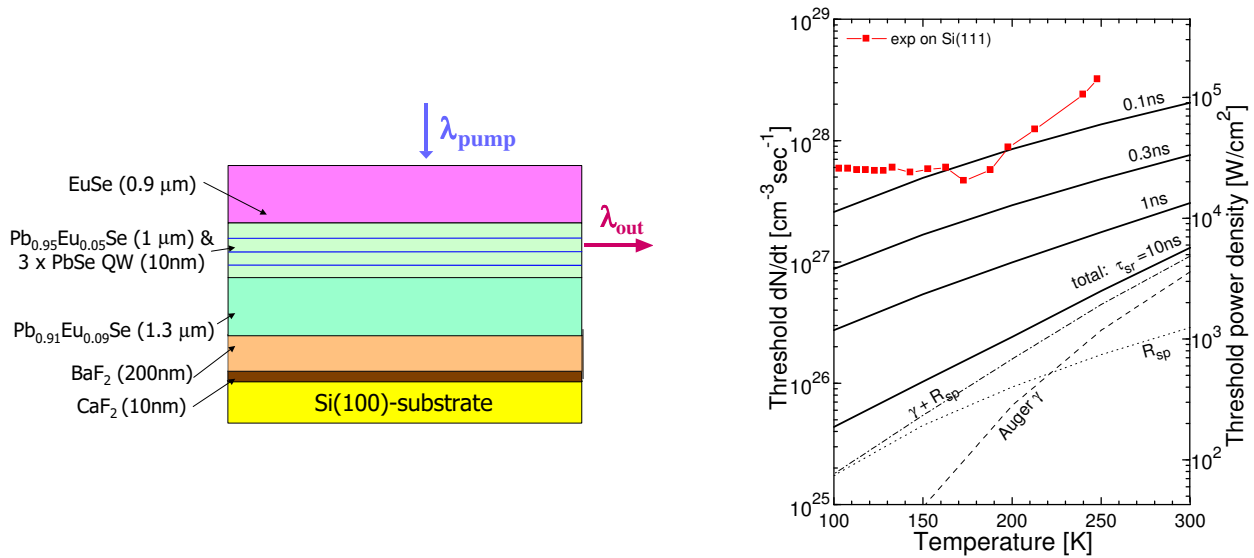


Figure 3.13: *Left:* Schematic structure of an optically pumped IV-VI QW laser grown on a Si-substrate. *Right:* Calculated and measured threshold power densities (for 900 nm pump light) for IV-VI lasers on Si-substrates. Calculated losses are for Auger recombination (γ), spontaneous recombination R_{sp} and sr-recombination at defects with lifetimes τ_{sr} .

3.8.2 Thin film solar cells based on $\text{Cu}(\text{In,Ga})\text{Se}_2$ and CdTe compound semiconductors

D. Abou-Ras, D.L. Bätzner, D. Brémaud, A.F. da Cunha, F.-J. Haug, M. Kaelin, G. Khrypunov, F. Kurdesau, A. Romeo, D. Rudmann, H. Zogg, and A.N. Tiwari; www.tfp.ethz.ch

3.8.2.1 CIGS thin film solar cells

High efficiency $\text{Cu}(\text{In,Ga})\text{Se}_2$ (CIGS)-based cells are normally grown with a chemical bath deposited (CBD) CdS buffer layer. However, for an industrial production, a liquid based CBD intermediate step during the all in-line vacuum deposition processes introduces several drawbacks. Therefore, CIGS solar cells with physical vapour deposited (PVD)-CdS have been developed and compared with the standard cells with CBD-buffer layers. The efficiency of CIGS cells with CBD-CdS is in the range of 14-16 % while PVD-CdS yields 10-12 % efficiency cells. Solar cells with higher band gap alternative buffer layers of ZnS or ZnSe, grown by thermal or e-beam evaporation, are only 9 % efficient. Cells with Zn-chalcogenide buffer have over all lower collection efficiency (fig. 3.14).

High efficiency CIGS solar cells require an optimum concentration of Na. We have shown that presence of Na during CIGS growth can inhibit the formation of ternary chalcopyrite phases, influences the microstructure (grain size, surface roughness) and increases the electrical conductivity. We have developed a novel process for a controlled incorporation of Na in CIGS to improve the cell efficiency. In this method Na is diffused into the layer after the CIGS growth so that the detrimental effects of Na on CIGS growth kinetics can be avoided but the beneficial effects of grain boundary passivation are maintained. Efficiency gains of 15 % to 40 % have been achieved due to Na incorporation, depending on the CIGS deposition temperature. Solar cell efficiencies of 13.3 % and 14.4 % were achieved at substrate temperatures as low as 400 °C and 450 °C, respectively (fig. 3.15). These efficiencies are amongst the highest achieved with low deposition temperature processes.

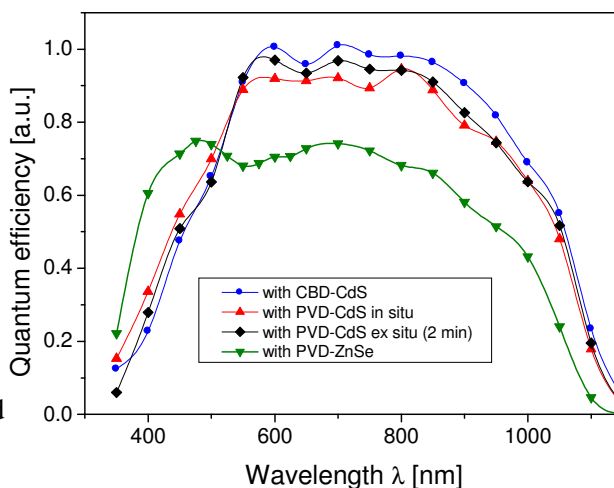


Figure 3.14: Quantum efficiency of CIGS solar cells with different buffer layers.

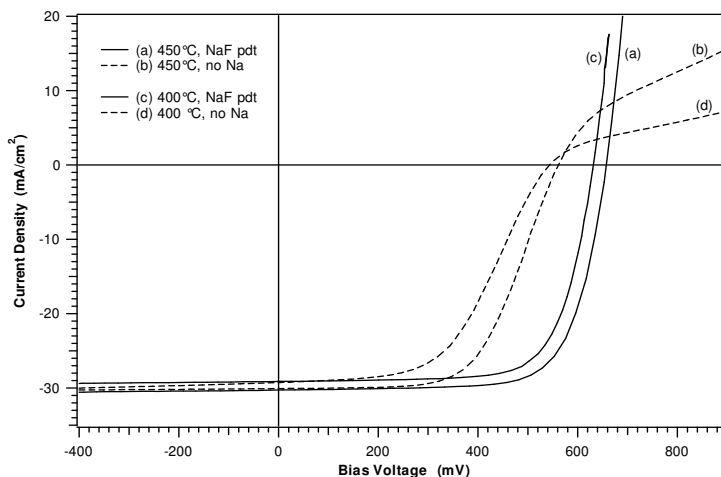


Figure 3.15: I–V curves of CIGS cells with and without Na incorporation at different growth temperatures. Efficiency gain of 15 to 40 % has been achieved with the novel post deposition method.

3.8.2.2 CdTe thin film solar cells

We have earlier shown that CdTe solar cells are extremely stable against high-energy electron and proton irradiation and their radiation tolerance is superior to conventional Si and III-V solar cells for space applications. Lightweight and flexible CdTe/CdS solar cells with 7.3 % efficiency in “substrate” configuration and >11 % efficiency in “superstrate” configuration have been developed with a low temperature deposition process. Either a spin-coated polyimide layer or a commercial (Upilex™) polyimide film is used as a substrate. In order to reduce the absorption loss in the substrate, very thin ($\sim 10 \mu\text{m}$) polyimide films are used for the cells in the superstrate configuration. Flexible CdTe solar cells with the record efficiency of 11.4 % have been achieved on a Upilex polyimide film (fig. 3.16, left). The fabrication processes are suitable for in-line production of solar cells and can be adapted for a roll-to-roll manufacturing. High efficiency flexible cells on polyimides show a specific power potential of $\sim 2 \text{ kW/kg}$ on the cell level.

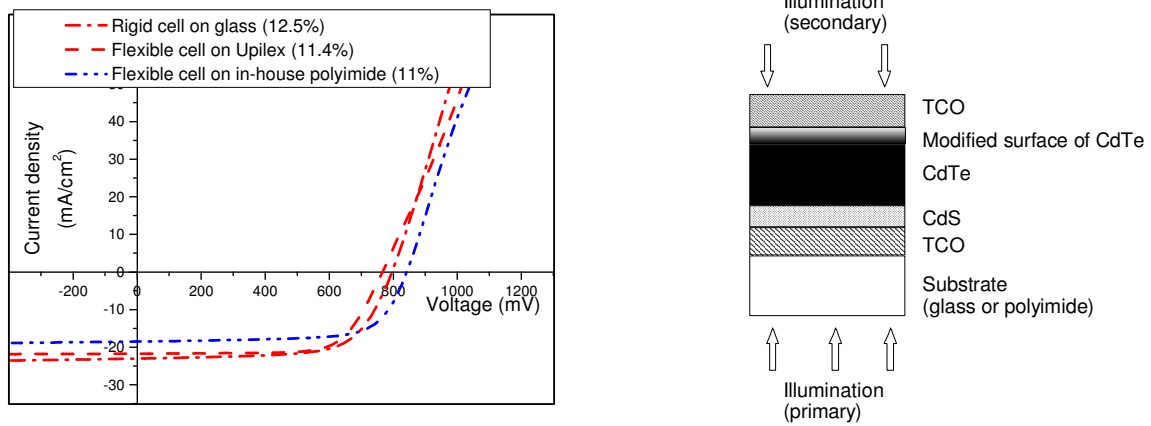


Figure 3.16: *Left:* I–V curves of CdTe solar cells on glass and polyimide under AM1.5 illumination. 11.4 % efficiency is a record for flexible CdTe solar cells. *Right:* Schematics of the novel CdTe solar cell in which TCO is used for the first time as a back contact on p-CdTe. The solar cell can be illuminated from either side. It is a conventional superstrate cell if illuminated only from the substrate side (primary illumination), while it operates like a “bi-facial” cell if simultaneously illuminated from both sides (primary and secondary illumination together). Such a solar cell configuration is also useful for tandem solar cells.

Chapter 4

Magnetism, Electron Spectroscopy

(<http://www.solid.phys.ethz.ch/pescia>)

Head

Prof. Dr. D.Pescia

Academic Staff

Prof. Dr. M. Erbudak

Dr. A. Vaterlaus (40%)

M. Buess (Ph.D student)

O.Portmann (Ph.D. student)

Dr. U. Ramsperger

T. Flückiger (Ph.D. student)

T. Michlmayr(PhD. student)

Dr. M. Hochstrasser

R. Lüscher (Ph.D. student)

Technical staff

K. Brunner(retired Sept. 2003)

T. Bähler (starting Oct. 2003)

U. Maier (20%)

L. Scherrer (30%)

4.1 Surface Physics

4.1.1 Self-assembled Al nanocrystals on the decagonal surface of the $\text{Al}_{70}\text{Co}_{15}\text{Ni}_{15}$

T. Flückiger, Y. Weisskopf, R. Lüscher, M. Erbudak, and A. R. Kortan

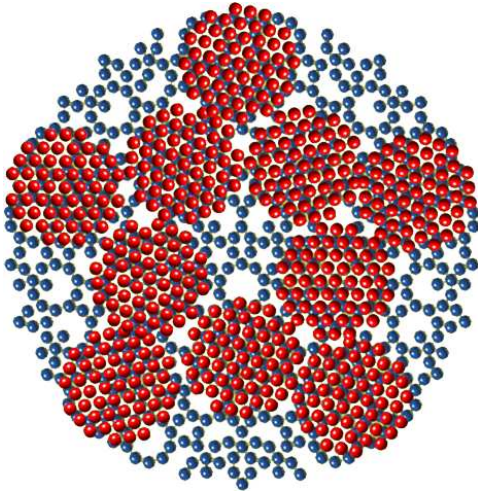


Figure 4.1: A schematic view of the substrate surface containing Al nanocrystals in ten discrete orientations, imposed by the aperiodic structure of the quasicrystalline template.

Periodicity is the unique characteristic of crystalline matter. Quasicrystals lack periodicity, but possess long-range orientational order with fivefold or tenfold point-group symmetries that cannot occur in crystals. Therefore, the structural transition on the atomic scale at the interface where an ordinary crystal and a quasicrystal intersect can potentially disclose structural mysteries of quasicrystalline surfaces and lead to novel surface phenomena. Generally, the equilibrium structure of the crystalline film on a quasicrystalline surface is determined by the relative strengths of epitaxy-imposed ordering versus the stable bulk phase of the film. We have studied the growth morphology of Al on the decagonal surface of $\text{Al}_{70}\text{Co}_{15}\text{Ni}_{15}$ using low-energy electron diffraction (LEED) and secondary-electron imaging (SEI). This surface is atomically flat and defect free. Up to roughly a monolayer coverage, there is no measurable change in the experimental observations. Hence, we conclude that epitaxy locks the Al atoms to the strained quasicrystalline lattice. For thicker Al coverages, the strain energy cannot be supported and the structure relaxes to the bulk stable face-centered cubic phase by breaking into multi-twinned domains, each a few nm large and oriented aperiodically according to the substrate structure.

As summarized in the figure, we can follow the growth of Al nanocrystals each having a diameter of about 3 nm and oriented with the [111] crystallographic direction parallel to the surface normal. Each Al island has a particular in-plane orientation enforced by the aperiodic structure of the decagonal surface. This observation on size selection and self orientation of Al nanocrystals holds promise in a number of important applications. We have reproduced these experimental results in model calculations representing the interface between Al and $\text{Al}_{70}\text{Co}_{15}\text{Ni}_{15}$ with a simplified electrostatic potential. Even taking the Al overlayer as a rigid mesh of the (111) surface, we have found that Al grows on the decagonal substrate in a particular size, distribution, and orientational alignment.

4.1.2 Structural compaction of the icosahedral quasicrystal $\text{Al}_{70}\text{Pd}_{20}\text{Mn}_{10}$

R. Lüscher, T. Flückiger, M. Erbudak, and A. R. Kortan

Al is vapor deposited onto the fivefold-symmetry surface of the icosahedral quasicrystal $\text{Al}_{70}\text{Pd}_{20}\text{Mn}_{10}$, kept at 770 K. We find that thick Al layers are readily diffused into the bulk without measurably influencing the surface order, chemically and structurally. We have monitored the Al-absorption process by measuring the temperature dependence of the specular-beam intensity in LEED. This procedure allows us to determine the surface Debye temperature, which is a measure for the atomic mean-square vibrational amplitude $\langle u^2 \rangle$ normal to the surface. The value associated with the pentagonal surface (298 ± 7 K) is very close to the bulk value of 312 K, determined in x-ray diffraction. This implies that the quasicrystalline bulk closely resembles the surface from the point of view how the vibrational modes are developed. This result is in agreement with the reported richness of vacancies in the bulk $\text{Al}_{70}\text{Pd}_{20}\text{Mn}_{10}$. We find that by adsorbing 195-Å thick Al, the surface Debye temperature increases by as much as 100 K. This amounts to a decrease of the vibrational amplitude by more than 20%. Thus, the quasicrystalline surface structure gains additional rigidity by the incorporation of Al. This stability can be reached by filling of the vacancy-rich, open-structured pentagonal surface of the $\text{Al}_{70}\text{Pd}_{20}\text{Mn}_{10}$ quasicrystal with Al. Our data indicate a vacancy concentration of about 1 – 2% in a region of a few surface layers accessible with surface-sensitive techniques used in this work.

4.1.3 Atomic structure of the Al_2O_3 (10·0) surface

M. Erbudak, T. Flückiger, A. R. Kortan, and R. Lüscher

Sapphire, $\alpha\text{-Al}_2\text{O}_3$, is a technologically important material which finds applications in many different fields. In microelectronics, it presents itself as an ideal substrate material because of its superior physical and chemical properties. The Al_2O_3 primitive unit cell is rhombohedral, but more often it is referred to by a non-primitive hexagonal (HK·L) unit cell. Its crystal structure can be described as six O layers along the [00·1] hexagonal axis, stacked as hcp, and twelve Al layers in fcc stacking. We have characterized the (10·0) surface of Al_2O_3 structurally and chemically using electron probes, such as LEED, SEI, and Auger electron spectroscopy. For insulating surfaces, SEI and AES are performed at the unity crossover energy of the secondary-electron yield. The atomic structure in a near-surface region of about 3 nm is investigated by SEI. The observations are reproduced by corresponding electron-scattering calculations. We find that above 630 K, the surface becomes gradually enriched in Al, probably due to the desorption of O, up to an excess atomic layer of Al. Further, LEED studies reveal a bulk-derived atomic structure of the surface.

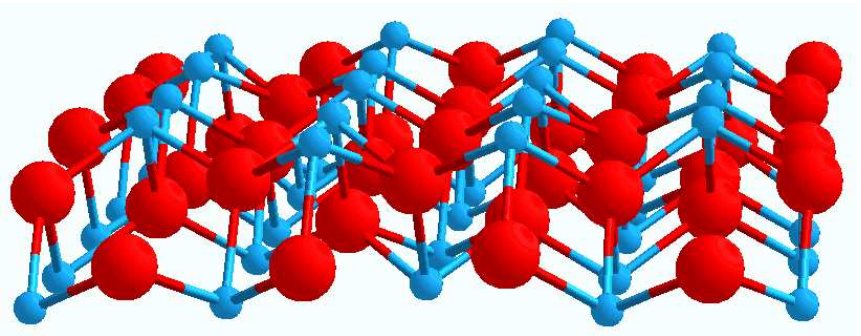


Figure 4.2: The (10·0) surface of Al_2O_3 in the corundum structure.

4.2 Magnetism

4.2.1 Labyrinthine to striped pattern inverse transition in perpendicularly magnetized ultrathin films

O. Portmann, A. Vaterlaus, D. Pescia, *Nature* **422**, 701-704 (2003) Stripe domains of opposite magnetization appear in perpendicularly magnetized films because the long-range dipolar coupling, albeit very weak, destabilizes the state of uniform perpendicular magnetization favoured by the short-range exchange interaction. In this respect, this system belongs to a wide class of pattern forming systems where two counteracting interactions give rise to a modulated ground state. The disordering scenario of the striped ground state is most controversial. Mean-field arguments predict a continuous reduction of the stripe width when the temperature is increased. At the onset of paramagnetism the magnetization within the stripes vanishes. Other studies suggest that topological defects, such as dislocations and disclinations, might penetrate the system below the mean-field transition temperature and drive the disordering by means of a special class of phase transitions, known as topological phase transitions. The outcome of disordering is a liquid domain state or a labyrinthine state. The liquid domain structure might even form an intermediate state between the striped and the paramagnetic phase. This last scenario is reminiscent of the Kostrelitz-Thouless-Nelson-Halperin-Young model of two-dimensional melting, which foresees that a two-dimensional "floating" solid like the striped domain structure in ultrathin films undergoes a two-step melting process. In this experiment we have imaged the domain structure of perpendicularly magnetized ultrathin fcc Fe films grown epitaxially on Cu(100). The novel elements found here are the following:

1. The disordering process is characterized by a phase transition from the striped ground state into an intermediate labyrinthine phase with six-fold symmetry. This transition is promoted by a transversal front instability.
2. The labyrinth is followed by the re-entrance of the stripe order (see top four images in the figure). Stripe order is less symmetric than a labyrinthine order: we thus observe an "inverse freezing" process which is a possible but very unusual phenomenon. The re-entrance of the stripes is mediated by bridge and knee-bend instabilities of the disclination network, which are documented in our images for the first time (bottom four images).
3. Upon cooling from the paramagnetic phase, the first structure to be formed are striped domains, the more symmetric

labyrinthine phase re-enter the system after some time. This is an example of inverse melting, which seems to be promoted by bubble defects of the stripe phase.

As topological phase transitions in striped matter are based on pure geometrical considerations, the discovery of these novel elements should be significant for any type of stripe order, even if it is encountered in a totally different context, such as the striped quantum liquid crystal phases envisaged recently in connection with copper oxide superconductors or the Quantum Hall effect.

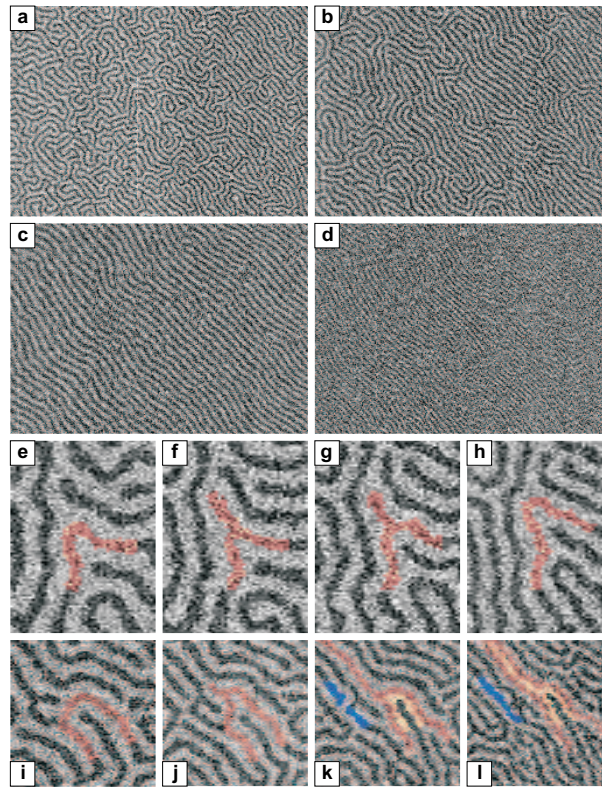


Figure 4.3: Top four images: the labyrinthine-stripe reentrant transition. Bottom four images: details of the microscopic mechanisms of the transition.

4.2.2 Pulsed precessional motion on the 'back of an envelope'

M. Buess, Y. Acremann, A. Kashuba, C.H. Back, D. Pescia, J. Phys: Condens. Matter **15** R1093 (2003) In a recent paper (Acremann Y et al. 2000 *Science* **290** 492) the precessional trajectory of the magnetization vector was imaged with spatial resolution as a function of the time elapsed after a very short (some picoseconds duration) magnetic field pulse was applied. The most surprising observations – the reversal the magnetic excitation upon reflection from the boundary and the spatial non-uniformities of the precessional mode – have remained unaccounted for so far. Here we present a "back of the envelope" model of the precessional motion that is analytical, free of adjustable parameters, and that reproduces all the essential experimental features – including the behavior of the dynamical magnetization at boundaries. In the experimental work quoted, the magnetic element was a very thin Co-disk (radius $R \sim 3\mu\text{m}$, thickness $d \sim 20$ nm). The ground state magnetization distribution consisted of at least four in-plane magnetized domains arranged to produce an almost "circulating" flux closure configuration. Of the experimental images taken after exciting the magnetization vector \vec{M} with a short magnetic field pulse, we consider here the images pertaining to the component of the magnetization vector that could be detected with the greatest precision, namely the one perpendicular to the plane on the disk (M_z). M_z is imaged as a function of the position within the disk and of the time t elapsed after application of the magnetic field pulse with $\approx 0.3\mu\text{m}$ lateral spatial resolution and with pico-second time resolution. The images display – as expected from the symmetry of the ground state – an approximate axial symmetry, i.e.

they are approximately invariant with respect to rotations around a z -axis passing through the center of the disk. Because of this axial symmetry, we restrict ourselves, without losing experimental information, to re-plotting the experimental $M_z(t, \vec{r})$ along one single axis " x " passing through the origin of the disk, see the top figure. Here, the spatial coordinate x is along the vertical scale, the time-coordinate t is along the horizontal scale. The gray scale used to plot the experimental data is a measure of the strength of M_z , white and black indicating opposite orientations. The main features of Fig.2A are the following: The magnetic excitation builds up at the boundaries ("A"), propagates to the center ("B"), where it is reflected back **with reversed amplitude**. After hitting the boundary of the disk, the excitation **reverses sign again** ("C") and travels back to the center ("D"). The pattern of Fig.2A can be roughly described as a $>$ -shaped excitation repeating periodically in time. The period can be directly read out from the figure. The mathematical model we have developed to reproduce the experimental image just described involves solving the Landau-Lifshitz (LL) equation containing the relevant magnetic interactions. It turns out that the problem can be reduced to the equation of motion of uncoupled classical harmonic oscillators and thus solved analytically. The bottom of the figure shows the analytical mode expansion. This figure, which essentially shows how the mixture of eigenmodes evolves in time and space, reproduces qualitatively as well as quantitatively the $>$ -shaped excitation front. In particular, the back and forth propagation of the excitation crest between A, B, C, D is the result of eigenmodes with appropriate frequency and spatial dependence coherently superposing to move the excitation crest and change its sign as observed in the experiment.

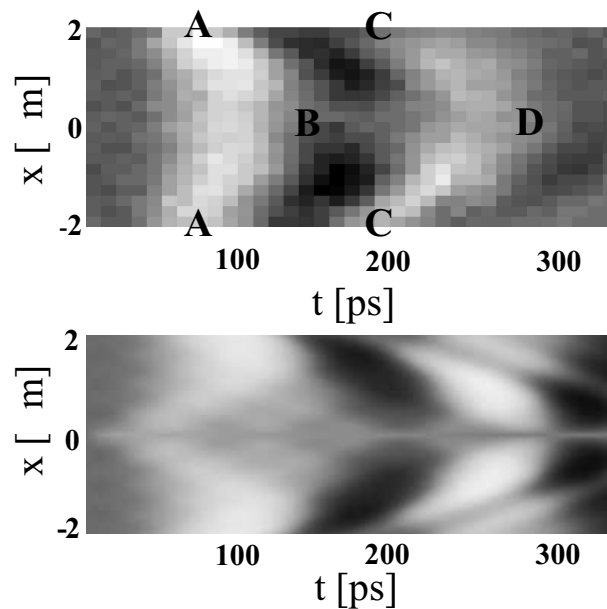


Figure 4.4: The top part show the experimental data $M_z(x, t)$. The bottom part is the corresponding analytical solution.

Chapter 5

Publications

K. Alchalabi, D. Zimin, H. Zogg

Self Assembled PbSe Quantum Dots with Almost Equal Sizes Grown by MBE on PbTe/Si(111)
Mat. Res. Soc. Symp. Proc. Vol. **737**, E5.5.1-5, (2003)

K. Alchalabi, D. Zimin, G. Kostorz, H. Zogg

Self-Assembled Semiconductor Quantum Dots with Nearly Uniform Sizes
Physics Review Letters **90**, 026104, 4 pages, (2003)

M. Angst, R. Puzniak, A. Wisniewski, J. Roos, H. Keller, P. Miranovic, J. Jun, S.M. Kazakov, J. Karpinski

Anisotropy of the superconducting state properties and phase diagram of MgB₂ by torque magnetometry on single crystals
Physica C **385** 143-154, (2003)

M. Angst, R. Puzniak, A. Wisniewski, J. Jun, S. M. Kazakov, and J. Karpinski

Disorder-induced phase transition of vortex matter in MgB₂
Phys. Review **B 67**, 012502, (2003)

C. Bergemann, A.P. Mackenzie, S.R. Julian, D. Forsythe, E. Ohmichi

Quasi-Two-Dimensional Fermi Liquid Properties of the Unconventional Superconductor Sr₂RuO₄
Adv. Physics, **52**, 639 (2003)

C. Bergemann, H. Keymeulen, J.F. van der Veen

Focusing X-Ray Beams to Nanometer Dimensions
Physics Review Letters, **91**, 204801 (2003)

S. Broderick, L. Degiorgi, H.R. Ott, J.L. Sarrao, Z. Fisk

Polar Kerr rotation of the ferromagnet EuB₆
Eur. Phys. J. **B33**, 47 (2003)

S. Broderick, L. Degiorgi, H.R. Ott, J.L. Sarrao, Z. Fisk

Polar Kerr rotation on the ferromagnet EuB₆
Eur. Phys. J.B. **33**, 47-54 (2003)

M. Buess, Y. Acremann, A. Kashuba, C.H. Back, D. Pescia

Pulsed Precessional Motion on the 'back of an envelope'
Journal of Physics: Condensed Matter **15**, R1093-R1100 (2003)

- Y. Bukhantsev, B. Kundys, A. Nabialek, S. Vasiliev, A. Wisniewski, J. Jun, S.M. Kazakov, J. Karpinski, H. Szymczak
The correlation between the transverse and longitudinal magnetostriction in a polycrystalline MgB_2 superconductor
Supercond. Science Technol. **16**, 707, (2003)
- Y. Bukhantsev, A. Nabialek, B. Kundys, S. Vasiliev, A. Wisniewski, J. Jun, S.M. Kazakov, J. Karpinski, A. Szewczyk, H. Szymczak
Pinning induced magnetostriction in superconducting MgB_2 ceramics
Physics State Solid (a) **No.1**, 82 (2003)
- A. Carrington, P.J. Meeson, J.R. Cooper, L. Balicas, N.E. Hussey, E.A. Yelland, S. Lee, A. Yamamoto, S. Tajima, S.M. Kazakov, J. Karpinski
Determination of the Fermi Surface of MgB_2 by the de Haas-van Alphen Effect
Physics Review Letters **91**, 037003, (2003)
- V. Chabanenko, R. Puzniak, A. Nabialek, S. Vasiliev, V. Rusakov, L. Huanquian, R. Szymczak, H. Szymczak, J. Jun, J. Karpinski, V. Finlel
Flux jumps and H-T diagram of instability for MgB_2
Journal of Low Temperature **3-4** 175-191, (2003)
- M.A. Chernikov, C. Beeli, E. Felder, S. Büchi, H.R. Ott
Spin freezing in the decagonal phase of the Al-Mn-Pd alloy system
Physical Review B **68**, 094202 (2003)
- M. Chiao, G. Wigger, C. Bergemann, H.R. Ott, S.S. Saxena, A.D. Bianchi, Z. Fisk
Tuning of Magnetic Moment in $\text{Eu}(1-x)\text{Ca}x\text{B}_6$
Acta Physics Pol. **B 34**, 1441, (2003)
- J.R. Cooper, A. Carrington, P.J. Meeson, E.A. Yelland, N.E. Hussey, L. Balicas, S. Tajima, S. Lee, S.M. Kazakov, J. Karpinski
de Haas-van Alphen effect in MgB_2 crystals
Physica C **385** 75-85, (2003)
- R. Cubitt, M.R. Eskildsen, C.D. Dewhurst, J. Jun, S.M. Kazakov, J. Karpinski
Effects of two-band superconductivity on the flux line lattice in Magnesium Diboride
Physics Review Letters, **91**, 047002, (2003)
- D. Daghero, R.S. Gonnelli, G.A. Ummarino, V.A. Stepanov, J. Jun, S.M. Kazakov, J. Karpinski
Point-contact spectroscopy in MgB_2 single crystals in magnetic field
Physica C **385** 255-264, (2003)
- L. Degiorgi
Optical properties of correlated systems in Concepts in Electron Correlation, Proceedings of the ARW NATO Workshop Hvar, Croatia, October 2002, page 363
Eds. A.C. Hewson, V. Zlatic, Kluwer Academic Publishers (2003)
- S.V. Dordevic, D.N. Basov, R.C. Dynes, B. Ruzicka, V. Vescoli, L. Degiorgi, H. Berger, R. Gaál, L. Forró, E. Bucher
Optical properties of the quasi-two-dimensional dichalcogenides 2H-TaSe_2 , 2H-NbSe_2
Eur. Phys. J. **B33**, 15 (2003)

- A. Dorn, M. Peter, S. Kicin, T. Ihn, K. Ensslin, D. Driscoll, A. C. Gossard
Charge tunable ErAs islands for backgate isolation in AlGaAs heterostructures
Appl. Phys. Lett. **82**, 2631 (2003)
- A. Dorn, P. Stauffenegger, T. Ihn, K. Ensslin, W. Wegscheider, M. Bichler
Ballistic electron transport through open squares
Proceedings of the 26th International Conference on the Physics of Semiconductors, Edinburgh, UK, paper P250 (2003)
- M. Enciso-Aquilar, F. Aniel, P. Crozet, R. Adde, H.-J. Herzog, T. Hackbarth, U. König, and H. von Känel
DC and high frequency performance of a 0.1 μ m n-type Si/Si_{0.6}Ge_{0.4} MODFET with f_{max} =188 GHz at 300 K and f_{max} =230 GHz at 50 K
Electronic Letters **39**, 149, (2003)
- M.R. Eskildsen, N. Jenkins, G. Levy, M. Kugler, Ø.Fischer, J. Jun, S.M. Kazakov, J. Karpinski
Vortex Imaging in Magnesium Diboride with H²c
Phys. Review **B 68**, 100508, (2003)
- M.R. Eskildsen, M. Kugler, G. Levy, S. Tanaka, J. Jun, S.M. Kazakov, J. Karpinski, Ø.Fischer
Scanning Tunneling Spectroscopy on Single Crystals MgB₂
Physica C **385** 169-177, (2003)
- T. Flückiger, T. Michlmayr, C. Biely, R. Lüscher, M. Erbudak
Structural transitions at the surface of the decagonal quasicrystal Al-Co-Ni
Applied Surface Science 212-213, 43-46 (2003)
- T. Flückiger, R. Lüscher, M. Erbudak, A.R. Kortan
Electronic excitations at the threefold-symmetric surface of the quasicrystal Al-Pd-Mn
Surface Science 532-535, 25-29 (2003)
- T. Flückiger, Y. Weisskopf, M. Erbudak, R. Lüscher, A.R. Kortan
Nano-epitaxy size selection in self-assembled and oriented Al nano-crystals grown on a quasicrystal surface
Nano Letters 3, 1717-1721 (2003)
- A. Franco-Obregón, R. D. Jäggi, K. Ensslin
Probing the nucleus
Bioworld **4**, 10 (2003)
- A. Fuhrer, T. Ihn, K. Ensslin, W. Wegscheider, M. Bichler
Singlet-Triplet Transition Tuned by Asymmetric Gate Voltages in a Quantum Ring
Phys. Rev. Lett. **91**, 206802 (2003)
- J.L. Gavilano, D. Rau, S. Mushkolaj, H.R. Ott, P. Millet, F. Mila
Low-Dimensional Spin S = 1/2 System at the Quantum Critical Limit: Na₂V₃O₇
Physical Review Letters, Vol. **90**, Number 16 (2003)
- J.L. Gavilano, S. Mushkolaj, D. Rau, H.R. Ott, A. Bianchi, Z. Fisk
NMR studies of YbB₆
Physica B **326-333**, 570-571 (2003)

J.L. Gavilano, D. Rau, S. Mushkolaj, H.R. Ott, F. Mila, P. Millet

Low-temperature NMR studies of $\text{Na}_2\text{V}_3\text{O}_7$

Physica B **329-333**, 703-704 (2003)

K. Giannò, A.V. Sologubenko, H.R. Ott, A.D. Bianchi, Z. Fisk

Low-temperature thermal conductivity of CaB_6 and EuB_6

J. Phys.: Condens. Matter **15**, 6739-6748 (2003)

R.S. Gonnelli, D. Daghero, G.A. Ummarino, V.A. Stepanov, J. Jun, S.M. Kazakov, J. Karpinski

Independent determination of the two gaps by directional point-contact spectroscopy in MgB_2 single crystals

Sup. Science Techn., **16** 171-175, (2003)

F.-J. Haug, D. Rudmann, H. Zogg and A. N. Tiwari

Light soaking effects in $\text{Cu}(\text{In,Ga})\text{Se}_2$ superstrate solar cells

Thin Solid Films **431-432**, 431-435, (2003)

T. Heinzl, R.D. Jaeggi, E. Ribeiro, M. v. Waldkirch, K. Ensslin, S.E. Ulloa, G. Medeiros-Ribeiro, P.M. Petroff

Transport signatures of correlated disorder in a two-dimensional electron gas

Europhy. Lett. **61**, 674 (2003)

T. Ihn, A. Fuhrer, T. Heinzl, K. Ensslin, W. Wegscheider, M. Bichler

Marvellous things in marvellous rings: energy spectrum, spins and persistent currents

Physica E **16**, 83 (2003)

T. Ihn, A. Fuhrer, M. Sigrist, K. Ensslin, W. Wegscheider, M. Bichler

Quantum Mechanics in Quantum Rings

Adv. in Solid State Phys. **43**, 139 (2003)

R.D. Jäggi, A. Franco-Obregón, K. Ensslin

Quantitative topographical analysis of Nuclear Pore Complex function using Scanning Force Microscopy

Biophysical Journal **85**, 4093 (2003)

R.D. Jäggi, A. Franco-Obregón, P. Mühlhäusser, F. Thomas, U. Kutay, K. Ensslin

Modulation of Nuclear Pore Topology by Transport Modifiers

Biophys. Journal **84**, 665 (2003)

M. Kaelin, D. Rudmann, F. Kurdesau, T. Meyer, H. Zogg and A. N. Tiwari

CIS and CIGS layers from selenized nanoparticle precursors

Thin Solid Films **431-432**, 58-62, (2003)

J. Karpinski, M. Angst, J. Jun, S.M. Kazakov, R. Puzniak, A. Wisniewski, J. Roos, H. Keller, A. Perucchi, L. Degiorgi,

M.R. Eskildsen, P. Bordet, L. Vinnikov, A. Mironov

MgB_2 single crystals: high pressure growth and physical properties

Supercond. Sci. Technol. **16**, 221 (2003)

J. Karpinski, S.M. Kazakov, J. Jun, M. Angst, R. Puzniak, A. Wisniewski, P. Bordet

Single crystal growth of MgB_2 and thermodynamics of Mg-B-N system at high pressure

Physica C **385** 42-48, (2003)

- K. Kellermann, D. Zimin, K. Alchalabi, P. Gasser, N.A. Pikhtin, H. Zogg
Optically pumped lead-chalcogenide mid-infrared lasers on Si-substrates
Journal Applied Physics **94**, pp.7053-7058, (Dec. 2003)
- K. Kellermann, D. Zimin, K. Alchalabi, N.A. Pikhtin, H. Zogg
Optically pumped lead-chalcogenide IR-emitters
IEE Proceedings - Optoelectronics, **150**, 337-339, (2003)
- D. L. Bätzner, G. Agostinelli, M. Campo, A. Romeo, J. Beier, H. Zogg and A. N. Tiwari
Study of spatially resolved impurity diffusion in CdTe solar cells using voltage dependent quantum efficiency
Thin Solid Films **431-432**, 421-425, (2003)
- R. Lüscher, T. Flückiger, M. Erbudak, A.R. Kortan
Debye temperature of the pentagonal surface of the quasicrystal Al-Pd-Mn
Surface Science 532-535, 8-12 (2003)
- R. Lüscher, T. Flückiger, M. Erbudak, A.R. Kortan
Evidence for surface compaction in Al-incorporated Al-Pd-Mn quasicrystal
Physical Review B 68 2122031-2122034 (2003)
- I.L. Landau, H.R. Ott
Some remarks on vortex matter in high- T_c superconductors
J. Low Temperature Physics, Vol. **130** (2003)
- I.L. Landau, H.R. Ott
Temperature dependence of the upper critical field of high- T_c superconductors from isothermal Magnetization data.
Application to polycrystalline samples and ceramics
Physica C **385**, 544-550 (2003)
- I.L. Landau, H.R. Ott
Equilibrium magnetization of high- T_c superconductors below the irreversibility line
Physical Review B **67**, 092505 (2003)
- I.L. Landau, H.R. Ott
Temperature dependence of the upper critical field of high- T_c superconductors from isothermal magnetization data:
influence of a temperature dependent Ginzburg-Landau parameter
Physica C 398, 73-77 (2003)
- I.L. Landau, A.V. Sologubenko, H.R. Ott
Ambivalence of the anisotropy of the vortex lattice in an anisotropic type-II superconductor
Physical Review B **68**, 132506 (2003)
- R. Leturcq, D. L'Hote, R. Tourbot, V. Senz, U. Gennser, T. Ihn, K. Ensslin, G. Dehlinger, D. Grützmacher
Hot-hole effects in a two-dimensional gas in SiGe
Europhys. Lett. **61**, 499 (2003)
- S. Lindemann, T. Ihn, T. Heinzl, K. Ensslin, K. Maranowski, A. C. Gossard
Stability of spin states in quantum dots
Proceedings of the 26th International Conference on the Physics of Semiconductors, Edinburgh, UK, paper H186
(2003)

- E. Müller, O. Kierfel, A. Rastelli, H. von Känel, and D. Grützmacher
Successful shape preservation of Ge-clusters during Si-coverage at low temperature
Material Science & Engineering B **101**, 142, (2003)
- G. Matteucci, D. Iencinella, C. Beeli
The Aharonov-Bohm Phase Shift and Boyer's Critical Considerations: New Experimental Result but Still an Open Sujet?
Foundations of Physics, Vol. **33**, No. 4 (2003)
- S. Moré, E.A. Soares, M. A. van Hoove, S. Lizzit, A. Baraldi, Ch. Grütter, J.H. Bilgram, Ph. Hofmann
?-Gallium (010) surface phase reconstruction: A LEED structural analysis of the (1?1) room temperature and R45° low temperature structures
Phys. Rev. B **68**, 75414 (2003)
- H.R. Ott
High- T_c Superconductivity
The Physics of Superconductors Vol. I, eds. K.H. Bennemann and J.B. Ketterson, p. 385-494 (Springer, Berlin, 2003)
- A. Perucchi, L. Degiorgi, J. Jun, M. Angst, J. Karpinski
Far-infrared optical properties of MgB₂ single crystals
Physica **C385**, 273 (2003)
- A. Perucchi, L. Degiorgi, J. Jun, M. Angst, J. Karpinski
Far-infrared optical properties of MgB₂ single crystals
Physica C **385** 273-278, (2003)
- A. Pioda, V. Senz, T. Ihn, T. Heinzel, K. Ensslin, W. Wegscheider, M. Bichler
Electron transport through an array of coherently coupled cavities
Proceedings of the 26th International Conference on the Physics of Semiconductors, Edinburgh, paper P252 (2003)
- O. Portmann, A. Vaterlaus, D. Pescia
An inverse transition of magnetic domain patterns in ultrathin films
Nature **422**, 701-704 (2003)
- M. R. Eskildsen, M. Kugler, S. Tanaka, J. Jun, S. M. Kazakov, J. Karpinski, Ø. Fischer
Vortex lattice imaging in single crystal MgB₂ by scanning tunneling spectroscopy
Physica C **388-389** 143-144, (2003)
- A. Rühm, H. Reichert, W. Donner, H. Dosch, Ch. Grütter, J. Bilgram
Bulk surface pre-melting phenomena in ?-gallium
Phys. Rev. B **68**, 224110 (2003)
- B. Rössner, G. Isella, H. von Känel
Effective mass in remotely doped Ge quantum wells
Applied Physics Letters **82**(5), 754 (2003)
- D. Rau, J.L. Gavilano, S. Mushkolaj, C. Beeli, H.R. Ott
Magnetism of decagonal Al_{69.8}Pd_{12.1}Mn_{18.1}
Physica B **329-33**, 1103-1104 (2003)

- D. Rau, J.L. Gavilano, S. Mushkolaj, C. Beeli, M.A. Chernikov, H.R. Ott
Anomalous magnetism in decagonal $\text{Al}_{69.8}\text{Pd}_{12.1}\text{Mn}_{18.1}$
Physical Review B **68**, 13204 (2003)
- D. Rudmann, G. Bilger, M. Kaelin, F. -J. Haug, H. Zogg and A. N. Tiwari
Effects of NaF coevaporation on structural properties of $\text{Cu}(\text{In,Ga})\text{Se}_2$ thin films
Thin Solid Films **431-432**, 37-40, (2003)
- B. Ruzicka, V. Vescoli, L. Degiorgi
Charge dynamics in low-dimensional quantum systems
J. Phys.: Condens. Matter **15**, S2501 (2003)
- G. Salis, Y. Kato, K. Ensslin, D. C. Driscoll, A. C. Gossard, D. D. Awschalom
Electrical control of spin precession in semiconductor quantum wells
Physica E **16**, 99 (2003)
- A. Shukla, M. Calandra, M. d'Astuto, M. Lazzeri, F. Mauri, Ch. Bellin, M. Krisch, J. Karpinski, S. M. Kazakov, J. Jun, D. Daghero, K. Parlinski
Phonon dispersion and lifetimes in MgB_2
Physics Review Letters **90**, 095506, (2003)
- A.V. Sologubenko, H.R. Ott, G. Dhalenne, R. Revcolevschi
Universal behaviour of spin-mediated energy transport in $S = 1/2$ chain cuprates: $\text{BaCu}_2\text{Si}_2\text{O}_7$ as an example
Europhysics Letters, Vol. **62**, Number 4, pp. 540-546 (2003)
- V. Sologubenko, J. Jun, S.M. Kazakov, J. Karpinski, H.R. Ott
Anomalous low-temperature thermal conductivity of MgB_2
Physica C **388-389**, 133-134 (2003)
- A.V. Sologubenko, S.M. Kazakov, H.R. Ott
Diffusive energy transport in the $S = 1$ Haldane chain compound AgVP_2S_6
Physical Review B **68**, 094432 (2003)
- A.V. Sologubenko, I.L. Landau, H.R. Ott, A. Bilusic, A. Smontara, H. Berger
Unusual Magnetic-Field-Induced Phase Transition in the Mixed State of Superconducting NbSe_2
Physical Review Letters, Vol. **91**, Number 19 (2003)
- A.V. Sologubenko, J. Jun, S.M. Kazakov, J. Karpinski, H.R. Ott
Anomalous low-temperature thermal conductivity of MgB_2
Physica C **388-389** 133, (2003)
- Ch. Sondergaard, Ch. Schultz, S. Agergaard, S.V. Hoffmann, Z. Li, Ph. Hofmann, H. Li, Ch. Grütter, J.H. Bilgram
Interplay between electronic structure and surface phase transition on $\sqrt{3}\times\sqrt{3}$ -Ga(010)
Phys. Rev. B **67**, 165422 (2003)
- Ch. Sondergaard, Ch. Schultz, S. Agergaard, H. Li, Z. Li, S.V. Hoffmann, Ch. Grütter, J.H. Bilgram, Ph. Hofmann
Electronic structure of $\sqrt{3}\times\sqrt{3}$ -Ga
Phys. Rev. B **67**, 205105 (2003)

I. Stalder, J. H. Bilgram

The measurement of the solid-liquid surface free energy of xenon

J. Chem. Phys. 118, 7981 (2003)

K. Suter, T. Akiyama, N. F. de Rooij, A. Baumgartner, T. Ihn, K. Ensslin, U. Staufer

Tuning Fork AFM with Conductive Cantilever

AIP Conference Proceedings, **696**, 227 (2003)

J. Takeya, C. Goldmann, S. Haas, K.P. Pernstich, B. Batlogg, and B. Ketterer

Field-induced charge transport at the surface of pentacene single crystals: A method to study charge dynamics of two-dimensional electron systems in organic crystals

Journal Applied Physics **94** /9, 5800-5804 (November 1st, 2003)

S.G. Thomas, S. Bharatan, R.E. Jones, R. Thoma, T. Zirkle, N.V. Edwards, R. Liu, X.D. Wang, Q. Xie, C. Rosenblad, J. Ramm, G. Isella, and H. von Känel

Structural characterization of thick, high-quality epitaxial Ge on Si substrates grown by low-energy plasma-enhanced chemical vapor deposition

Journal Electronic Materials **32**, 976, (2003)

A.N. Tiwari, D. Rudmann, A.F. da Cunha*, M. Kaelin, F.-J. Haug**, H. Zogg

Effects of Na on the Growth of Cu(In,Ga) Se₂ Thin Films and Solar Cells

Mat. Res. Soc. Symp. Proc. Vol. **763**, 53-64 (2003)

T. Uchihashi, U. Ramsperger

Atomic scale characterization of metal micro-electrodes grown on clean semiconductor surfaces

Thin Solid Films 438-439, 61-64 (2003)

T. Uchihashi, U. Ramsperger

Phase transition of the Si(111) 4X1-In surface reconstruction investigated by electron transport measurements

Surface Science 532-535, 685-689 (2003)

T. Uchihashi, U. Ramsperger

Electron transport through indium atomic chain arrays self-assembled on a silicon surface

Physica E: Low dimensional Systems and Nanostructures 18, 227-228 (2003)

T. Vancura, S. Kicin, T. Ihn, K. Ensslin, M. Bichler, W. Wegscheider

Scanning probe-based local spectroscopy of semiconductor heterostructures below 300 mK

Proceedings of the 26th International Conference on the Physics of Semiconductors, Edinburgh, UK, paper P175 (2003)

T. Vancura, S. Kicin, T. Ihn, K. Ensslin, M. Bichler, W. Wegscheider

Kelvin Probe Spectroscopy of a Two-Dimensional Electron Gas Below 300 mK

Appl. Phys. Lett. **83**, 2602 cond-mat/0308069, (2003)

L. Ya. Vinnikov, J. Karpinski, S. M. Kazakov, J. Jun, J. Anderegg, S. L. Bud'ko, P. C. Canfield

Vortex structure in MgB₂ single crystals by Bitter decoration technique

Phys. Review **B 67**, 092512, (2003)

L. Ya. Vinnikov, J. Karpinski, S.M. Kazakov, J. Jun, J. Anderegg, S. L. Bud'ko, P. C. Canfield

Bitter decoration of vortex structure in MgB₂ single crystals

Physica C **385** 177-179, (2003)

P. Wachter, B. Bucher, J. Malar

A superfluid phase in a Bose condensed excitonic state
Acta Physica Polonica B **34**, 897 (2003)

P. Wachter, B. Bucher, J. Malar

Evidence of a superfluid phase in a Bose condensed excitonic state
Europhys. Lett. **62**, 343 (2003)

P. Wachter

Intermediate valence of plutonium chalcogenides as determined by photoemission
Solid State Commun. **127**, 599 (2003)

P. Wachter, B. Bucher, J. Malar

Evidence of a superfluid phase in a Bose condensed excitonic state
Proc. Workshop RWTH Aachen, 60th anniversary, Aachen, pg 1 (2003)

M. Zehetmayer, F.M. Sauerzopf, H.W. Weber, J. Karpinski, M. Murakami

Comparative study of sequential neutron irradiation and annealing effects in superconducting $\text{YBa}_2\text{Cu}_3\text{O}_{7-x}$, $\text{Y}_2\text{Ba}_4\text{Cu}_8\text{O}_{16}$ and $\text{NdBa}_2\text{Cu}_3\text{O}_{7-x}$ single crystals
Physica C **383**, 232-240, (2002)

M. Zehetmayer, M. Eisterer, H.W. Weber, J. Jun, S.M. Kazakov, J. Karpinski

Reversible and irreversible properties of superconducting MgB_2
Physica C **388-389**, 159, (2003)

M. Zeuner, T. Hackbarth, M. Enciso-Aguilar, F. Aniel, and H. von Känel

Sub-100 nm gate technologies for Si/SiGe buried channel RF devices
Japanese Journal Applied Physics **42**, 2363, (2003)

H. Zogg, K. Alchalabi, D. Zimin, K. Kellermann, W. Buttler

Two-dimensional monolithic lead-chalcogenide infrared sensor array on silicon read-out chip
Nucl. Instr. Meth. in Physics Research **A512**, 440-444, (Oct 2003)

H. Zogg

Lead Chalcogenide Infrared Detectors Grown on Silicon Substrates, in *Optoelectronic Properties of Semiconductors and Superlattices*, M.O. Manasreh, Series editor, Vol. 18, Lead Chalcogenides: Physics and Applications, D. Khokhlov ed., Taylor & Francis Books, Inc., New York and London, pp 587-616, (2003)

H. Zogg, K. Alchalabi, D. Zimin, K. Kellermann

Two-dimensional monolithic lead chalcogenide infrared sensor arrays on silicon read-out chips and noise mechanisms
IEEE Trans. Electron Devices **ED50**, pp. 209 – 214, (Jan 2003)

Chapter 6

Talks

(* = invited)

Alchalabi K.
Bleisalz-Infrarot-Emitter auf Si-Substraten
Deutscher MBE-Workshop, München, Deutschland, 17.10.2003

Alchalabi K.
Self assembled PbSe quantum dots with nearly uniform sizes on PbTe/Si(111)
12th Euro-MBE workshop, Bad Hofgastein, Austria, 16.2.2003

Arnold M.
Bleisalz-Infrarot-Sensor-Array auf CMOS-Substrat
Deutscher MBE-Workshop, München, Deutschland, 16.10.2003

* Bätzner D.L.
Stability aspects in CdTe/CdS solar cells
E-MRS Spring Meeting, Strasbourg, France, 12.6.2003

* Bätzner D.L.
CdTe/CdS and CIGS Thin Film Solar Cells
Keynote at 1. International Solar-Wind-Hydro Conference, Segovia, Spain, 8.7.2003

* Batlogg B.
Recent developments in superconducting materials
The First Topical SCENET-2 Workshop and Chem-HTSC IX Workshop, Sant Feliu de Guixols, Spain, 15.11.2003

* Batlogg B.
Organic Thin Film Field-Effect Transistors
WOCSDICE 2003 The 27th Workshop on Compound Semiconductor Devices and Integrated Circuits held in Europe, Fürigen, Switzerland, 27.5.2003

* Batlogg B.
Evidence for two electronic components in Na_xCoO_2 ($x=0.7-0.75$)
Quantum Complexities in Condensed Matter, Bukhara, Uzbekistan, 23.8.2003

* Batlogg B.
Electron-lattice interaction in organic semiconductors
18. Workshop on Novel Materials and Superconductors, Plannersalm, Austria, 23.2.2003

* Bergemann and J. Takeya Ch.

Charge Transport and Search for Metallic Behaviour in Polyacenes: SCLC, Intercalation, and Single-Crystal FET
Int. Workshop Electronic properties of organic semiconductors, Lorentz Center, Leiden, Netherlands, 7.7.2003

* Bergemann Ch.

Fermi Surfaces and Electron Masses in Metallic Oxides

Kolloquium des Sonderforschungsbereichs "Komplexe Uebergangsmetallverbindungen mit Spin- und Ladungsfreiheitsgraden und Unordnung", Köln, Germany, 12.3.2003

* Bilgram J.

Komplexe Strukturen: Symbiose von Experimenten und Modellrechnungen
Zürcher Physikalische Gesellschaft, Zürich, Switzerland, 30.01.2003

Bilgram J.

Quantitative Description of Growth Morphologies of Xenon Crystals in 3D
DPG, Dresden, Germany, 25.03.2003

* Bilgram J.

Complex Structures: A Symbiosis of Experiments and Numerical Studies
EUROMAT, Lausanne, Switzerland, 02.09.2003

Brühwiler M.

Strongly enhanced low temperature resistance and heat capacity in Na_xCoO_2

2003 Swiss Workshop on Materials with Novel Electronic Properties, in Les Diablerets, Switzerland, 30.9.2003

Buess M.

Boundary conditions in precessional motion

ICM 2003, Roma, 2908.2003

Caimi G.

Ferromagnetism and Superconductivity in Boride Systems

MANEP Topical Meeting and Review Panel, Neuchatel, Switzerland, 26.06.2003

Caimi G.

Magneto-optical response of $\text{Eu}_{1-x}\text{Ca}_x\text{B}_6$

2003 Swiss Workshop on Materials with Novel Electronic Properties, Les Diablerets, Switzerland, 29.09.2003

* Degiorgi L.

Electrodynamics in correlated systems

Solid State Physics Seminar at Walther Meissner Institute, Garching, Munich, Germany, 17.02.2003

* Degiorgi L.

Luce e Materia

Lecture at Liceo Cantonale di Lugano, Lugano, Switzerland, 05.05.2003

* Degiorgi L.

Ferromagnetism and superconductivity in boride systems

Solid State Physics Seminar at Max-Planck-Institute Stuttgart, Germany, 09.05.2003

* Degiorgi L.

The synchrotron IR program at the SLS facility

Workshop on Infrared Microscopy and Spectroscopy with Accelerator-Based Sources, Lake Tahoe, U.S.A., 09.07.2003

* Degiorgi L.

Ferromagnetism and superconductivity in boride systems

Solid State Physics Seminar at University of California at San Diego, La Jolla, U.S.A., 14.07.2003

* Degiorgi L.

Dynamics of low dimensional correlated systems

International Conference on Theoretical trends in low-dimensional magnetism, Florence, Italy, 24.07.2003

* Degiorgi L.

Dynamics of low dimensional correlated systems

Euroconference on Spin and Charge Transport in Nanostructures, Braga, Portugal, 02.09.2003

Dorn A.

AFM-defined antidot lattices with top- and backgate tunability

15th international conference on Electronic Properties of Two-Dimensional Systems, Nara, Japan, 15.07.2003

Dorn A.

Charging effects of ErAs islands embedded in AlGaAs heterostructures

11th international conference on Modulated Semiconductor Structures, Nara, Japan, 17.07.2003

Dorn A.

Coulomb blockade and percolation in a quantum dot network

Swiss/US Nanoforum, Basel, 14.10.2003

* Ensslin K.

Spin and orbital effects in quantum rings

International conference on Nanoelectronics Lancaster, UK, 06.01.2003

* Ensslin K.

Spin and coherence in semiconductor nanostructures

DARPA meeting on spintronics, Lenzerheide, Switzerland, 13.02.2003

* Ensslin K.

From nuclear pore complexes to quantum rings

3rd Swiss / US-Nanoforum, Basel, Switzerland, 14.10.2003

* Ensslin K.

Nanophysics

Festvortrag for the opening of The Center for Nanoelectronic Systems for Information Technology- CNI, Forschungszentrum Jülich, Germany, 07.07.2003

* Ensslin K.

Orbital and spin states in Quantum rings

International workshop on Classical and quantum barrier transport in complex systems, Dresden, Germany, 22.05.2003

* Ensslin K.

Orbital and spin states in Quantum rings

Meeting of the Swiss Physical Society, Basel, Switzerland, 21.03.2003

* Ensslin K.

Orbital and spin states in quantum rings

Physics Colloquium, Univ. of Neuchatel, Switzerland, 12.05.2003

* Ensslin K.

Quantum physics in AFM defined quantum dots

European workshop on Local oxidation nanolithography, Madrid, Spain, 05.10.2003

* Ensslin K.

Quantum physics in quantum dots

Meeting of the Groupement De Recherche on Mesoscopic physics in Aussois, France, 24.09.2003

* Ensslin K.

Quantum physics in quantum dots

Seminar at Fraunhofer Institut, Freiburg, Germany, 28.11.2003

* Ensslin K.

Quantum physics in quantum rings

Physics Colloquium, Univ. of Geneva, Switzerland, 26.05.2003

* Ensslin K.

Spin and orbital effects in quantum rings

Physics Colloquium, Univ. of Antwerp, Belgium, 18.02.2003

* Erbudak M.

Crystal-quasicrystal interfaces

10th Conf. on Statistical Physics, Istanbul, 4.07.2003

* Erbudak M.

Structural Studies of quasi-crystal interfaces

5th General Conference of the, SMN-Vrnjacka Banja, 27.08.2003

* Erbudak M.

Investigation of symmetry properties of surfaces by means of backscattered electrons

Physics Seminar, Istanbul University, Istanbul, 10.10.2003

Flückiger T.

Structural Alignment of Al grown on the decagonal surface of Al-Co-Ni

Joint Colloquium GDR-CINQ and SPQK, Nancy, 28.05.2003

Fuhrer A.

Singlet-triplet transition in a many-electron quantum ring tuned by asymmetric gate voltages and magnetic fields

15th international conference on Electronic Properties of Two-Dimensional Systems, Nara, Japan, 17.07.2003

Fuhrer A.

Phase Coherence, Orbital and Spin States in quantum rings

Seminar, Prof. Caio Lewenkopf, Instituto de Fisica/UERJ, Brazil, 22.09.2003

Fuhrer A.

Phase Coherence, Orbital and Spin States in quantum rings

Seminar, Prof. Gilberto Medeiros Ribeiro, Laboratório Nacional de Luz Sincrotron, Brazil, 01.10.2003 A. Fuhrer

* Gavilano J.L.

NMR and dc-susceptibility studies of NaVGe_2O_6

Swiss Workshop on Materials with Novel Electronic Properties, Les Diablerets, Switzerland, 30.09.2003

* Gavilano J.L.

NMR studies of $\text{Na}_2\text{V}_3\text{O}_7$

Encuentro Científico Internacional, Lima, Peru 04.01.2003

* Gavilano J.L.

NMR studies of two unusual low dimensional spin

Physics Dep. University of Cambridge, Cambridge, England, 24.02.2003

Gavilano J.L.

Phase transitions of $\text{Na}_{0.7}\text{CoO}_2$ below 300 K

NMR and EPR of Broad-Line Solids, Specialized Colloque AMPERE, Portoroz, Slovenia 09.09.2003

Gavilano J.L.

Phase transitions of $\text{Na}_{0.7}\text{CoO}_2$ below 300 K

Swiss Workshop on Materials with Novel Electronic Properties, Les Diablerets, Switzerland, 02.09.2003

Gavilano J.L.

Physical Properties of Amorphous and Quasicrystalline $\text{Al}_{75}\text{Cu}_{15}\text{V}_{10}$ (Poster)

International conference on Magnetism, Rome, Italy, 01.08.2003

Geiser P.

GaN: bulk single crystal growth and treatment for MBE homoepitaxy

MaNEP Topical Meeting, Neuchatel, Switzerland, 25.6.2003

Goldmann C.

A method to measure transport of field-induced charge at the surface of organic molecular crystals

APS March Meeting 2003, Austin, TX, 4.3.2003

Goldmann C.

Transport of field-induced charge at the surface of pentacene single crystals

Intl. Workshop Electronic properties of organic semiconductors, Lorentz Center, Leiden, Netherlands, 8.7.2003

* Haug F.-J.

Electrical properties of the heterojunction in $\text{Cu}(\text{In,Ga})\text{Se}_2$ superstrate solar cells

3rd World Conference on Photovoltaic Energy Conversion, Osaka, Japan, 13.5.2003

Heinzel T.

Lateral correlation in self-assembled quantum dot layers probed by transport experiments

DPG Tagung, Dresden, Germany, 26.03.2003

Hinderer J.

Magnetic domains with non-spin origin: Condon domains in beryllium
Solid State Physics Journal Club, ETH Zürich, Switzerland, 28.06.2003

Hinderer J.

Condon domains
MANEP meeting in Les Diablerets, Switzerland, 30.09.2003

Hinderer J.

Unusual magnetism in quasi one-dimensional Na₂V₃O₇
MANEP meeting, Neuchâtel, Switzerland, 26.06.2003

Hochstrasser M.

Spin-resolved photoemission of surface States of W(110)-(1x1)H
PNSXM, Venice, 408.2003

Ihn T.

Ausflug in die Welt der Halbleiter Nanostrukturen: von Quantendots und Quantenringen
Physikalisches Colloquium der ETH Zürich, Zürich, Switzerland, 05.11.2003

* Ihn T.

Ausflug in die Welt der Halbleiter Nanostrukturen: von Quantendots und Quantenringen
Vortragsreihe der Physikalischen Gesellschaft Zürich, Zürich, Switzerland, 30.10.2003

* Ihn T.

Juggling Electrons and Spins in Quantum Rings
Goethe Universität, Frankfurt a. M., Germany, 08.07. 2003

* Ihn T.

Quantum Mechanics in Quantum Rings
Spring meeting of the German Physical Society, Dresden, Germany, 25.03.2003

* Ihn T.

Ring shaped quantum dots beyond constant interaction
316. W. und E. Heraeus Seminar on Correlation, Decoherence and Spin Effects in Simple and Complex Quantum Dot Systems, Bad Honnef, Germany, 24.10.2003

J. Gundlach D.

Organic Thin Film Transistors: fabrication and characterization
EUROFET meeting, Bayreuth, Germany, 3.3.2003

Kaelin M.

Low cost Cu(In,Ga)Se₂ absorber layers from selenization of precursor materials
3rd World Conference on Photovoltaic Energy Conversion, Osaka, Japan, 12.5.2003

* Karpinski J.

High pressure growth and anisotropic properties of MgB₂ single crystals
American Physical Society Meeting, Austin, TX, USA, 3.3.2003

* Karpinski J.

MgB₂ Single Crystals: High Pressure Growth and Anisotropic Properties

National Laboratory, Argonne, France, 17.3.2003

Karpinski J.

MgB₂ and Mg_{1-x}Al_xB₂ single crystals: high pressure growth and anisotropic properties

7th Int. Conference on Materials and Mechanisms of Superconductivity, Rio de Janeiro, Brasil, 26.5.2003

Karpinski J.

MgB₂ and Mg_{1-x}Al_xB₂ single crystals: high-pressure growth and physical properties

Swiss Workshop on Materials with Novel Electronic Properties, Les Diablerets, Switzerland, 29.9.2003

* Karpinski J.

High-pressure crystal growth of superconductors and nitride semiconductors

Gordon Research Conference in Solid State Chemistry, Oxford, United Kingdom, 15.9.2003

* Karpinski J.

MgB₂ single crystals: high pressure growth and anisotropic properties

European Congress on Advanced Materials and Processes EUROMAT, Lausanne, Switzerland, 4.9.2003

* Karpinski J.

Anisotropic properties and substitutions in MgB₂ single crystals, NATO Workshop on Symmetry and Heterogeneity in High Temperature

Superconductors, Erice-Sicily, Italy, 9.10.2003

Karpinski J.

MgB₂ and Mg_{1-x}Al_xB₂ single crystals: high-pressure growth and physical properties

MaNEP Topical Meeting, Neuchatel, Switzerland, 25.6.2003

Kazakov S.

Single crystal growth and properties of MgB₂ and Mg(B_{1-x}C_x)₂

7th Int. Conference on Materials and Mechanisms of Superconductivity, Rio de Janeiro, Brasil, 27.5.2003

Kazakov S.

Single crystal growth and properties of Mg(B_{1-x}C_x)₂

Swiss Workshop on Materials with Novel Electronic Properties, Les Diablerets, Switzerland, 29.9.2003

Kazakov S.

High pressure phase diagram of Mg-B-N system and crystal growth of MgB₂

MaNEP Topical Meeting, Neuchatel, Switzerland, 25.6.2003

Kellermann K.

Optisch gepumpte Bleichalkogenid Infrarotlaser auf Si-Substraten

33. IR-Kolloquium, Freiburg i. Br., Germany, 8.4.2003

Kicin S.

Scanning gate measurement in the quantum Hall regime at 300 mK

11th international conference on Modulated Semiconductor Structures, Nara, Japan, 16.07.2003

Kicin S.

Scanning gate measurements in the quantum Hall regime at 300 mK

SPG Tagung Basel, Switzerland 21.03.2003

Kurdesau F.

In-situ resistivity measurements during selenization process

E-MRS Spring Meeting, Strasbourg, France, 11.6.2003

* L. Degiorgi.

The synchrotron IR program at the SLS facility

International workshop on Advances in Experimental and Theoretical, Methods for Biological Applications of Synchrotron Radiation, Frascati, Italy, 28.02.2003

Lüscher R.

Evidence for structural compaction in Al-incorporated Al-Pd-Mn quasicrystals

Oberflächen und Grenzflächen, Meeting of the Schweizerische Arbeitsgemeinschaft, Fribourg, 24.01.2003

Lüscher R.

Growth of Al on the faceted threefold-symmetry surface of the Al-Pd-Mn quasicrystal

Aperiodic-03, Belo-Horizonte, 13.09.2003

* Landau I.

Temperature dependence of the upper critical field of type-II superconductors from isothermal magnetization data: application to high-T_c superconductors

Kapitza Institute for Physical Problems, Moscow, Russia, 05.07.2003

Landau I.L.

Temperature dependence of the upper critical field of type-II superconductors from isothermal magnetization data: application to high-T_c superconductors

International Conference on Magnetism, Rome, Italy 28.07.2003

Landau I.L.

Temperature dependencies of the upper critical field and the Ginzburg-Landau parameter for single crystalline NbSe₂ (Poster)

International Conference on Magnetism, Rome, Italy, 29.07.2003

Landau I.L.

Temperature dependencies of the upper critical field and the Ginzburg-Landau parameter for single crystalline NbSe₂
Swiss Workshop on Materials with Novel Electronic Properties, Les Diablerets, Switzerland, 29.09.2003

Leturcq R.

Multi-terminal transport through quantum dots

International workshop on Correlations, Decoherence and Spin Effects in Simple and Complex Quantum Dot Systems, Bad Honnef, Germany, October 23.10.2003

* M. Singer H.

Experiments and simulations for a quantitative description of growth morphologies of xenon crystals in 3 dimensions: 3D reconstructions and phase field simulations

Laboratory of phase transition dynamics, Institute of Low Temperature Science, Hokkaido University, Sapporo, Japan, 29.09.2003

Meier L.

Single-electron screening in a coupled dot-ring system

15th international conference on Electronic Properties of Two-Dimensional Systems, Nara, Japan, 17.07.2003

* Ott H.R.

Magnetotransport in Eu-based Hexaborides

NEDO Workshop, Key West, USA 10.03.2003

* Ott H.R.

Energy transport in Spin chains

NEDO Workshop, Key West, USA 11.03.2003

* Ott H.R.

Spins in Low Dimensional Systems

Physics Workshop, PSI Villigen, Switzerland, 30.06.2003

* Ott H.R.

Magnetotransport in Eu-based Hexaborides

ACCGE-15, Keystone, USA, 21.07.2003

* Ott H.R.

Heavy Eletron Systems

Enrico Fermi School, Varenna, Italy, 30.07.2003

* Ott H.R.

High-Tc Superconductors

Enrico Fermi School, Varenna, Italy, 31.07.2003

* Ott H.R.

Electronic transport and magnetism close to metal/insulator transitions

Enrico Fermi School, Varenna, Italy, 01.08.2003

* Ott H.R.

Spin-mediated energy transport in 1D spin systems

International Workshop, Bergisch Gladbach, Germany 05.08.2003

* Ott H.R.

Energy Transport in Low-Dimensional Spin Systems

Euroconference, Braga, Portugal, 04.09.2003

* Ott H.R.

Superconductivity, Status and Perspectives

Riso Symposium, Riso, Denmark, 11.09.2003

Perucchi A.

The Excitation Spectrum of Transition Metal Trichalcogenides XSe_3 ($X=Ta$ and Nb)

2003 Swiss Workshop on Materials with Novel Electronic Properties, Les Diablerets, Switzerland, 30.09.2003

Pernstich K.

Pentacene TFTs

EUROFET meeting, Bayreuth, Germany, 3.3.2003

Pernstich K.

Recent Advances in OTFT Fabrication

EUROFET meeting Varenna, Italy, 30.9.2003

* Pescia D.

Magnetism with Spatial and temporal resolution

Seminar at MPI für Festkörperforschung, Stuttgart, 23.04.2003

* Pescia D.

Aspect of magnetism with spatial and temporal resolution

Universita Modena, Colloquium at the Dept. of Physics degli studi di Modena, 19.06.2003

Pescia D.

Two-dimensional melting of magnetic stripes

Dimensional Magnetism, Int. Conf. on Theoretical Trends in Low, Florence, 24.07.2003

* Pescia D.

Summary speech

Dimensional Magnetism, Int. Conf. on Theoretical Trends in Low, Florence, 25.07.2003

Pioda A.

Scanning gate measurements in the quantum Hall regime at 300 mK

International Symposium: Quantum Hall effect: past, present and future Stuttgart, Germany 04.07.2003

Pioda A.,

Scanning gate measurements in the quantum Hall regime at 300 mK

SPG Tagung, Basel, Switzerland, 01.02.2003

Pioda A.

Scanning gate measurements in the quantum Hall regime at 300 mK

DPG Tagung, Dresden, Germany, 26.03.2003

Portmann O.

Microscopic mechanisms mediating topological phase transitions in the domain structure of ultrathin Fe films on Cu(110)

Frühjahrstagung des Arbeitskreises, Dresden, 24.03.2003

Portmann O.

Defects mediating a labyrinthine to stripe-domain pattern inverse transition in perpendicularly magnetized ultrathin Fe films on Cu(100)

International Conference on Magnetism 2003, Rome, 29.07.2003

Rössner B.

Nonparabolicity effects in SiGe/Ge quantum wells

Silicon Workshop Genova, Italy 13.02.2003

Rössner B.

High mobility hole gases in compressively strained Ge quantum wells

12th Euro MBE Workshop, Bad Hofgastein, Austria, 17.02.2003

Rau D.

Inhomogeneous Mn-magnetism in Al-Pd-Mn quasicrystals
ICM 2003, Rome, Italy

Rau D.

d-Electron Magnetism in Quasicrystals, SWM
Les Diablerets, Switzerland, 02.09.2003

* Rau D.

d-Electron Magnetism in Quasicrystals
High Magnetic Field Laboratory, Grenoble, France 08.10.2003

Rudmann D.

Impact of Na on structural properties and interdiffusion of CuInSe₂ and CuGaSe₂ Thin Films
3rd World Conference on Photovoltaic Energy Conversion, Osaka, Japan, 12.5.2003

Sigrist M.

Transmission phase in a ring interferometer with two quantum dots
DPG Tagung, Dresden, Germany, 26.03.03

Sigrist M.

Transmission phase through two quantum dots embedded in a four-terminal quantum ring
15th international conference on Electronic Properties of Two-Dimensional Systems, Nara, Japan, 17.07.03

Simovic B.

Toward spin resonance in a quantum dot
Workshop of EU-RTN Network on Spintronics, Munich, Germany, 21.11.2003

Singer H.M.

Quantitative Description of Growth Morphologies of Xenon Crystals in 3D
2. French German Crystal Growth Meeting, Nancy, France, 11.03.2003

Singer H.M.

Growth Morphologies of Xenon Crystals in 3D
2. French German Crystal Growth Meeting, Nancy, France, 11.03.2003

* Singer H.M.

Description quantitative des morphologies de croissance des cristaux de xénon en 3 dimensions et reconstruction tridimensionnelle des dendrites expérimentales L2MP
Université d'Aix-Marseille III, Faculté des Sciences de St Jerome, Marseille, France, 04.07.2003

Singer H.M.

Quantitative description of growth morphologies of xenon crystals in 3 dimensions and 3D reconstruction of experimental dendrites
ACCG-15, Keystone CO, USA, 24.07.2003

* Singer H.M.

Quantitative description of growth morphologies of xenon crystals in 3 dimensions and 3D reconstruction of experimental structures
Royal Institute of Technology KTH, Stockholm, Sweden 19.08.2003

Singer H.M.

Quantitative Description and Reconstruction of Growth Morphologies of Xenon Crystals in 3 Dimensions
EUROMAT, Lausanne, Switzerland, 01.09.2003

Singer H.M.

Three Dimensional Reconstruction of Experimentally Grown Xenon Dendrites
EUROMAT, Lausanne, Switzerland, 03.09.2003

* Singer H.M.

Quantitative description of growth morphologies of xenon crystals in 3 dimensions, their 3D reconstruction and comparison with 3D phase field models
Dept. of Energy, Kyoto University, Kyoto, Japan, 19.09.2003

* Sologubenko A.V.

Unusual magnetic-field-induced phase transition in the mixed state of superconducting NbSe₂
Swiss Workshop on Materials with Novel Electronic Properties, Les Diablerets, Switzerland, 01.10.2003

Takeya J.

A method to measure transport of field-induced charge at the surface of organic molecular crystals
Japanese Phys. Soc. March Meeting, Sendai, Japan, 28.3.2003

* Tiwari A.N.

Effects of Na on the Growth of Cu(In,Ga)Se₂ Thin Films and Solar Cells
MRS spring meeting, San Francisco, USA, 22.4.2003

Vaterlaus A.

Domain Configuration in perpendicularly magnetized atomically thin iron particles
ICM 2003, Roma, 10.08.2003

* Wachter P.

Evidence of a superfluid phase in a Bose condensed excitonic state
Seminar University of Geneva, Switzerland, 3. 4. 2003

Wachter P.

Intermediate valence of Plutonium chalcogenides as evidenced by photoemission
33^{emes} Journées des Actinides, Prague, Czech Republic, 27. 4. 2003

* Wachter P.

Evidence of a superfluid phase in a Bose condensed excitonic state
Workshop RWTH Aachen, Germany, 2. 5. 2003

* Wachter P.

Possibility of a superfluid phase in a Bose condensed excitonic state
SFB Kolloquium TU Dresden, Germany, 13. 10. 2003

* Wachter P.

Possibility of a superfluid phase in a Bose condensed excitonic state
Kolloquium University Leipzig, Germany, 15. 10. 2003

Weisskopf Y.

Al-growth on the decagonal surface of the Al-Co-Ni quasicrystal

Oberflächen und Grenzflächen, Meeting of the Schweizerische Arbeitsgemeinschaft, Fribourg, 24.01.2003

Weller M.

Phase Coherent Preseccional Magnetization Reversal in Microscopic Spin Valve Elements

Solid State Physics Journal Club, ETH Zürich, Switzerland, 04.07.2003

Weller M.

Unusual magnetism in quasi-one dimensional Na₂V₃O₇

MaNEP Review Panel, Neuchâtel, Switzerland, 26.06.2003

Wittwer O.

Tip splitting of xenon dendrites

DPG, Dresden, Germany, 27.03.2003

Zimin D.

Self-assembled CaF₂-on-Si(001) nanostructures

12th Euro-MBE Workshop, Bad Hofgastein, Austria, 17.2.2003

* Zogg H.

Optically pumped lead chalcogenide infrared emitters on Si-substrates

7th AITA workshop (7th Int. Workshop on Advanced Infrared Technology and Applications), Pisa, Italy, 9.9.2003

Zogg H.

Optically pumped mid-infrared lasers on Si-substrates

TDLS-2003, Tunable Diode Laser Spectroscopy conference, Zermatt, Switzerland, 18.7.2003

Zogg H.

Optically pumped lead chalcogenide infrared emitters on silicon substrates

NGS-11, 11th int. conf. on narrow gap semiconductors, Buffalo NY, USA, 18.6.2003

Zogg H.

Optically pumped lead chalcogenide infrared emitters on Si-substrates

12th Euro-MBE workshop, Bad Hofgastein, Austria, 16.2.2003